Ph. D. DISSERTATION

Directional launching methods of surface plasmon in nanoslits and applications

나노 슬릿에서의 방향성 표면 플라즈몬의 생성 방법과 응용

By

SEUNG-YEOL LEE

FEBRUARY 2014

DEPARTMENT OF ELECTRICAL AND
COMPUTER ENGINNERING
COLLEGE OF ENGINEERING
SEOUL NATIONAL UNIVERSITY

Abstract

Directional launching methods of surface plasmon in nanoslits and applications

SEUNG-YEOL LEE
DEPARTMENT OF ELECTRICAL AND
COMPUTER ENGINEERING
COLLEGE OF ENGINEERING
SEOUL NATIONAL UNIVERSITY

Surface plasmon polaritons (SPPs), known as quasi-particles generated by a collective oscillation of photons and electrons, have been studied by numerous researchers due to their various fascinating properties such as sub-wavelength confinement characteristics and strong electromagnetic field enhancement near metal surface. Indeed, such characteristics are quite demanded to design a novel photonic devices for future technologies such as highly integrated photonic circuit and optical storage system with ultra-high density. Hence, numerous studies have been reported about optical devices based on the physical characteristics of SPPs, so-called "plasmonic devices." Although they are not yet combined to integrated system which can overcome the conventional computing system operated by electrons, optical or quantum computing via SPPs is still an impressive issue in nanophotonics.

One of the necessary parts of optical computing is a switching of SPP source. The works done in this dissertation are focused on the physical mechanism and structural design of nanostructures such as nanoslit and nanoaperture which can be used to switch SPP source. After brief introduction, the first part of this dissertation discusses on the various methods for directional switching of SPP excitation from nanoslit geometry. In broad separation, two types of directional switching mechanisms are demonstrated: the first one is a plasmonic directional switching which can be modulated by polarization modulation. It is shown that the excited SPPs from nanoslit can be unidirectionally launched without any asymmetry of neither geometry nor incident momentum at certain polarization state when the light illuminates obliquely along the parallel-to-slit direction.

To explain such a novel type of SPP excitation phenomenon, an induced current model that can explain an aspect of SPP excitation from nanoslit for TE and TM polarization illumination is proposed. Then, appropriate experimental results are followed to verify the possibility and performance of unidirectional SPP excitation.

Then, the second type of plasmonic directional switching method, which can be modulated by phase modulation, is discussed. When two beams illuminate obliquely to nanoslit, it is found that excited SPPs from nanoslit have either symmetric or anti-symmetric profile according to the relative location between node of interference pattern and center of slit. After finding the optimized condition of nanoslit geometry which can efficiently excite both symmetric and anti-symmetric SPPs in nearly same amplitude scale, experimental demonstration of SPP switching is achieved with electromotive phase modulation done by piezo-stage. The origins of both types of switching methods can be explained by the induced charge distribution near the nanoslit.

In the second part of this dissertation, various plasmonic devices that use the switching mechanism introduced in the first part of this dissertation are demonstrated. For the realization of optical signal multiplexing and spectrum analyzing in integrated chip scale, it is necessary to develop a plasmonic color splitter which can clearly split the designed region of frequencies. By applying the physical analogy discussed in the first part of this dissertation, theoretical analysis on the plasmonic dichroic splitter that can launch two different frequencies of visible light into an opposite direction is shown for the first application device. In this case, metal-insulator-metal (MIM) waveguide structure is used instead of single interface geometry to form a Fabry-Perot resonator structure at the entrance of SPP coupler. Similar to the work done in the first part, this plasmonic dichoric splitter can also switch their launching directions of SPPs when incident polarization state is changed.

Moreover, beaming from surface plasmon source has great potential to generate a subwavelength scale of optical beam. For the second application device, analysis on the plasmonic beaming from plasmonic double spiral bull's eye geometry is discussed. Chiral geometry pattern of spiral bull's eye geometry can lead to the polarization dependent characteristics for beam generation. It is shown that the generated beam from spiral bull's eye can be switched on and off according to the optical polarization of incident light. Such beam switching phenomenon can be explained by the angular momentum change, which is caused by spin-orbital interaction at the nanohole and spiral gratings.

Keywords: Plasmonics, nanophotonics, surface plasmons, diffraction limit, surface plasmon switching, surface plasmon interference, plasmonic modulator, plasmonic dichroic splitter, plasmonic beam generation, Bull's eye structure, angular momentum.

Student number: 2009-20862

Contents

List of Figures

List of Tables

Chapter 1

Introduction

1.1. Overview on plasmonics

In recent progress on nanophotonics, the interaction of photons with various types of materials has been significantly researched and now it gives a breakthrough to overcome the several limitations on conventional optics [1, 2]. Among them, plasmonics is a field of researching area that explores the role of surface plasmon polaritons (SPPs) and their applications. SPPs are quasi-particles generated at the surface of conductive materials by a collective oscillation of photons and electrons [3]. In the viewpoint of electromagnetic wave, SPPs are kind of surface wave that propagates or oscillates near the surface of conductive materials. Hence, it is possible to control the highly confined light on metallic surface, or to generate intensive hot spot beyond the diffraction limits [4].

Although the early scientists predicts the existence of SPPs as a solution of Maxwell's equation, the discovery of SPPs are fascinated by detecting an anomalous enhancement of optical transmission in metallic hole array. This "extraordinary optical transmission (EOT)" phenomenon gives a strong impact on nanophotonics field since it shows that SPPs have quite significant role in the metallic nanostructure [5]. After discovery of EOT, many scientists and engineers have dedicated themselves to the study of these beneficial characteristics of SPPs and endeavor to find a breakthrough to reach innovative future technologies such as optical devices on integrated chip

[6], invisibility cloak [7], next-generation optical data storage [8], photovoltaic devices [9], and quantum computing [10]. Since the speed of light is far faster than flow of electrical current used in conventional computing system, replacing the signal source of computing system from electron to photon has great advantages. Although long-ranged data processing between personal computers uses optical signals based on fiber optical communications, it is quite difficult to directly use optical fiber into the integrated optical circuit due to the large size and significant bending loss of optical fiber [11]. Waveguides based on surface plasmon source that is often referred to as “plasmonic waveguides”, however, have extremely confined guiding characteristics of SPP signals far below half of the wavelength scale, which is known as a diffraction limit of light [12]. Hence, it is possible to use SPPs as a source of integrated photonic circuit. Moreover, strong light-material interaction caused by SPPs in metallic nanostructures gives various anomalous phenomena like a negative refractive index properties [13], strong optical activity [14], and giant optical field enhancement [15]. All of these features make surface plasmons quite useful for the applications such as superlens [16], metamaterials [17–19], and next-generation solar cell [20].

As similar to other fascinated technology, plasmonics still have some issues to be overcome. For example, significant thermal loss of SPPs gives difficulty to practically utilize SPPs as a source of integrated optical system. To solve this problem, scientists struggle to improve thermal loss problems by adapting novel type of metamaterial [21] or graphene-based plasmonics [22]. Other problems such as sensitivity to metal roughness and fabrication issues in nanoscale should also be solved as soon as possible. Nevertheless, plasmonics is one of the promising research fields to overcome the limitations of conventional optics and it seems that various applications researched in plasmonics can flourish our life in future world.

1.2. Motivation of this dissertation

During a few decades of progresses in plasmonics, there have been lots of attempt to use SPPs as a source of integrated optical circuit. To build a platform of integrated plasmonic system on the metal substrate, various types of devices such as waveguide [23], beam splitter [24], plasmonic lens [25], input and output coupler [26], interconnector [27], etc. have been proposed and successfully demonstrated. Plasmonic switching device is also one of them. It includes plasmonic devices which can change launching direction of light, switch on and off the state of

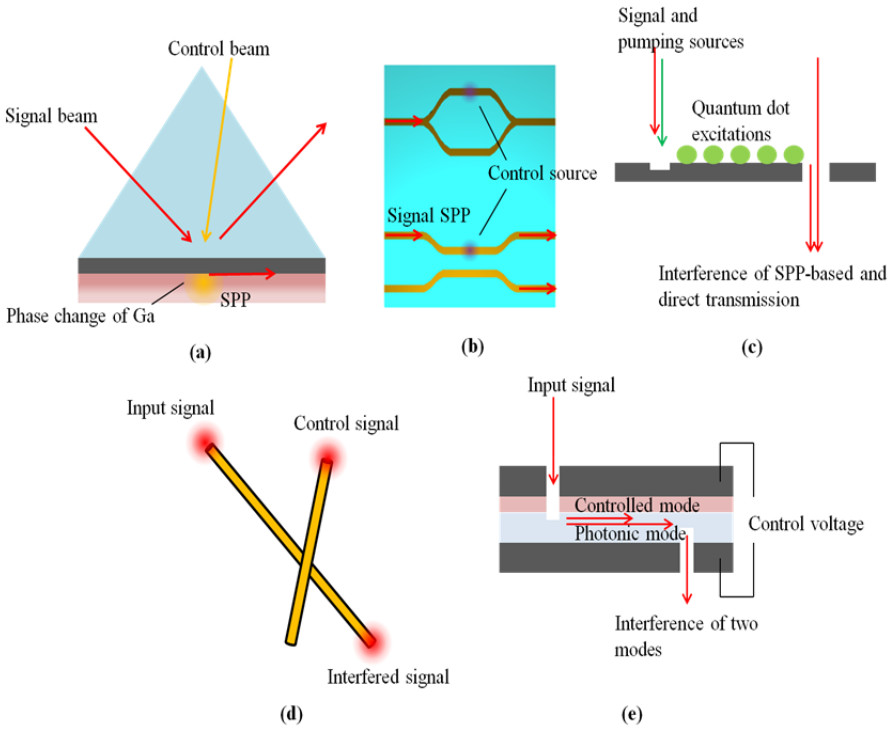

Figure 1.1. Schematics of representative previous works for switching the SPPs excitation based on: (a) a phase transition of gallium, (b) interference in plasmonic directional coupler and Mach-Zehnder interferometer, (c) quantum dot excitation, (d) interference at the junction of nanorods, and (e) cutoff of specific plasmonic mode by electric modulations.

beam generation and control the state change between hot spot and dark spot by simple interaction

on incident light or generated SPPs [28]. Here, it will be better to clearly note that plasmonic switching devices contain not only the structure operated with active material or nonlinear phenomenon, but also all kinds of nanostructures which can dramatically change the optical response by small change of external conditions including the incident light source. Indeed, it is not possible to say such structures as active plasmonic devices; however, these structures have great potential for realizing active integrated plasmonic system since they can modulate the flow of the optical signals with a simple interaction such as phase change of light.

In Fig. 1.1, schematics of representative previous works for switching the SPP excitation or far-field generation from SPPs are presented. One of the pioneering works in this field is using the thermal phase change of material that controls the propagation of SPPs in Kretschmann configuration, as shown in Fig. 1.1(a) [29]. Moreover, there are numerous types of inteferometric control of SPPs signal using the directional couplers or Mach-Zehnder interferometers, as shown in Fig. 1.1(b) [30, 31]. The control of interference of SPPs can be achieved by using electric signals or quantum dot excitations from the control sources [32] (Fig. 1.1(c)). Researchers also tried to find other plasmonic structures in order to control SPPs in even smaller scale, such as nanowire [33]. A network of nanowire structure is one of the representative geometries for SPP-based interferometric logics which are realized on a subwavelength-scale, which is shown in Fig. 1.1(d). Chemically synthesized nanowires deposited on dielectric substrate can couple the propagating SPPs with low phase incoherency, and it has been shown that interference of propagating SPPs at the intersection or junction points of nanowire networks can control the intensity of out-coupled field with the on-off ratio of 10 [33]. Control of SPPs can also be achieved by using the mode cutoff characteristics of specific SPP mode, which demonstrates electro-optically driven plasmonic switch in metal-dielectric-metal plasmonic waveguide [34] ((Fig. 1.1(e)). Like these, numerous types of SPP switching methods exist.

Although there exist various methods for launching and guiding the SPPs on the metal substrate, SPP excitation from nanoslit is one of the fundamental and powerful methods to launch SPPs. A nanoslit can excite SPPs when light illuminates it by matching the spatial linear momentum of incident light through the diffraction from nanoslit. This method is advantageous compared to other methods such as Kretschmann's configuration. First, the excitation location of SPPs can be confined to the slit, so that the SPP sources can be completely separated from the incident and reflected light. Second, it can provide uniform intensity and phase profile along the slit when the fabrication of slit is carefully done. At last, numerous previous researches have modeled the coupling characteristics of SPPs from nanoslit; so it is quite easy to design a slit parameter and

easy to fabricate [35, 36]. Due to these benefits, nanoslit structure has been used for efficient SPP coupler in numerous studies, and revealing physical mechanisms and modeling of SPPs excitation near the nanoslit is still ongoing research process.

Therefore, the motivation of this dissertation is to propose novel plasmonic switching methods which are applicable to the excitation of SPPs or far-field beam generation from the simplest plasmonic structures such as nanoslit or nanoaperture. As will be discussed throughout this dissertation, the key control factors can be polarization state, phase difference, or incident wavelength according to the slight difference in their configuration. For the starting point of the realization of integrated plasmonic system, nanoslit structure can be a successful SPP coupler or source from the external control beams, hence switchable excitation of SPPs from nanoslit and nanoaperture has a great potential for being utilized in fundamental device in integrated photonic system.

1.3. Scope and Organization

In this dissertation, novel types of switchable unidirectional SPP launching methods from a nanoslit, which can be switched by incident polarization modulation and incident phase, are proposed in chapter 2. Before the physical mechanisms of SPPs excitation from nanoslit are discussed, brief review on basic principles and modal profiles of SPPs in various types of plasmonic waveguides are introduced in section 2.1. The knowledge introduced in section 2.1 will be helpful to understand the concept of plasmonic mode and their characteristics which are generally used throughout this dissertation. Characteristics of SPP mode in single interface metal surface and MIM waveguide are explained in subsections 2.1.1 and 2.1.2, respectively. Then, the demonstration of unidirectional SPP excitation from nanoslit which can be modulated by incident polarization state will be discussed on section 2.2. Configuration of proposed SPP excitation methods, charge induced model, line dipole modeling of radiated field from nanoslit in various polarization incidences are covered in subsection 2.2.1. Numerical simulation results and experimental demonstrations of the proposed scheme are explained in detail in subsections 2.2.2 and 2.2.3, respectively.

Compared to the work done in section 2.2, the work discussed on section 2.3 is a switchable unidirectional launching of SPPs operated by phase modulation of incident light. Indeed, changing the phase of light is much simpler than polarization modulation, and this method also improved some problems such as oblique launching from nanoslit, which are observed in the work done in

section 2.2. In section 2.3.1, configuration of proposed method and physical mechanisms are introduced. Then, the optimization process to find the slit condition which can efficiently launch and switch SPPs will be followed in section 2.3.2. Experimental configurations, comparison between simulations and experiments are discussed in section 2.3.3.

In chapter 3, specific applications that can be achieved by using the SPP modulation phenomenon demonstrated in chapter 2 are discussed. At first, in section 3.1, the concept of polarization-modulated unidirectional launching demonstrated in section 2.2 is applied to realize a plasmonic dichroic splitter by combining this concept with the efficient Fabry-Perot cavity structure. Here, the demonstration of plasmonic dichroic splitter is done by using the nanoslit coupler carved on the MIM plasmonic waveguide. Geometrical configuration and physical mechanism of the proposed plasmonic dichroic splitter is explained in subsection 3.1.1. Next, optimization process of Fabry-Perot cavity structure to improve both the dichroic and unidirectional characteristics of the proposed structure is followed in subsection 3.1.2. Experimental configuration and results of demonstrated plasmonic dichroic splitter are shown in subsection 3.1.3.

In section 3.2, analysis on switchable beam controlling method will be discussed. Unlike the previous section, the focus of this section is not a directional change of excited SPPs, but the absolute intensity modulation of optical beaming from double spiral bull's eye geometry. In subsection 3.2.1, principle of conventional bull's eye structure and basic concept of spin orbital interaction in plasmonic structure are introduced. Then, the proposed double spiral geometry and its working mechanism are explained with the help of the change of vortex topological charge. At last, full electromagnetic simulation results for double spiral bull's eye geometry are demonstrated in section 3.2.2 to check the performance of on and off switching ratio. Finally, concluding remarks for this dissertation are provided in chapter 4.

Chapter 2

Methods for surface plasmon directional launching from nanoslit

Propagating surface plasmons (PSPs) are kind of surface plasmons that propagate through the smooth surface of metal-dielectric interfaces or more complicated layered structures such as metal-dielectric-metal waveguides. Since PSPs has great potential for using SPP source as a integrated photonic devices, unidirectional launching of PSPs have been intensively researched for the purpose of compactness, increase of excitation efficiency, and reduction of noise signals. Various types of structures have been proposed for unidirectional SPP launchers such as an asymmetric nanoslit [37], double slits [38], or a nanoslit with asymmetric gratings [39].

However, these works are not appropriate for the application of plasmonic switching devices since the overall sample should be rotated or the incident angle should be reversed to switch the launching direction. Such methods are difficult to apply in practice, so other mechanisms that can used to switch the SPP launching direction more easily are needed.

In this chapter, novel types of unidirectional SPP launching methods are proposed in order to solve abovementioned problems. Before explaining the modulation methods, basic principles on surface plasmon modes in plasmonic waveguide will be introduced in section 2.1. In section 2.2, modulation of the launching direction of SPPs is done by changing the polarization state of incident light. The principles of the methods are based on the movement of induced charge generated near the nanoslit. To explain the physical mechanism of this phenomenon, two different

types of SPP excitation model is applied for two orthogonal polarization states: perpendicular-to-slit electric field (TE) and magnetic field (TM) components. Then, experimental results are demonstrated to verify the proposed SPPs switching mechanism. In section 2.3, another type of modulation method is introduced which is done by changing the relative phase difference between two incident lights.

2.1. Basic principles of SPPs in plasmonic waveguides

Throughout this dissertation, most of the works done is based on the field interference and coupling characteristics from nanoslit to plasmonic waveguide. Hence, it is significantly helpful to understand the basic principles and mode characteristics on plasmonic waveguides including single interface and metal-dielectric-metal waveguide. Before the main topic of this chapter is discussed, basic principles, mode characteristics, and mode dispersion diagram of various types of SPP modes are briefly summarized in this section.

2.1.1. Characteristics of SPP mode in single interface

In a viewpoint of light as a particle, SPPs can be explained as a quasi-particle generated by the resonant coupling of photons and electrons existed in the surface of metal [3]. However, it is possible to consider an SPP as a kind of electromagnetic surface wave which can satisfy the Maxwell's equations. To understand the field distribution and mode characteristics of SPP mode on planar metallic waveguides, it is convenient to approach SPPs as a mathematical solution of Maxwell's equations at the metal surface. For the simplest case, it will be started with the single interface of metal and dielectric structure as shown in Fig. 2.1.1.

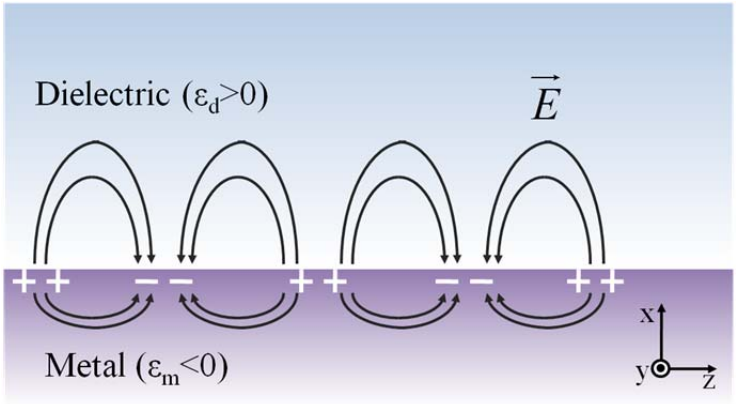

Figure 2.1.1. SPPs at the interface between a metal and a dielectric layer.

As depicted in Fig. 2.1.1, the important factor for the existence of bounded surface mode at the interface between two layers is opposite sign of permittivity between two layers. In general, dielectric media such as air, water, glass, and quartz have positive value of permittivity for most ranges of optical and THz frequencies. On the other hand, metallic substrates such as gold, silver, copper, and aluminum have negative real part of permittivity. The permittivity of metal (ε_m) is often modeled by the Drude model:

$$\varepsilon_m = \varepsilon_\infty - \frac{\omega_p^{\,2}}{\omega(\omega + j\gamma)}, \tag{2.1.1}$$

where ω_p is the plasma frequency of metal and γ is collision frequency. ε_∞ is the dielectric constant at infinite frequency. Therefore, electromagnetic waves which have lower frequency than the ω_p of metal cannot propagate inside the metal but evanescently decays along the penetration. At the interface between two materials which have opposite sign of permittivity, magnetic field of transverse magnetic (TM) surface mode can be achieved as follows:

$$H_y(x,z) = \begin{cases} A\exp(j\beta z)\exp(-\kappa_d x) & (x \geq 0) \\ A\exp(j\beta z)\exp(\kappa_m x) & (x \leq 0) \end{cases}. \tag{2.1.2}$$

From the H_y field, electric field components can also be obtained from the Maxwell's curl equation,

$$\nabla \times \mathbf{H} = -j\omega\varepsilon_0\varepsilon_r\mathbf{E}, \tag{2.1.3}$$

which can be resulted in

$$E_x(x,z)=\begin{cases}\dfrac{\beta}{\omega\varepsilon_0\varepsilon_d}A\exp(j\beta z)\exp(-\kappa_d x) & (x\geq 0)\\ \dfrac{\beta}{\omega\varepsilon_0\varepsilon_m}A\exp(j\beta z)\exp(\kappa_m x) & (x\leq 0)\end{cases} \tag{2.1.4}$$

$$E_z(x,z)=\begin{cases}\dfrac{\kappa_d}{j\omega\varepsilon_0\varepsilon_d}A\exp(j\beta z)\exp(-\kappa_d x) & (x\geq 0)\\ \dfrac{\kappa_m}{-j\omega\varepsilon_0\varepsilon_m}A\exp(j\beta z)\exp(\kappa_m x) & (x\leq 0)\end{cases}. \tag{2.1.5}$$

Due to the momentum conservation condition, it is possible to obtain

$$\begin{aligned}-\kappa_d{}^2+\beta^2&=\varepsilon_d k_0{}^2\\ -\kappa_m{}^2+\beta^2&=\varepsilon_m k_0{}^2\end{aligned}, \tag{2.1.6}$$

where k_0 is wavenumber at freespace, which can be expressed as ω/c_0, where c_0 is the speed of light in vacuum. By using the boundary condition at the interface (x = 0), tangential electric (E_z) and magnetic (H_y) field should be continuous at x = 0, which gives us following relation from (2.1.2) and (2.1.5):

$$\frac{\kappa_d}{\varepsilon_d}+\frac{\kappa_m}{\varepsilon_m}=0. \tag{2.1.7}$$

From the three equations depicted in (2.1.6) and (2.1.7), an effective propagation number of single interface SPP mode (β) can be obtained as follows,

$$\beta=k_0\sqrt{\frac{\varepsilon_d\varepsilon_m}{\varepsilon_d+\varepsilon_m}}. \tag{2.1.8}$$

In Fig. 2.1.2, the dispersion curve of SPP mode at single interface is shown. One important feature of the dispersion characteristics is that it lies on the right side of the light line at the homogeneous dielectric medium. This means β is always higher than $\sqrt{\varepsilon_d}k_0$, hence field decays exponentially into the dielectric medium.

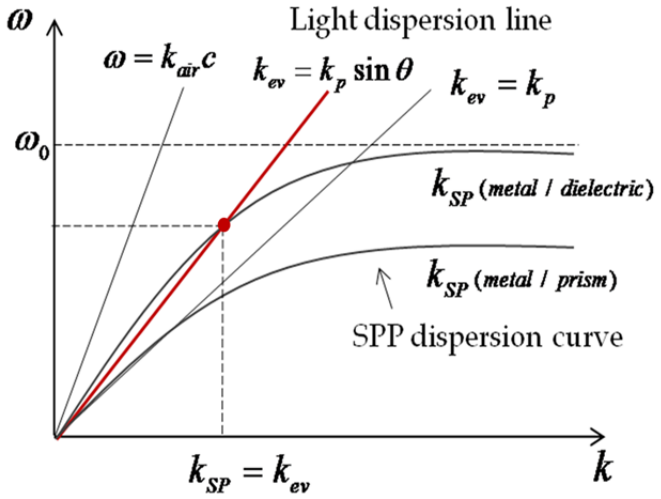

Figure 2.1.2. Dispersion curves of SPP at a dielectric–metal interface, propagating light in the dielectric medium, and momentum matching condition done by Kretschmann's configuration are shown.

Such momentum mismatch between propagating light waves in dielectric and SPP mode indicates that it is impossible to excite SPPs at the metal-dielectric surface by simply illuminating light through the flat metal surface. Instead, SPPs can be excited to flat metal surface by using the prism coupling methods, which are known as a Kretschmann's configuration and Otto's configuration [40, 41], and shown in Fig. 2.1.3.

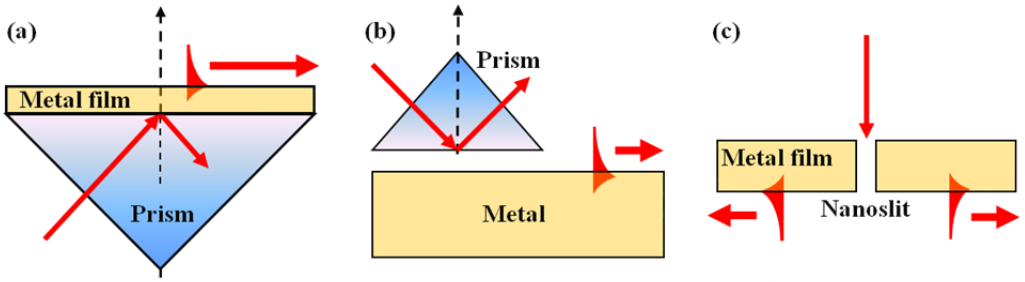

Figure 2.1.3. Representative methods for exciting SPPs: (a) Kretschmann's configuration, (b) Otto's configuration, and (c) nanoslit coupling.

These methods can match the momentum mismatch between light line and the SPP mode by

using the prism which has higher refractive index than the dielectric material used for SPP generation ($\varepsilon_{prism} > \varepsilon_d$). Then, the light line in prism can intersect with the SPP mode as shown in Fig. 2.1.2, so the momentum matching is satisfied and SPPs can be excited.

On the other hand, SPPs can also be excited by micro- or nano-sized geometry such as slits, gratings, bumps, and particles. In this case, some portion of diffracted light from these structures can match to the momentum condition so that propagating SPPs mode can be generated. Especially, nanoslit structure is frequently used in this dissertation in order to excite and manipulate the SPP mode. It is possible to consider the nanoslit as a MIM plasmonic waveguide when the length of slit is sufficiently long. Moreover, the MIM plasmonic waveguide is used instead of single interface plasmonic waveguide to realize a plasmonic dichroic color splitter in chapter 3. Due to these reasons, brief explanation on the characteristics of SPP modes in MIM plasmonic waveguide will be explained in the next subsection.

2.1.2. Characteristics of SPP mode in MIM plasmonic waveguides

An MIM plasmonic waveguide is three-layered plasmonic waveguide structure which consists of insulator (dielectric material such as glass, silicon, silicon nitride are often used) core encapsulated by metallic cladding structure as shown in Fig. 2.1.4. Compared to mode of single interface structure as mentioned in previous subsection, modes of MIM plasmonic waveguide have much higher compactness even though its propagation length is in similar to the mode of single interface plasmonic waveguide. Moreover, due to its complicate aspect appeared in their dispersion relation, anomalous effects such as negative refractive index and zero group velocity phenomena [42] are observed. These anomalous characteristics have been applied to generate negative Airy beam generation [43], rainbow trapping in tapered MIM waveguide [44], optical trapping and filtering [45].

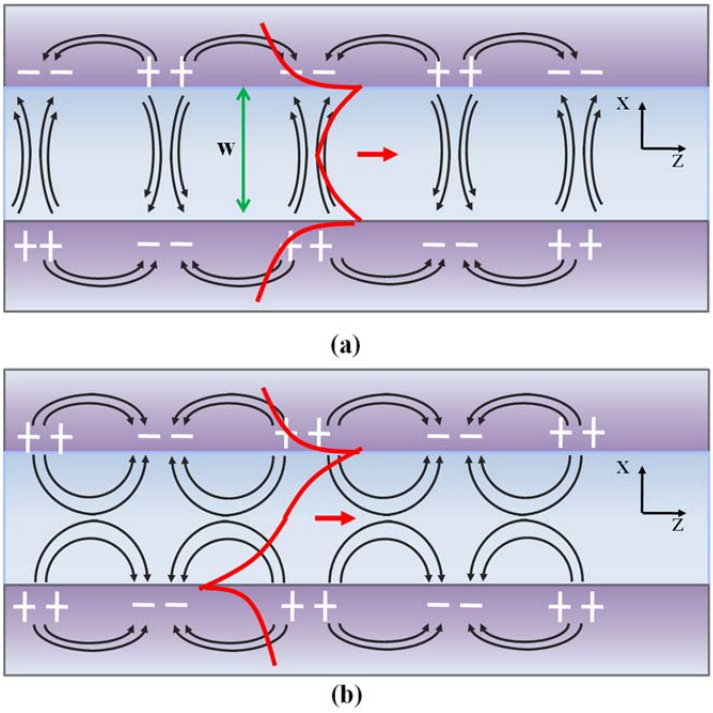

Figure 2.1.4. SPPs at the MIM plasmonic waveguide. Schematics for (a) symmetric and (b) anti-symmetric plasmonic modes are shown.

Similar to single interface case, it is convenient to approach plasmonic modes on a MIM plasmonic waveguide as a mathematical solution of Maxwell's equations. In this case, magnetic field of transverse magnetic (TM) surface mode can be achieved as follows:

$$H_y(x,z)=\begin{cases} A\exp(j\beta z)\exp\left(-\kappa_m\left(x-\frac{w}{2}\right)\right) & z\geq\frac{w}{2} \\ \exp(j\beta z)\left(\mathrm{B}\exp\left(\kappa_d\left(x-\frac{w}{2}\right)\right)+C\exp\left(-\kappa_d\left(x+\frac{w}{2}\right)\right)\right) & -\frac{w}{2}\leq z\leq\frac{w}{2} \\ D\exp(j\beta z)\exp\left(\kappa_m\left(x+\frac{w}{2}\right)\right) & z\leq-\frac{w}{2} \end{cases} \tag{2.1.9}$$

From the H_y field, electric field components can be obtained from (2.1.3), which can be resulted in,

$$E_x(x,z)=\begin{cases} A\dfrac{\beta}{\omega\varepsilon_0\varepsilon_m}\exp(j\beta z)\exp\left(-\kappa_m\left(x-\dfrac{w}{2}\right)\right) & z\geq\dfrac{w}{2} \\ \dfrac{\beta}{\omega\varepsilon_0\varepsilon_d}\exp(j\beta z)\left(B\exp\left(\kappa_d\left(x-\dfrac{w}{2}\right)\right)+C\exp\left(-\kappa_d\left(x+\dfrac{w}{2}\right)\right)\right) & -\dfrac{w}{2}\leq z\leq\dfrac{w}{2} \\ D\dfrac{\beta}{\omega\varepsilon_0\varepsilon_m}\exp(j\beta z)\exp\left(\kappa_m\left(x+\dfrac{w}{2}\right)\right) & z\leq-\dfrac{w}{2} \end{cases} \tag{2.1.10}$$

$$E_z(x,z)=\begin{cases} A\dfrac{\kappa_m}{j\omega\varepsilon_0\varepsilon_m}\exp(j\beta z)\exp\left(-\kappa_m\left(x-\dfrac{w}{2}\right)\right) & z\geq\dfrac{w}{2} \\ \dfrac{-\kappa_d}{j\omega\varepsilon_0\varepsilon_d}\exp(j\beta z)\left(B\exp\left(\kappa_d\left(x-\dfrac{w}{2}\right)\right)-C\exp\left(-\kappa_d\left(x+\dfrac{w}{2}\right)\right)\right) & -\dfrac{w}{2}\leq z\leq\dfrac{w}{2} \\ D\dfrac{-\kappa_m}{j\omega\varepsilon_0\varepsilon_m}\exp(j\beta z)\exp\left(\kappa_m\left(x+\dfrac{w}{2}\right)\right) & z\leq-\dfrac{w}{2} \end{cases}. \tag{2.1.11}$$

By using the boundary conditions at the interfaces ($x=\pm w/2$), tangential electric (E_z) and magnetic (H_y) fields should be continuous. Due to the symmetry of MIM waveguide, $B=\pm C$. If $B=C$, it will give a solution for symmetric plasmonic mode, whereas that for the anti-symmetric plasmonic mode is obtained when $B=-C$. Solving the boundary conditions will give a characteristic equation of MIM plasmonic modes, which can be expressed as

$$\frac{\kappa_d}{\varepsilon_d}+\frac{\kappa_m}{\varepsilon_m}\tanh\left(\frac{\kappa_m w}{2}\right)=0\,, \tag{2.1.12}$$

$$\frac{\kappa_d}{\varepsilon_d}+\frac{\kappa_m}{\varepsilon_m}\coth\left(\frac{\kappa_m w}{2}\right)=0\,, \tag{2.1.13}$$

where Eqs. (2.1.12) and (2.1.13) show the case of symmetric and anti-symmetric MIM plasmonic mode, respectively. By combining these equations with the momentum matching condition shown in Eq. (2.1.6), it is possible to find the solution for effective propagation number similar to the case of single interface SPPs, and it is also possible to find the dispersion relations of MIM plasmonic waveguide. Since this calculation cannot be solved in single analytic form, numerically calculated dispersion curves for both modes to show the aspect of these modes are shown in Fig. 2.1.5. The symmetric MIM mode has similar dispersion aspect with respect to the case of single interface SPPs, which do not have any cutoff frequency, and this mode always laid on the right-side of light line. In the research field of plasmonics, this mode has received significant attention for chip-scale optical communications based on plasmonic waveguides because it does not have any cutoff frequency, so it would be possible to overcome the diffraction limit [46]. On the other hand, the dispersion curve of the anti-symmetric plasmonic mode starts from the left side of the

light line; it does not have evanescently decaying modal profile near the cutoff frequency. However, it is gradually changed from photonic to plasmonic modal profile and finally follows the dispersion curve of symmetric plasmonic mode. Although this mode may not be appropriate for transferring more energy into a subwavelength slit, it is appropriate to generate anomalous effects in plasmonic waveguides such as negative refractive index or zero group velocity. Especially, in the section 2.3 of this dissertation, control of relative coupling efficiency between these two plasmonic modes becomes a key factor for switching the launching direction of SPPs at the transmission side of nanoslit.

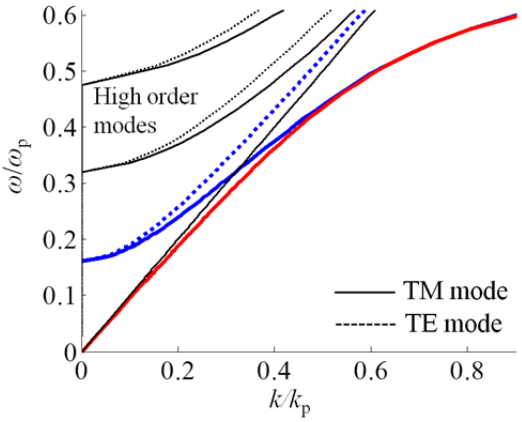

Figure 2.1.5. Plasmonic and photonic modes in the MIM waveguide geometry. Red solid line indicates the dispersion curve of symmetric MIM plasmonic mode, whereas blue solid line indicates that of anti-symmetric plasmonic mode, all other curves laid on the left side of light line denote the dispersion relation of photonic modes.

2.2. Demonstration of polarization-modulated SPP excitation from nanoslit

2.2.1. Principle of polarization-modulated directional launching

During the few decades, nanoslit structure has been considered to excite SPPs at the transmission side of metallic substrate with highly predictable amplitude and low noise signals. For the slit excitation problems, researchers have been only focused on the mechanism of SPP excitation with the incident electromagnetic waves having perpendicular electric fields to the slit, since it is

natural to think SPPs are only generated when the collective oscillation of free electrons exists. Modeling of SPP excitation problem from nanoslit with electric fields normal to the slit is often expressed by an electric line dipole source [47, 48], which accumulates opposite sign of charge across the nanoslit.

On the other hand, SPPs are not generated from the slit when incident waves are polarized to parallel-to-slit direction with normal illumination. However, under certain conditions, SPPs can be excited via an incident light that has no electric component normal to the slit, which only has parallel-to-slit electric component. In this situation, the electric dipole cannot be formed across the slit but magnetic induction currents are the origin of the SPP excitation [49].

In this section, the mechanisms of SPP excitation from nanoslit by using the induced surface current on metal surface are discussed, which are calculated from the incident electromagnetic fields for TE and TM incidence, respectively. After that, charge oscillation aspects at the edge of nanoslit are calculated from the surface current. In addition to conventional electric line dipole modeling for TE incidence case, modeling of SPP excitation aspect for TM incidence case is produced by magnetic line dipole source, which is done by calculating the Green's dyadic function.

2.2.1.1. Induced surface current and charge characteristics

In microwave region, conductivity of noble metal is high enough to respond directly to the external electromagnetic wave. Therefore, it is often assumed to be a perfect electric conductor (PEC). When the electromagnetic wave illuminated the PEC, unbounded free electrons existing in PEC surface directly respond to the electromagnetic wave not to allow the propagation of incident wave into the PEC, and the flow of surface currents results to the reflection wave. Therefore, in ideal PEC, electromagnetic waves cannot exist inside them; so surface currents only exist within the infinitesimal skin depth. The amount of surface current, which is derived from the Maxwell's curl equation at the boundary sheet of PEC, is written as,

$$\hat{\mathrm{n}} \times \mathbf{H} = \mathbf{K} . \tag{2.2.1}$$

where $\hat{\mathrm{n}}$, $\mathbf{H}$, and $\mathbf{K}$ are the surface normal unit vector, magnetic field vector at surface, and surface current density, respectively.

However, when the frequency of electromagnetic wave is increased to infrared or visible range, it is not possible to assume the noble metal as a PEC since free electrons do not anymore respond immediately at this frequency region. Fields penetrate into the metal; so surface currents flow

through the finite depth of surface. A penetration depth of material is defined as the depth where field amplitude of the radiation inside the material falls to 1/*e* of its original value, which can be expressed with the permittivity of material as follows,

$$\delta = \frac{1}{\mathrm{Im}(\sqrt{\varepsilon_r})k_0}. \tag{2.2.2}$$

According to the material parameters noted in ref. [50], penetration depth of silver and gold at the frequency of 532 nm is obtained to 25 nm and 32 nm, respectively. Considering the metal film is much thicker than penetration depth, electromagnetic fields are nearly zero at the beneath of metal surface even for these frequency region. Hence, similar to the case of PEC, it is possible to assume the amount of surface currents calculated from (2.2.1) effectively flows within the region of penetration depth. For example, surface current density at half-infinite metal plate laid on $z = 0$ plane can be expressed with the current density $\mathbf{J}$,

$$\mathbf{K} = \int_{-\infty}^{0} \mathbf{J}\, \mathrm{e}^{\frac{z}{\delta}}\, dz = \delta \mathbf{J}. \tag{2.2.3}$$

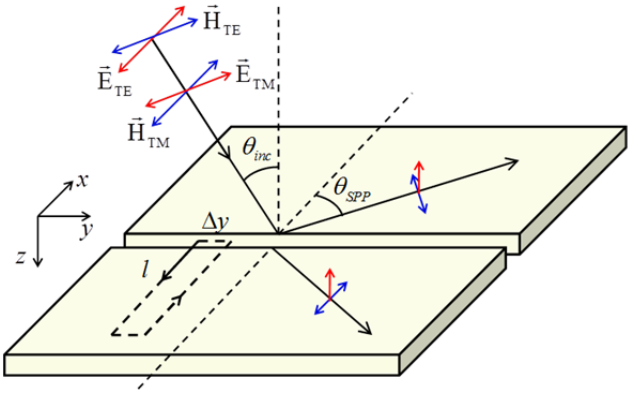

Figure 2.2.1. Configuration of the circumstance of oblique incidence that will be used for polarization dependent unidirectional launching of SPPs.

From now, let us consider the circumstance of electromagnetic waves illuminating the nanoslit structure as depicted in Fig. 2.2.1. The incident light obliquely illuminates the nanoslit in *y*-*z* plane with the incident angle of θ_{inc}. Field orientation of two orthogonal polarization states: TE and TM waves are defined as shown in Fig. 2.2.1. Although there is a field perturbation caused by the

nanoslit, it is not considered to calculation of surface current since it is a secondary wave generated together with SPPs. The magnetic field component of incident and reflected field for both polarization states without considering the slit can be expressed as,

$$\begin{aligned}\mathbf{H}_{TE}(x,y,z) &= H_0(\cos\theta_{inc}(e^{jk_z z} - r_s e^{-jk_z z})\hat{y} + \sin\theta_{inc}(e^{jk_z z} + r_s e^{-jk_z z})\hat{z})e^{jk_y y} \\ \mathbf{H}_{TM}(x,y,z) &= (e^{jk_z z} - r_p e^{-jk_z z})H_0\hat{x}e^{jk_y y}\end{aligned}, \quad (2.2.4)$$

where $k_y = k_0 \sin\theta_{inc}$, $k_z = k_0 \cos\theta_{inc}$, r_s and r_p denote the Fresnel reflection coefficient for *s* and *p* polarization cases between air and metal interface, respectively. By using the Eqs. (2.2.1) and (2.2.4), it is possible to obtain a surface current density at the illuminated metal surface as follows,

$$\mathbf{K} = -\hat{z} \times \mathbf{H}\Big|_{z=0} = \begin{cases} H_0 \cos\theta_{inc}(1-r_s)e^{jk_y y}\hat{x} & \text{for TE} \\ -(1-r_p)H_0 e^{jk_y y}\hat{y} & \text{for TM} \end{cases}. \quad (2.2.5)$$

In general, the continuity equation, which shows the relation between the induced charge and current, can be written as in integration form,

$$Q_{ind} = \frac{1}{j\omega}\oint \mathbf{J}\cdot\hat{\mathrm{n}}_{\mathrm{s}}\, dS, \quad (2.2.6)$$

where $\hat{\mathrm{n}}_{\mathrm{s}}$ denotes the surface normal unit vector for integrated surface. Since the surface currents do not flow normal to the metal surface, by assuming the surface currents effectively flow within the region of penetration depth as shown in (2.2.3), Eq. (2.2.6) can be replaced with the contour integral form of surface current density,

$$\rho_{ind} = Q_{ind}\delta = \frac{1}{j\omega}\oint \mathbf{K}\cdot\hat{\mathrm{n}}_l dl, \quad (2.2.7)$$

where $\hat{\mathrm{n}}_l$ and ρ_{ind} denote the normal unit vector for integrated line laid on surface of metal and induced surface charge density, respectively. Therefore, contour integral along the curve *l*, which is shown in Fig. 2.4, can lead to the expression of accumulated surface charge at the edges of nanoslit by using Eqs. (2.2.5) and (2.2.7), which are expressed as [49],

$$\rho_{TE}(y) = \pm\frac{\lambda}{i2\pi c}H_{inc}(1-r_s)\cos\theta_{inc}e^{jk_y y}, \quad (2.2.8a)$$

$$\rho_{TM}(y) \approx \frac{\lambda}{2\pi c}k_0\delta\tau H_{inc}(1-r_p)\sin\theta_{inc}e^{jk_y y}, \quad (2.2.8b)$$

where plus and minus signs of Eq. (2.2.8a) mean that the accumulated surface charges at each side of edge have opposite phases. The constant τ used in Eq. (2.2.8b) is a compensation factor determined by the geometry of nanoslit, which will be explained later.

From now, let me discuss about the physical meaning of these equations. The schematics in Figs. 2.2.2 and 2.2.3 show the directions of surface currents and the signs of induced surface charges for both polarization incidences.

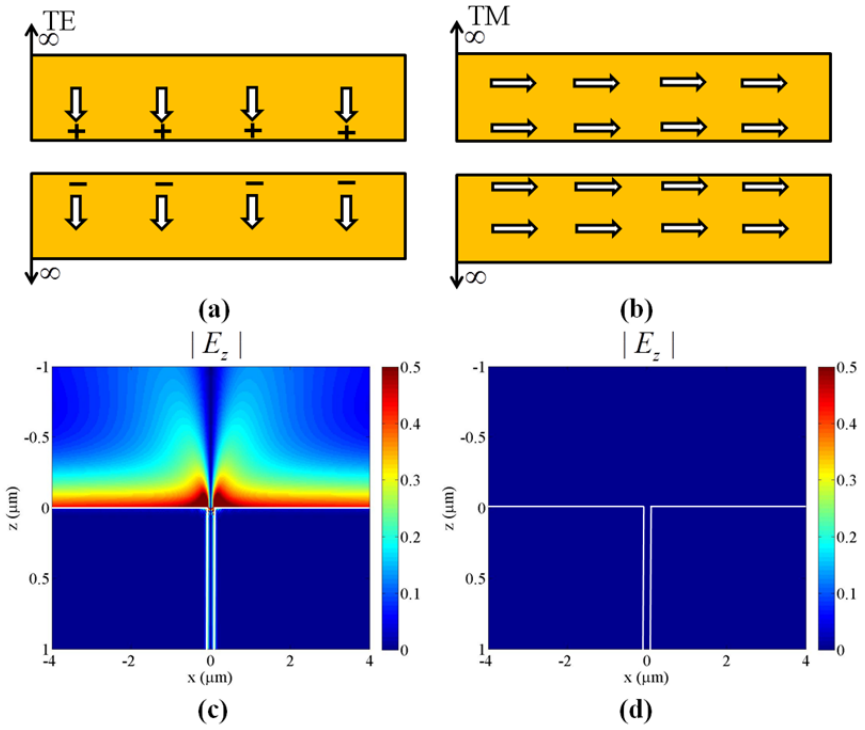

Figure 2.2.2. Directions of surface currents and the sign of induced surface charge when (a) TE or (b) TM polarized electromagnetic wave is normally illuminated. *z*-directional electric field distributions on the cross section of nanoslit (*x*-*z* plane) are shown for (c) TE and (d) TM polarization. Here, silver is used for metal substrate. Incident wavelength and slit width are set to 532 nm and 200 nm, respectively.

For the normal illumination case as shown in Fig. 2.2.2, surface currents direct to *x*-direction (perpendicular-to-slit) for TE polarized illumination, hence they uniformly accumulate the opposite sign surface charges at the edges of nanoslit. The amount of surface charge is proportional to incident wavelength (λ), which was explained by the lambda-zone effect for local

capacitor model in nanoslit geometry [51]. On the other hand, for TM polarized illumination, surface currents direct to the *y*-direction (parallel-to-slit) for overall region of illuminated metal surface. Although surface currents massively flow parallel-to-slit direction, they do not accumulate or oscillate surface charge near the edge of nanoslit, so they cannot generate SPPs from the nanoslit. This aspect is also shown in Eq. (2.2.8b) by substituting $\theta_{inc} = 0$. These characteristics of surface charge distribution have been well-known to the researchers on plasmonics as an origin of SPPs excitation from the nanoslit at normal incidence, and they also explain why parallel-to-slit (TM) polarized light cannot excite the SPPs for that case. In Figs. 2.2.2(c) and 2.2.2(d), amplitude of *z*-directional electric fields are shown for both polarization incidences, you cannot find any surface plasmon excitation for TM illumination in this case.

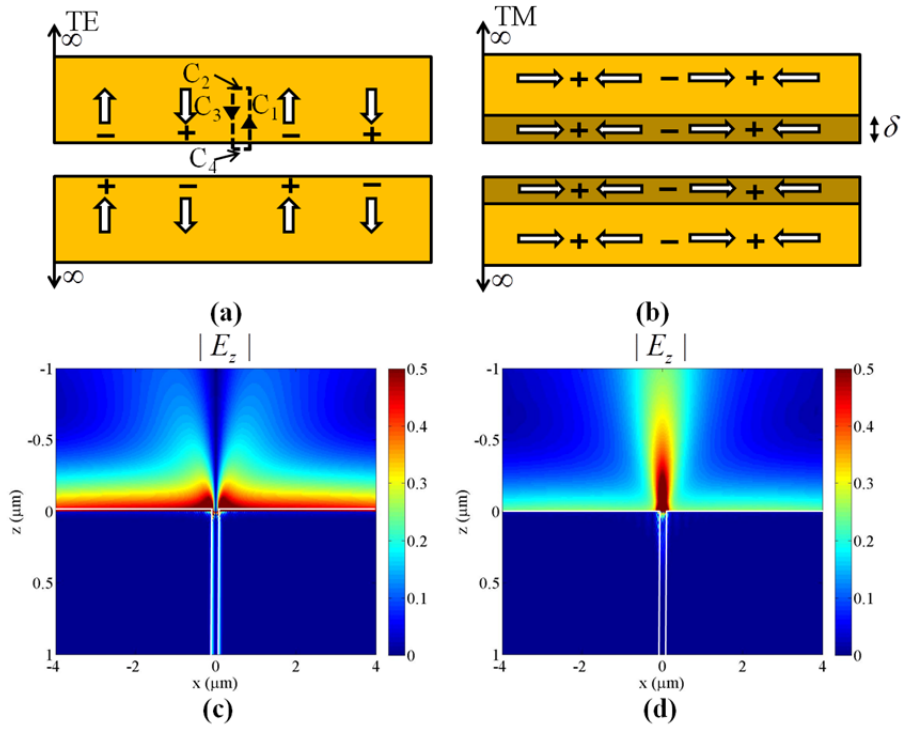

Figure 2.2.3. Directions of surface currents and the sign of induced surface charge when (a) TE or (b) TM polarized electromagnetic wave is obliquely illuminated. *z*-directional electric field distributions on the cross section of nanoslit (*x*-*z* plane) are shown for (c) TE and (d) TM polarization.

In contrast, Fig. 2.2.3 shows the case of oblique incidence, $\theta_{inc} \neq 0$. Due to the linear momentum carried by incident wave, surface currents are not uniform, but oscillate along the *y*-direction with the period of $\lambda_y = \lambda / \sin\theta_{inc}$. Therefore, accumulated charges for TE wave illumination case also changes its orientation as shown in Fig. 2.2.3(a). The amount of surface charges are simply decreased by the factor of $\cos\theta_{inc}$, which is caused by the amplitude variation of incident magnetic field shown in Eq. (2.2.5). However, for the case of TM wave illumination, periodic variation of surface current can generate the fluctuation of surface charge, like a transmission of longitudinal wave as shown in Fig. 2.2.3(b). The amount of oscillating surface charge increases when incident angle is increased by the factor of $\sin\theta_{inc}$ as shown in Eq. (2.2.8b). Therefore, SPPs can also be generated from TM polarization case in oblique incidence case. Generated SPPs are shown in Figs. 2.2.3(c) and 2.2.3(d), by observing the *z*-directional electric field. One more important feature is difference between the relative phases of induced charge with respect to the surface currents, which is directly accumulated for TE incidence case, whereas it has $\pi/2$ shift in TM incidence case. This feature is also understood by comparing the phase between the Eq. (2.2.8a) and (2.2.8b). Similar to the normal incidence, these surface currents exists on the overall region of illuminated surface of metal substrate. For TE wave illumination, contour integral only has nonzero value for C2 curve. Hence, accumulated surface charge is independent of the length of C1 or C3 curve. However, the oscillating surface charge inside the contour is proportional to the length of C1 or C3 for TM wave illumination, so it is not possible to directly say the all of the surface charge inside the contour is related to the excitation of SPPs. In practical, there should exist the region in which oscillating surface charge can affect the excitation of SPPs. In this dissertation, let me assume this effective length near the edge of nanoslit as a penetration depth (δ), and the error between this assumption and full numerical simulation is matched by adapting the compensation parameter τ , which will be calculated with the magnetic dipole model followed in next section.

2.2.1.2. Electric and magnetic dipole modeling of nanoslit

Analytical modeling of nanoslit excitation problem is one of fascinating issues to understand the SPPs excitation characteristics from nanoslit. As mentioned in previous section, charge of opposite signs are accumulated near the edges of slit when TE polarized wave is illuminated.

From such condition, strong electric fields are generated between the edges of slit so that many researchers have explained the TE polarization illumination case as a line electric dipole source aligned to the perpendicular-to-slit direction (*x*-direction) [47], as shown in Fig. 2.2.4.

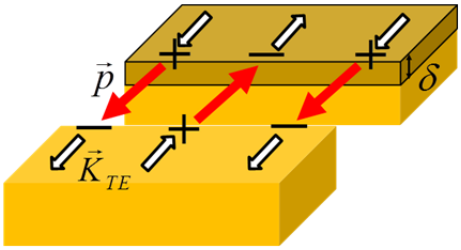

Figure 2.2.4. Schematic of electric line dipole model to explain the TE illumination.

According to these results, the amount of excited SPPs is proportional to that of the accumulated surface charge near the slit edge when slit width is far smaller than operating wavelength, which makes an electric line dipole source much stronger. The amplitude of electric line dipole source can be determined from the width of slit and accumulated surface charge,

$$\mathbf{p}_{TE}(y) = \rho_{TE}(y) w \hat{x}. \tag{2.2.9}$$

Here, $\rho_{TE}(y)$ is calculated in Eq. (2.2.8a) and *w* is the width of nanoslit. The expression in (2.2.9) has been often used for modeling the SPPs excited from nanoslit when TE polarized light is illuminated [51].

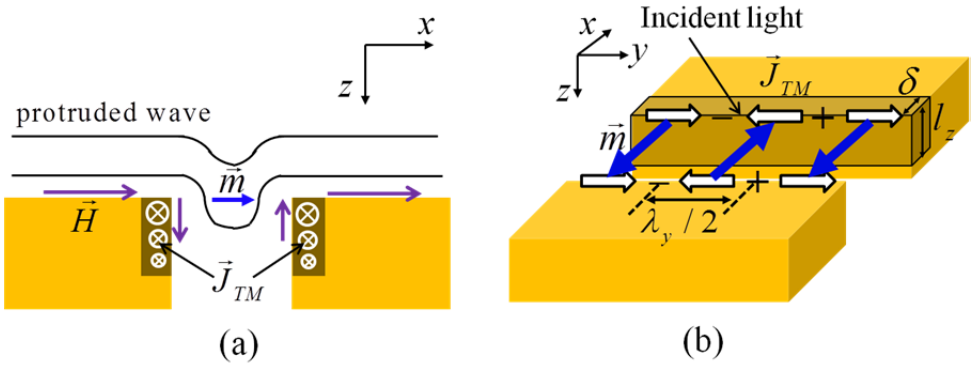

Figure 2.2.5. (a) Schematic diagram for illustrating the induction current generated by the protruded incident magnetic field. (b) Schematic of magnetic line dipole model to explain the TM illumination.

However, to the best of my knowledge, there was no research to model the case of TM polarized light illuminance since researchers do not consider that case can also excite the SPPs. In this dissertation, the author firstly model TM illumination case and predicts the amount of excited SPPs by using the magnetic line dipole source. In Fig. 2.2.5, schematic for explaining how magnetic dipole source can be formed by TM illumination case is illustrated.

Since the width of nanoslit is subwavelength scale, there is no propagating mode inside the nanoslit. However, fields can protrude within the nanoslit as shown in Fig. 2.2.5(a). Purple arrows laid on metal surface indicate the direction of incident magnetic fields at certain phase, and these protruded magnetic fields generate parallel-to-slit currents within the edge of nanoslit as discussed in previous section. The protrude length within the nanoslit (l_z), which is a function of slit width and incident wavelength, often has larger value than penetration depth. These currents act as double parallel wires and they can be expressed as magnetic dipole source **m** located at the center of slit on $z = 0$ plane by using the relation [52],

$$\mathbf{m} = \frac{1}{2}\int r' \times \mathbf{J}_{TMz}(r') dr'^3 \ . \tag{2.2.10}$$

Here, the y-directional integration region is considered for nearest current flow (For example, $-\lambda_y/4 < y < +\lambda_y/4$ for magnetic dipole located at $y = 0$) since this is more dominant than other flows far away from calculation point when the slit gap (w) is much smaller than the oscillation period (λ_y). From the assumption of the surface current source $\mathrm{Re}(\mathbf{J}_{TMz}) = |\mathbf{J}_{TMz}|\cos(k_y y')\hat{y}$ (uniformly distributed inside the shadowed region), cross product inside the integrand calculated for single side of slit can be expressed as

$$\vec{r}' \times \mathbf{J}_{TMz}(r') = \hat{x}\left(-|\mathbf{J}_{TMz}| z' \cos\left(\frac{2\pi}{\lambda_y} y'\right)\right) + \hat{z}\left(-|\mathbf{J}_{TMz}| x' \cos\left(\frac{2\pi}{\lambda_y} y'\right)\right), \tag{2.2.11}$$

where the primed coordinate ($\vec{r}'$) denotes the coordinate for current source.

After adding the currents from both sides of the slit, only the x-directional component is remained. Therefore the author can obtained the direction of magnetic dipole source as illustrated in Fig. 2.2.5(b),

$$\vec{r}' \times \mathbf{J}_{TMz}(r') = \hat{x}\left(-|\mathbf{J}_{TMz}| z' \cos\left(\frac{2\pi}{\lambda_y} y'\right)\right) \times 2. \tag{2.2.12}$$

Finally, integration along the considered region gives:

$$\begin{aligned}\left|\mathbf{m}\right| &= 2\left|\mathbf{J}_{TMz}\right| \times \frac{1}{2}\int_{w/2}^{w/2+\delta}\int_{-\lambda_y/4}^{+\lambda_y/4}\int_0^{l_z} \hat{x}z'\cos\left(\frac{2\pi}{\lambda_y}y'\right)dz'dy'dx' \\ &= 2\left(\frac{1}{2}\left|\mathbf{J}_{TMz}\right|\delta\frac{\lambda_y}{\pi}\frac{l_z^{\,2}}{2}\right).\end{aligned} \tag{2.2.13}$$

Due to the oblique incidence, magnetic line dipole source carries its own linear momentum as same as the case of electric line dipole source,

$$\mathbf{m} = \left|\mathbf{m}\right| e^{j\frac{2\pi}{\lambda_y}y}\hat{x}. \tag{2.2.14}$$

By assuming that the amplitude of radiated field from modeled magnetic line dipole source is equal to that of protruding incident magnetic fields near the slit edges, in quasi-static approximation due to the subwavelength scale of nanoslit, it is possible to obtain following relation,

$$\left|\mathbf{H}\right| = \frac{1}{2\pi}\frac{\left|\mathbf{m}\right|}{(w/2)^3}. \tag{2.2.15}$$

Then, by substituting Eqs. (2.20b) and (2.25) into (2.26) gives us an expression of compensation factor τ ,

$$\tau = \frac{4\pi^2(w/2)^3}{\lambda_y l_z^{\,2}}. \tag{2.2.16}$$

Note that the compensation factor is a dimensionless parameter which is increasing with the incident angle (decrease of λ_y). It is also acceptable that effective region for excited SPPs from nanoslit for TM polarization is increased when width of slit becomes wider. The value of compensation factor is nearly in unity value for our experimental condition, which will be followed in next section.

From now, analyses on the field radiation characteristics from those electric and magnetic line dipole sources are shown by using the Green's dyadic formulations. Assuming the case of line dipole source is located slightly above the flat metal boundary at z=0 plane, the radiated field from line dipole source in such geometry can be expressed by the summation of two radiation terms: one is the radiation from the source without any reflection from the metal plane, and the other is the radiating field after bouncing the metal surface. Therefore, field radiated by the electric or magnetic dipole source located above the metal interface can be expressed as,

$$\mathbf{U}_{\Phi}(r) = \omega^2 \eta \int (\vec{\mathbf{G}}_{0,U}(\vec{r},\vec{r}') + \vec{\mathbf{G}}_{S,U}(\vec{r},\vec{r}')) \cdot \mathbf{s}(\vec{r}')dr', \tag{2.2.17}$$

where $\mathbf{U}$ is either $\mathbf{E}$ or $\mathbf{H}$, η is ε or μ, Φ is TE or TM, and $\mathbf{s}$ is $\mathbf{p}$ or $\mathbf{m}$ for electric or magnetic line dipole source, respectively. The first term of integrand, $\vec{\mathbf{G}}_{0,U}(\vec{r},\vec{r}')$ denotes the free space Green's dyadic tensors, and they are identical both for electric and magnetic dipole cases,

$$\vec{\mathbf{G}}_{0,E}(\vec{r},\vec{r}') = \vec{\mathbf{G}}_{0,H}(\vec{r},\vec{r}') = j\frac{1}{k_0^{\,2}}\int_{-\infty}^{\infty} dk_x \frac{1}{k_z}\begin{bmatrix} k_0^{\,2}-k_x^{\,2} & -k_x k_y & -k_x k_z \\ -k_x k_y & k_0^{\,2}-k_y^{\,2} & -k_y k_z \\ -k_x k_z & -k_y k_z & k_0^{\,2}-k_z^{\,2} \end{bmatrix}\Psi, \tag{2.2.18}$$

whereas the second term of integrand, which contains the radiation from the metal surface after bounching and evanesecnt surface modes, should be modified due to the different reflection characteristic in metal substrate for each dipole sources. The surface Green dyadic $\vec{\mathbf{G}}_S(\vec{r},\vec{r}')$ represents the linear combination of Fresnel's reflection coefficient and decomposed free space Green dyadic,

$$\vec{\mathbf{G}}_{S,E}(\vec{r},\vec{r}') = i\frac{1}{k_0^{\,2}}\int_{-\infty}^{\infty} dk_x(\vec{\mathbf{M}}_p r_p + \vec{\mathbf{M}}_s r_s)\Psi, \tag{2.2.19a}$$

$$\vec{\mathbf{G}}_{S,H}(\vec{r},\vec{r}') = -i\frac{1}{k_0^{\,2}}\int_{-\infty}^{\infty} dk_x(\vec{\mathbf{M}}_p r_s + \vec{\mathbf{M}}_s r_p)\Psi. \tag{2.2.19b}$$

Here, since our configuration is done in infinite length of slit for *y*-direction, *y*-directional momentum k_y can be treated as a constant of $k_y = k_0 \sin\theta_{inc}$, where $\vec{\mathbf{M}}_p$ and $\vec{\mathbf{M}}_s$ denote the 3×3 Green's tensor for corresponding polarization:

$$\vec{\mathbf{M}}_p = \frac{1}{(k_x^{\,2}+k_y^{\,2})}\begin{bmatrix} k_x^{\,2}k_z & k_x k_y k_z & -k_x(k_x^{\,2}+k_y^{\,2}) \\ k_x k_y k_z & k_y^{\,2}k_z & -k_y(k_x^{\,2}+k_y^{\,2}) \\ -k_x(k_x^{\,2}+k_y^{\,2}) & -k_y(k_x^{\,2}+k_y^{\,2}) & (k_x^{\,2}+k_y^{\,2})^2/k_z \end{bmatrix}, \tag{2.2.20a}$$

$$\vec{\mathbf{M}}_s = \frac{k_0^{\,2}}{(k_x^{\,2}+k_y^{\,2})k_z}\begin{bmatrix} k_y^{\,2} & -k_x k_y & 0 \\ -k_x k_y & k_x^{\,2} & 0 \\ 0 & 0 & 0 \end{bmatrix}, \tag{2.2.20b}$$

and the retarded phase profile Ψ is given as $\Psi = \exp\{i[k_x(x-x') + k_y(y-y') + k_z|z-z'|]\}$.

By using the Green's dyadic tensors, it is possible to calculate all of *x*-, *y*-, and *z*- components of the radiating electric (or magnetic) field generated from the electric dipole (or magnetic dipole) line source which has *x*-, *y*-, and *z*- components. Since the dipole sources are only arranged to *x*-

direction for our analysis as depicted in Eqs. (2.2.9) amd (2.2.17), only the first column of Green's dyadic tensor is used. From the Eq. (2.2.18), it is possible to directly obtain the electric field of TE incidence case. On the other hand, magnetic fields are firstly obtained for TM incidence case. Electric fields for TM incidence case are calculated from the magnetic fields by using the Maxwell's curl equation $\nabla \times \vec{H}_{TMz} = -i\omega\varepsilon\vec{E}_{TMz}$.

2.2.2. Simulations for unidirectional launching from nanoslit

To verify our induced charge and magnetic line dipole models, comparison between the analytic results and the full electromagnetic field simulations based on rigorous coupled wave analysis (RCWA) is shown. RCWA is a kind of Fourier modal method (FMM), which finds the coupling coefficients between the eigenmodes of layered system [53].

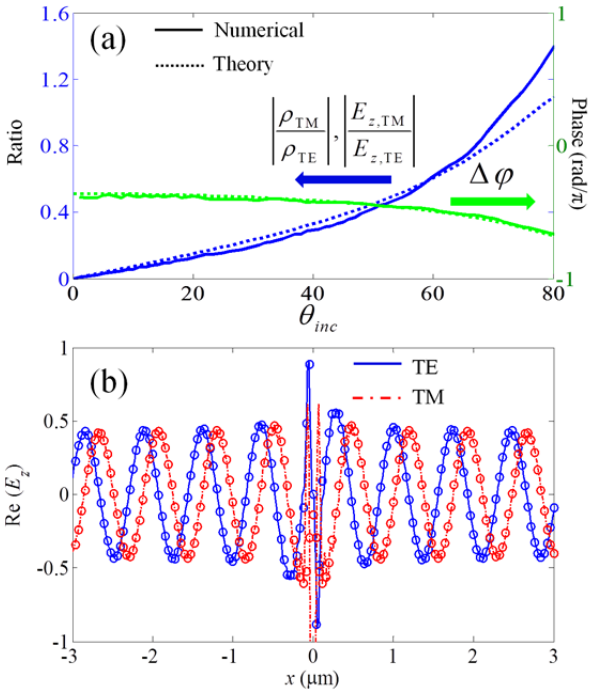

Figure 2.2.6. (a) The amplitude ratio and phase difference of excited SPPs between TE and TM illumination cases are compared. (b) RCWA results of E_z field distribution at 2 nm above the metal surface are compared with line dipole model.

This method is advantageous since it can selectively turn on or off the specific eigenmodes of certain layer. For example, it is possible to only see the evanescent modes by turning off the eigenmodes which have real propagation numbers. Therefore, it is quite useful to observe the SPP mode without considering incident or reflected wave, which is appropriate for our purpose.

Firstly, to show the amplitude and phase of induced charge is proportional to those of excited SPPs from nanoslit, they are compared in Fig. 2.2.6(a). The solid lines are numerical results calculated by RCWA that measure the amount of excited SPPs 4 μm away from nanoslit. Dotted lines are theoretical results of induced surface charges which are calculated from Eqs. (2.2.8a) and (2.2.8b). The amplitude ratios (TM/TE) for both numerical and theoretical results are rapidly increased when incident angle increases as expected in previous section. It originates from the decrease (or increase) of induced surface charge near the slit edges for TE (or TM) polarization illumination. On the other hand, phase differences are changed smoothly near the value of 0.5π (rad). Such characteristics are also predicted by induced charge model that was shown in Eqs. (2.2.8a) and (2.2.8b). Decrease of phase difference plot originates from the phase change of the Fresnel reflection coefficients, r_s and r_p.

Next, to check whether the surface fields generated from nanoslit are well-matched to the radiated fields calculated from line dipole model, they are compared in Fig. 2.2.6(b). Blue solid and red dotted lines indicate the numerically calculated *z*-directional electric field profile along 2 nm above the metal surface for TE and TM polarization cases done by RCWA. Markers drawn in the same figure are analytically calculated results done by Green's dyadic function discussed in previous sections. Other conditions are set to the following values: λ_0 = 532 nm, ε_{Ag} = -10.19 + $0.83j$, and w = 100 nm. As can be seen from these results, the analytical calculations based on the proposed line dipole model are in excellent agreement with the numerical results.

From these simulation results, one important feature for utilizing the unidirectional launching of SPPs is revealed as well as the verification of proposed model. Since the phase of excited SPPs from nanoslit follows that of induced charge, it is notable that TE polarized light can generate anti-symmetric SPP profile from nanoslit whereas TM polarized light generates symmetric one. This feature is also checked in the radiation from electric or magnetic line dipole moment, which is shown in Fig. 2.2.6(b). The opposite phase parity of SPPs caused by two orthogonal polarizations is the key principle for unidirectional excitation of SPPs.

Now, let me consider the case that TE and TM polarizations are simultaneously illuminated to the nanoslit. From the numerical calculation done in Fig. 2.2.6(a), the amplitude ratio and phase

difference of excited SPPs for each of TE and TM polarization case are already known. Due to the phase parity of excited SPPs, resulting excitations of SPPs for each side of slit operate in opposite ways: one side is canceled out and the other side is reinforced. The conceptual schematic for such situation is drawn in Fig. 2.2.7(a).

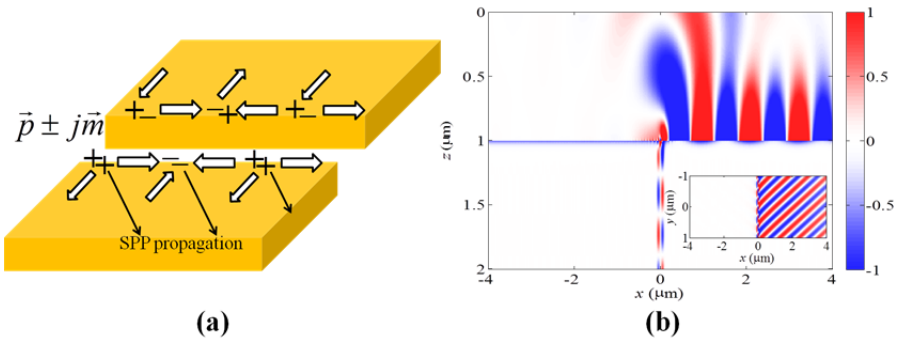

Figure 2.2.7. (a) Directions of surface currents and the sign of induced surface charge when TE and TM polarized lights are simultaneously illuminated. (b) E_z field distribution along the *x*-*z* plane at optimized polarization state for right-side unidirectional launching which has incident angle of $\theta_{inc} = 50°$ and incident polarization state of $(E_{TE},\ E_{TM}) = (1,\ 2j)$.

In the viewpoint of surface charge, appropriate composition of symmetric and anti-symmetric distribution of surface charge can lead to the unidirectional launching of SPPs. To achieve that, the amplitude ratio and phase difference between TE and TM illuminations are precisely compensated to cancel the single side of SPP excitation. A *z*-directional electric field distribution of optimized case (perfectly cancels the single side launching) is shown in Fig. 2.2.7(b). To clearly show the SPPs on the metal surface, incident field components are removed. According to the plot shown in Fig. 2.2.6(a), the optimized polarization state for right-side unidirectional launching at incident angle of $\theta_{inc} = 50°$ is obtained as $(E_{TE},\ E_{TM}) = (1,\ 2j)$, whereas launching direction of SPPs can be switched to left direction when polarization state is changed to $(E_{TE},\ E_{TM}) = (1,\ -2j)$.

To check the variation of unidirectional launching condition respect with the incident angle, let me show the result of unidirectional ratio for various incident angles, which is defined as the ratio of the intensity of the SPPs excited on the left-side of the slit compared to that for the right-side in

Fig. 2.2.8. As shown in Fig. 2.2.8(b), unidirectional launching does not appear for normal incidence since TM mode cannot attribute to the SPP excitation. However, when the incident angle starts to tilt, at the condition of 20° (Fig. 2.2.8(c)), unidirectional launching conditions for left and right sides simultaneously appear near the TM polarization state. This is because SPP coupling efficiency of TM mode is not yet strong enough compared to that of TE mode, so strong TM component is needed to compensate the difference of coupling efficiency. Then they are moved toward the poles of Poincaré sphere, which means LCP and RCP condition. In this region, the maximum efficiency for unidirectional coupling is also achieved (Figs. 2.2.8(d) and 2.2.8(e)). Then finally, the condition for 80° incident angle is shown in Fig. 2.2.8(f), and it clearly shows that the unidirectional conditions are moved to near TE polarization state.

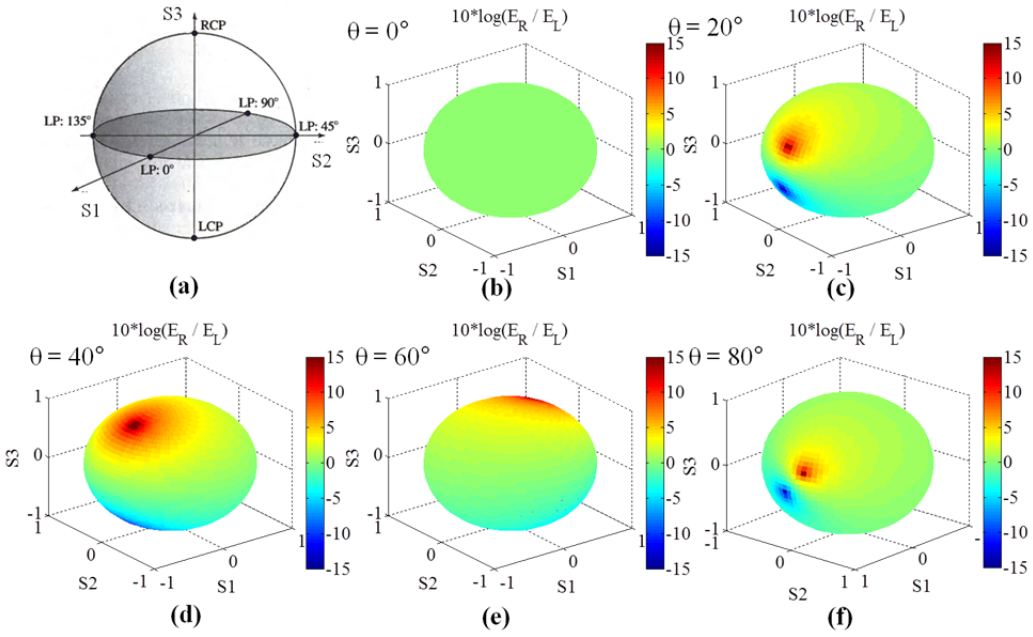

Figure 2.2.8. The unidirectional ratio parameter is shown on the map of Poincaré sphere for various incident angles : (a) 0°, (b) 20°, (c) 40°, (d) 60°, and (e) 80°. Note that the axis of S1 is reversed in (e).

Until now, the modeling of unidirectional launching phenomenon on the nanoslit which can be changed by incident polarization modulation is done. For the clear explanation of our magnetic induction current model, half-infinite thickness of metal substrate is assumed and excited SPPs are

generated at the reflection side of nanoslit. However, for the experimental demonstration, it is not so easy to completely separate the SPPs at the reflection side from the large noise signals such as incident field, quasi-cylindrical waves, and scattered field from the unwanted particles which are excited from the incident field. Therefore, it is necessary to re-design the structure which can generate SPPs unidirectionally at the transmission side of nanoslit.

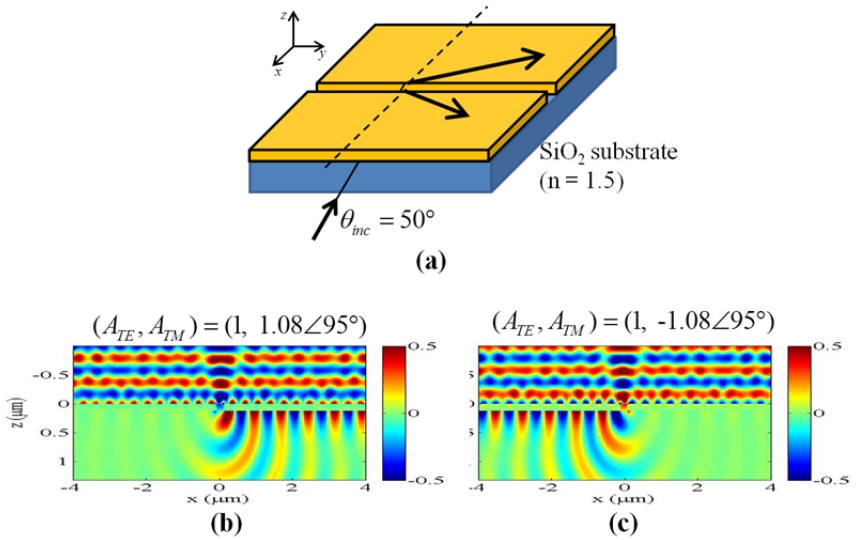

Figure 2.2.9. (a) Configuration of polarization-sensitive unidirectional launching of SPPs in transmission type which is designed for practical experiment. E_z field distributions along the *x*-z plane at optimized polarization state for (b) right-side and (c) left-side unidirectional conditions are shown.

Fig. 2.2.9 shows the schematic diagram and simulation results for unidirectional launching from nanoslit structure in transmission side of nanoslit. Similar to reflection type shown in Fig. 2.2.7, the amplitude ratio and phase difference of excited SPPs at the transmission side both for TE and TM polarization states are calculated, and they are superposed with appropriate Jones vector conditions to make a perfect destructive interference at the single side of nanoslit. Note that the incident layer is SiO_2 substrate (n = 1.5), the width and thickness of nanoslit are set to 200 nm and 120 nm, respectively. The value of slit width is precisely chosen not to permit a propagating photonic mode caused by TM illumination to avoid a Fabri-Perot resonance caused by finite thickness of nanoslit. Moreover, the thickness of slit is also important since it should not only have enough thickness to block the direct tunneling of incident field but also be sufficiently thin to

allow the protruded field can generate the SPPs at the transmission side even though there is no propagating mode caused by TM polarization. These simulation conditions will be also used in experiment which will be followed in next subsection.

2.2.3. Experimental demonstration for polarization-modulated plasmonic switching

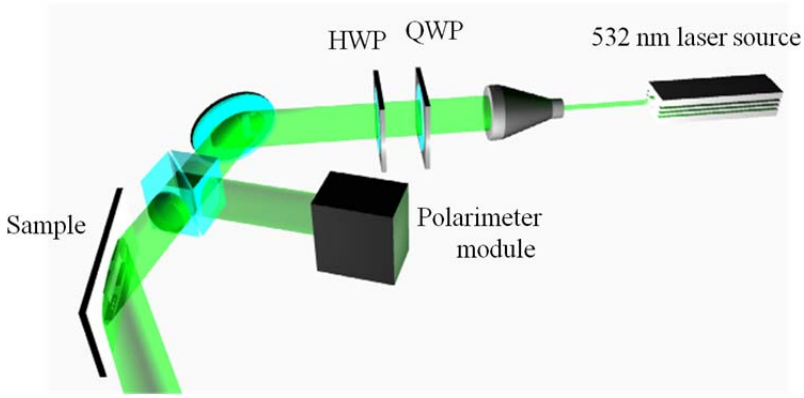

Figure 2.2.10. Experimental configuration for unidirectional launching of SPPs caused by polarization modulation.

In Fig. 2.2.10, experimental configuration for unidirectional launching of SPPs caused by polarization modulation is illustrated. 200 nm-width, and 25 μm-length of nanoslit sample is carved on 120 nm thickness of Ag layer by Focused Ion Beam (FEI, Quanta 200) machine and the film is evaporated by E-beam evaporator. For the precise measurement of input polarization, high-resolution polarimeter module (Thorlabs, PAN5710VIS) is used for the detection of input polarization state before it is illuminated to the sample. The detection of surface plasmon field was simply done by capturing the far-field image over the transmission side of slit by using the charged coupled device (CCD), which can measure the scattered field of SPPs from the small roughness of metal surfaces.

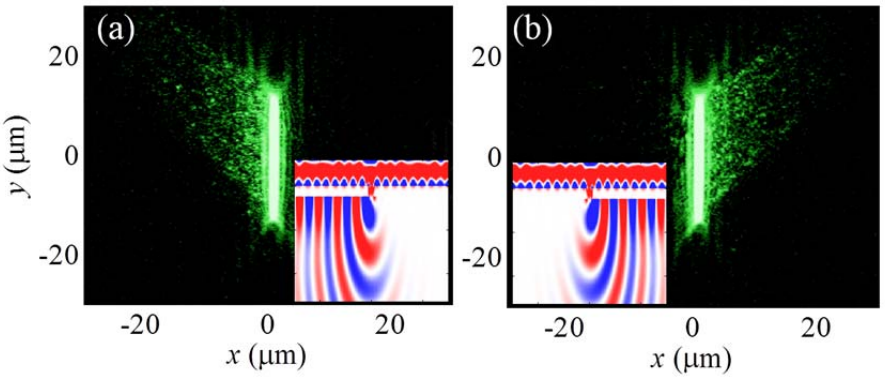

Figure 2.2.11. CCD images at the surface of the slit carved on thin metal plate for (a) RCP and (b) LCP light illumination conditions.

In Figs. 2.2.11(a) and (b), the CCD images for RCP and LCP light illuminations are shown, respectively. In the inset of each figure, corresponding numerical results are shown. To compare the theory, numerical simulation and experimental results simultaneously, the incident polarization state is changed along the vertical circular path of Poincaré sphere as shown in the inset of the plot depicted in Fig. 2.2.12. By changing the polarization elipticity χ, the unidirectional ratio (U) is plotted. The value of U is defined as the ratio of the intensity of the SPPs excited on the left-side of the slit ($|E_L|^2$) compared to that for the right-side ($|E_R|^2$), for numerical simulation and experimental results. In theoretical plot, it is defined by analytic form which can be written as,

$$U = \frac{\left|\rho_{TM} A_{TM} - \rho_{TE} A_{TE}\right|^2}{\left|\rho_{TM} A_{TM} + \rho_{TE} A_{TE}\right|^2}. \tag{2.2.21}$$

Here, the numerator and denominator, which are given as the linear combinations of line charge density and the incident polarization Jones vectors, analytically denote the amount of excited SPPs at the left and right side of the slit, respectively.

To precisely measure the variation of unidirectional ratio according to the incident polarization state, CCD images are captured with the variation of polarization elipticity χ. The theoretical, numerical and experimental results are simultaneously compared in the plot of Fig. 2.2.12.

Table 2.1. Experimental results for various incident polarization states.

Polarization state (χ)	Image	Unidirectional ratio (dB)	Polarization state (χ)	Image	Unidirectional ratio (dB)
TE (χ = 0°)	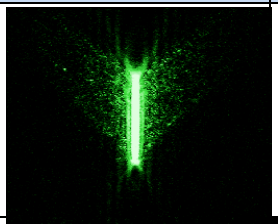	-0.84	TM (χ = 90°)	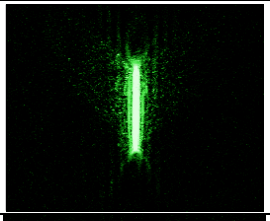	0.12
(χ = 30°)	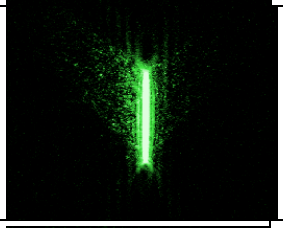	9.59	(χ = 120°)	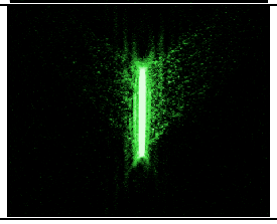	-12.84
RCP (χ = 45°)	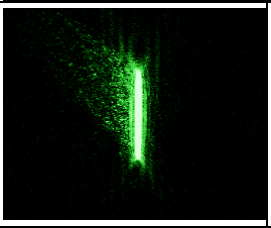	22.59	LCP (χ = 135°)	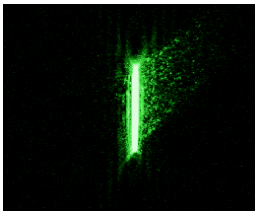	-15.68
(χ = 60°)	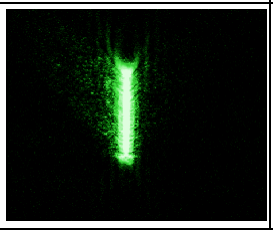	13.67	(χ = 150°)	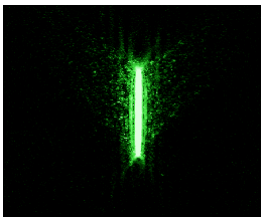	-9.29

By gradually changing the polarization state from TE, RCP, TM, LCP, and back to the TE state, the results show that the highest unidirectional ratio is obtained near the RCP state, whereas the inverse peak is located near the LCP state as predicted by our analytic model.

Furthermore, the experimental results of representative polarization states are summarized in Table 2.1 to provide an evidence of my experimental results. Corresponding Jones vector of incident polarization state and the unidirectional ratio at those conditions are given with the CCD images.

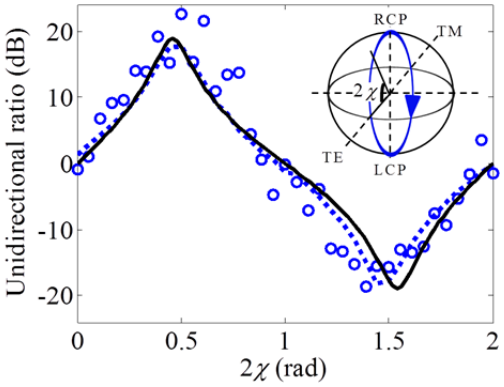

Figure 2.2.12. Theoretical (solid black line), numerical (dotted blue line) and experimental (markers) results of unidirectional ratios are compared simultaneously.

In order to check that the oblique propagation from nanoslit shown in CCD images originates from a scattering from the small roughness at the metal surface, not from far-field diffraction at nanoslit, numerically calculated near- and far-field distributions above the metal nanoslit are shown for various heights in Fig. 2.2.13. Representatively, near-field image which is observed 0 μm above the metal surface is shown in Fig. 2.2.13(a). It is shown that unidirectional propagation of electromagnetic field is clearly shown for this figure, which is propagating tens of micrometers from the center slit. However, when the observing point is getting higher from the surface, far-field radiation has almost symmetric field intensity distribution as shown in Figs 2.2.13(b)-2.2.13(d), which means it is not significantly affected by near-field pattern. Therefore, it is quite difficult to think that unidirectionally launched field patterns shown in the experimental results are caused by direct far-field radiation from the nanoslit. The field distribution shows that far-field radiation cannot generate a clear unidirectional pattern as depicted in the CCD images shown in Fig. 2.2.12 and Table 2.1.

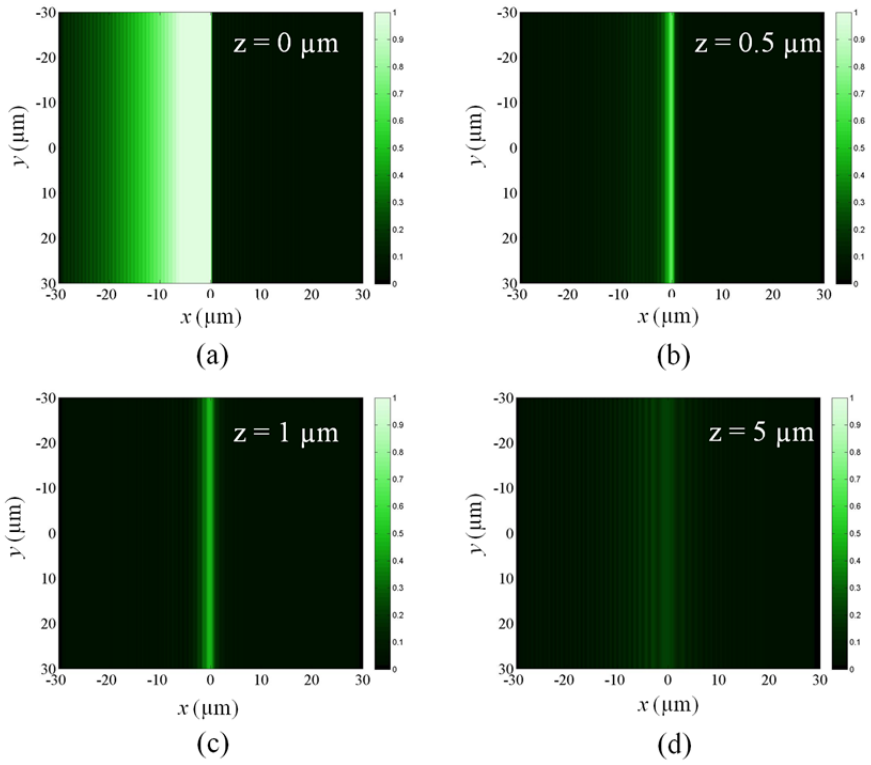

Figure 2.2.13. Near- and far-field intensity distribution observed above the various heights from the metal surface. The distance between metal surface and observed plane is set to (a) 0 μm, (b) 0.5 μm, (c) 1 μm, and (d) 5 μm, respectively.

2.3. Demonstration of phase-modulated SPP excitation from nanoslit

In section 2.2, the excitation characteristics of SPPs from nanoslit caused by two orthogonal polarization states were discussed, and a novel method for switching the launching direction of SPPs which can be controlled by polarization modulation was also demonstrated both in theory and experiment. However, an active change of a polarization state of light, which can be done by using anisotropic materials such as liquid crystal, is hard to apply to switching devices in practice due to the slow response speed. Moreover, tilted propagation from nanoslit, which is caused by

the parallel-to-slit linear momentum of incident light, will decrease the effective propagation length of SPPs, which is measured normally from the nanoslit.

To solve these problems, an interference pattern of two obliquely illuminated beams is used which can dramatically change the direction of SPP excitations in this chapter. By adjusting the relative location between nodal line of interference pattern and center of nanoslit, SPPs excited from nanoslit can be selected to either symmetric or anti-symmetric mode. Then, by optimizing the nanoslit geometry, coupling efficiencies of symmetric and anti-symmetric plasmonic modes are set to nearly equal scale. Finally, by interfering the excited SPPs from two coupled modes, directional switching of SPPs which can be modulated by relative phase difference between two incident beams is proposed. Here, the left-to-right unidirectional launching ratio is obtained up to 28 dB in experiment, and launching direction of SPPs is also perpendicular to slit.

2.3.1. Principle of phase-modulated directional launching by two beam interference

As shown in section 2.2, the excitation of SPPs from nanoslit is significantly related to the induced surface currents and charge profile near the edge of nanoslit. Moreover, it is also shown that unidirectional launching of SPPs can be achieved when charges at the single edge of nanoslit are perfectly canceled somehow. In previous chapter, such cancellation is done by superposing two orthogonal polarization states: TE and TM illumination which generates anti-symmetric and symmetric charge distribution near the slit edges, respectively.

In this section, similar charge parities are achieved by a different principle, which is an illumination of two beams forming a parallel-to-slit interference pattern. In Fig. 2.3.1, schematics for explaining the SPP excitation characteristics when two oblique beams illuminate the nanoslit are shown. Two incident beams are illuminating the slit with the incidence angle of θ_{inc} and $-\theta_{\mathrm{inc}}$. The polarization of incident light is fixed in this case, to have only E_x, H_y, and E_z electromagnetic components as shown in Figs. 2.3.1(a) and 2.3.1(b).

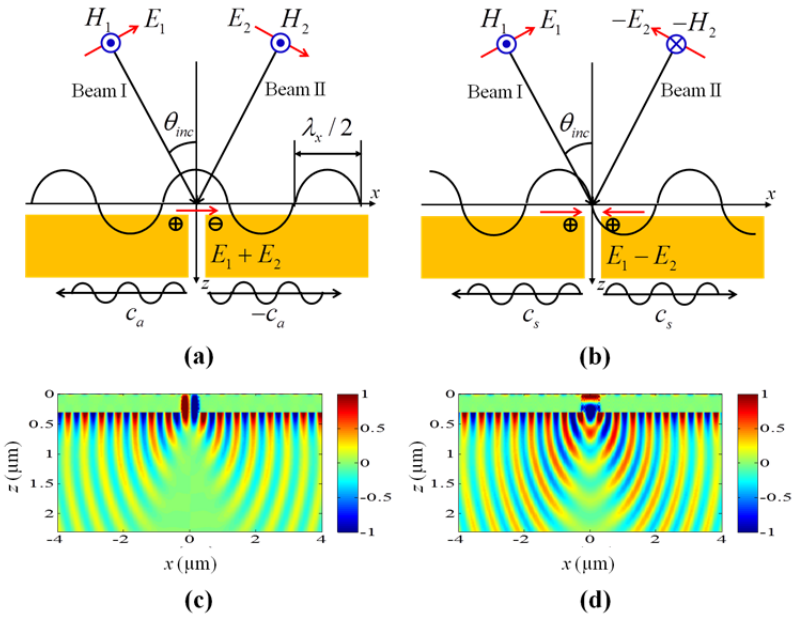

Figure 2.3.1. Schematic diagrams for explaining the aspect of excited SPPs according to the relative phase difference between two incident beams: (a) zero-phase and (b) π-phase difference. E_z field distribution of SPPs excited from the nanoslit along the *x*-*z* plane when two beams are illuminated: (c) zero-phase and (d) π-phase difference cases.

When ignoring the diffractions caused by nanoslit, it is possible to think two incident beams form an interference pattern which has periodic nodal line with a period of $\lambda_x / 2$, where λ_x is defined as $\lambda_x = 2\pi / k_0 \sin\theta_{inc}$. From now, let me consider the sign of accumulated charge near the slit edge with respect to the relative location between the nodal line of interference pattern and center of slit. The location of the nodal lines of the standing wave could be shifted when the phase difference between Beam I (reference beam) and Beam II (control beam) is changed. Schematic shown in Fig. 2.3.1(a) shows the status when Beam I and Beam II are in-phase state, so that the belly of interference pattern (of E_x and H_y components) is positioned just above the center of nanoslit. In that case, strong E_x field above the slit can accumulate the surface charge; this permits the slit can act as a local capacitor [51], which means charges with opposite signs are induced across the slit, as shown in the Fig. 2.3.1(a). In this circumstance, it is noted that symmetric MIM

plasmonic mode is always excited inside the nanoslit since this mode is a fundamental plasmonic mode in MIM waveguide which does not have cutoff frequency.

On the other hand, consider the condition when Beam I and Beam II are in opposite-phase states. In this case, the nodal line of interference pattern (of E_x and H_y components) is directly positioned above the center of nanoslit. Therefore, electric field (E_x) above the slit has opposite direction at each edge of nanoslit, and it accumulates the same sign of surface charge. If the thickness of nanoslit is sufficiently thick enough to permit the anti-symmetric plasmonic mode, such charge accumulation can generate the anti-symmetric plasmonic mode inside the nanoslit. The aspects of plasmonic modes excited inside the nanoslit are shown in Fig. 2.3.2 by changing the phase difference between Beam I and Beam II. Here, the thickness of slit is assumed to half infinite in order to ignore the Fabry-Perot resonance caused by reflection at the end of nanoslit.

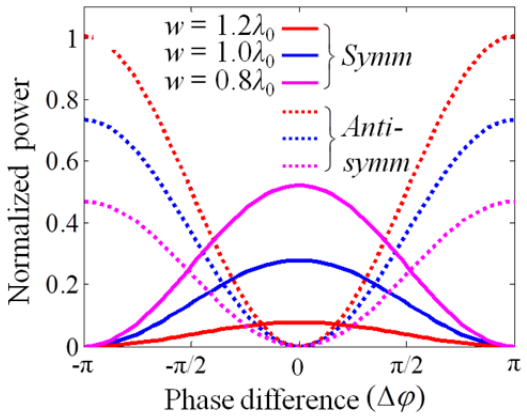

Figure 2.3.2. Power coupled to symmetric and anti-symmetric plasmonic mode when two oblique beams are illuminated with different phases.

It is shown that only the symmetric plasmonic mode is coupled for zero-phase difference whereas it perfectly vanished for π phase difference regardless to the width of nanoslit. When the thickness of nanoslit becomes finite, propagating SPPs are generated at the transmission side of nanoslit. Due to the symmetry of each mode, excited SPPs also have anti-symmetric or symmetric profile after coupling from MIM plasmonic mode to SPPs at the transmitted metal surface. Here, symmetric MIM plasmonic mode has anti-symmetric charge symmetry, so excited SPPs at the end of nanoslit have anti-symmetric initial phase as shown in Fig. 2.3.1(c). On the other hand, anti-

symmetric MIM plasmonic mode has symmetric charge distribution so that it generates SPPs at the end of nanoslit with symmetric initial phase as shown in Fig. 2.3.1(d).

Similar to the principle of unidirectional launching introduced in section 2.2, it is possible to perfectly cancel the single side of SPP excitation by destructive interference of both excitation types illustrated in Figs. 2.3.1(a) and 2.3.1(b). However, to find a practical condition for unidirectional launching which can be switched without any amplitude modulation, optimization of unidirectional condition should be performed before the experimental demonstration.

2.3.2. Simulation processes for optimized unidirectional condition

According to the notation illustrated in Fig. 2.3.1, a coupling ratio for anti-symmetric (c_a) and symmetric (c_s) SPPs excitation caused by zero-phase and π-phase difference cases is defined. These values are set to the amplitude of SPPs at the transmitted side of metal surface 4-μm away from the center of nanoslit, and normalized by the amplitude of incident field. For the perfect unidirectional launching of SPPs, one side of excited SPPs should be canceled out by destructive interference. Such conditions can be obtained for each side of slit by appropriately summing the anti-symmetric and symmetric coupling together. By calculating the value of coupling ratio c_a and c_s numerically, the left-side unidirectional (right-side canceled) excitation condition is achieved when the amplitude and phase of Beam II satisfy the following condition:

$$E_2 = \frac{(c_s - c_a)}{(c_s + c_a)} E_1 = U_L E_1 . \tag{2.3.1}$$

Similarly, right-side unidirectional (left-side canceled) condition can be expressed as

$$E_2 = \frac{(c_s + c_a)}{(c_s - c_a)} E_1 = U_R E_1 . \tag{2.3.2}$$

In general case, U_L and U_R are arbitrary complex numbers, which are inversely related to each other, so both the amplitude and phase of Beam II should be changed simultaneously when direction of SPP launching is switched from left to right. Such simultaneous and precise amplitude modulation of Beam II creates significant difficulties in terms of experimental demonstration. However, when slit conditions which have the relation of $|U_L| = |U_R| = 1$ are found, switching the direction of SPP launching can be achieved by simply changing the phase difference between Beam I and Beam II without any amplitude modulations. Simple calculations

indicate that such a condition is achieved when the phase difference between two SPP coupling coefficients is identical to $\pm 90°$, which can be expressed as

$$\angle\left(\frac{c_s}{c_a}\right) = \pm\frac{\pi}{2},\ |c_s| \neq 0,\ |c_a| \neq 0\,. \tag{2.3.3}$$

When the condition of Eq. (2.3.3) is satisfied, left or right side unidirectional launching is achieved when the phase difference of two beams satisfies

$$\varphi = \pi \pm 2\tan^{-1}\left(\left|\frac{c_s}{c_a}\right|\right), \tag{2.3.4}$$

where, plus (minus) sign for phase difference indicates right (left) side of unidirectional launching respectively, with the case of $\angle(c_s / c_a) = +\pi/2$, and the sign is reversed for the case of $\angle(c_s / c_a) = -\pi/2$.

Until now, the analytic condition for unidirectional launching without amplitude modulation of incident beam is discussed. Since the coupling coefficients c_a and c_s are quite sensitive to the geometric parameter of nanoslit such as slit width and thickness, parametric sweep for finding the optimized condition, which can satisfy the Eq. (2.3.3), should be performed.

For numerical analyses, RCWA method is used to determine the coupling coefficients for various conditions of nanoslit geometry. To consider the practical example which can be applied to the experimental demonstration, simulations were done with the thin metal film deposited on a half infinite SiO_2 substrate. 2 μm-thick perfect matched layer (PML) is used to prevent the periodicity problem of an RCWA simulation. The refractive index of the incident SiO_2 layer is set to 1.5 to consider the substrate used in the experimental part. The incident angle is also fixed to $\theta_{inc} = 28.1°$ in the SiO_2 substrate, which is calculated from Snell's law with an illumination angle of 45 degrees in free space. The incident wavelength is set to 532 nm, the overall period of the calculation is 20 μm, and silver is used for the thin metal film layer.

To find an optimized condition which can modulate the direction of SPPs only with phase modulations, the coupling ratios of anti-symmetric and symmetric SPPs excitations are shown in Fig. 2.3.3 varying with the slit width and thickness. It is shown that the coupling ratios are periodically changed with the variation in slit thickness (which can be observed when the slit width is in the single SPP mode regime), which originate from Fabry-Perot resonance inside the slit layer [54, 55]. Moreover, it is also shown that the SPP coupling coefficients are much more sensitive to a variation in slit width rather than that of slit thickness.

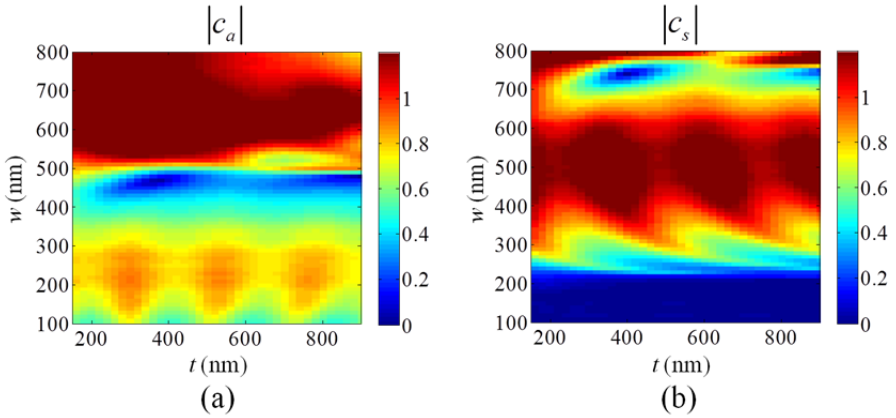

Figure 2.3.3. Power coupled to single interface SPPs at the transmission side of nanoslit caused by two beams with (a) zero-phase and (b) π-phase difference are shown for various slit-widths and slit thicknesses.

Due to the cutoff condition of anti-symmetric plasmonic mode, it is shown that the amount of excited SPPs coupled by opposite incident phases is nearly zero below a slit width of 250 nm. Below this condition, it is not possible to make a unidirectional launching of SPPs at the transmission side of nanoslit by coupling the anti-symmetric MIM plasmonic mode. Therefore, to achieve the unidirectional launching of SPP by adding both symmetrically and anti-symmetrically excited SPPs, we should avoid too narrow slit thickness below the cutoff condition due to the fact that the value of c_s is nearly zero. Otherwise, it is possible to make a unidirectional launching at the reflection side of nanoslit. However, as discussed in section 2.2, experimental detection of SPPs at the reflection side of nanoslit is quite difficult since incident and directly reflected beams act as a noise signal in practical experiment.

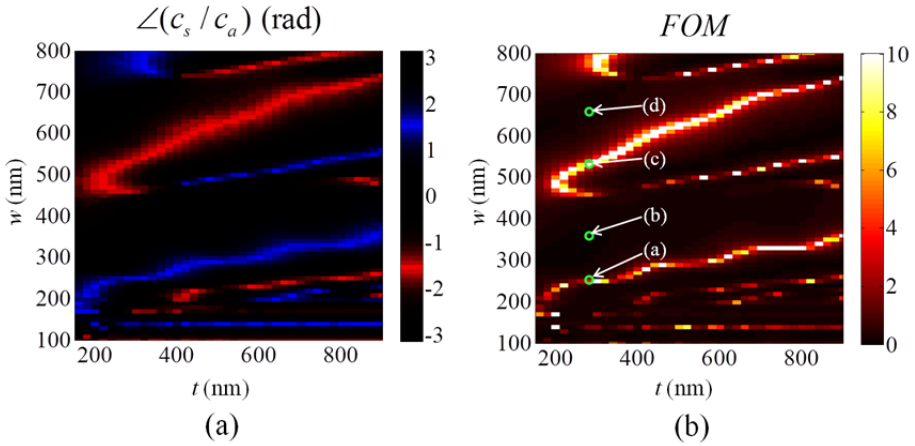

Figure 2.3.4. (a) Phase difference between two types of coupling efficiencies and (b) FOM parameter are shown for various slit-widths and slit thicknesses.

In order to find the slit condition that permits switching the direction of the excited SPP without the amplitude modulation of Beam II, numerically calculated phase difference between c_a and c_s is plotted in Fig. 3.4(a). The slit conditions that satisfy Eq. (2.3.3) are shown in red ($\angle(c_s/c_a) = -\pi/2$) and blue ($\angle(c_s/c_a) = +\pi/2$) regions in Fig. 2.3.4(a). It is shown that the blue or red regions which satisfy the Eq. (2.3.3) are moved to a wider slit width condition when the slit thickness becomes thicker. Such aspect can be explained by the change of effective refractive index difference between symmetric and anti-symmetric MIM modes existing in nanoslit. As discussed in section 2.2, the effective refractive index difference between these two modes becomes smaller when the slit width becomes wider. Therefore, a longer slit thickness is required to achieve the same amount of phase difference between those two types of SPP excitations. For the SPPs excitation problem, one of the most important issues is the efficiency of power coupling from plane wave source to SPPs. Moreover, in our configuration, unidirectional ratio which denotes the deference between left and right side excitation is also important. Therefore, it will be better to define a figure of merit (FOM) parameter of the proposed structure which is expressed as,

$$FOM = \left| \frac{\min(c_s, c_a)}{|U_R| - |U_L|} \right|. \tag{2.3.5}$$

In Eq. (2.3.5), a smaller value of the denominator increases the maximum unidirectional ratio during the phase modulation of Beam II, whereas a larger value of the nominator increases the absolute amount of coupled SPPs. Therefore, it can easily express the performance of the proposed plasmonic unidirectional launcher both in its absolute coupling efficiency and left-to-right amplitude ratio. In Fig. 2.3.4(b), FOM values for various slit conditions are plotted. It is obvious that the high FOM values are directly found in the red or blue regions in Fig. 2.3.4(a), which correspond to the phase differences of $\angle(c_s / c_a) = \pm\pi/2$.

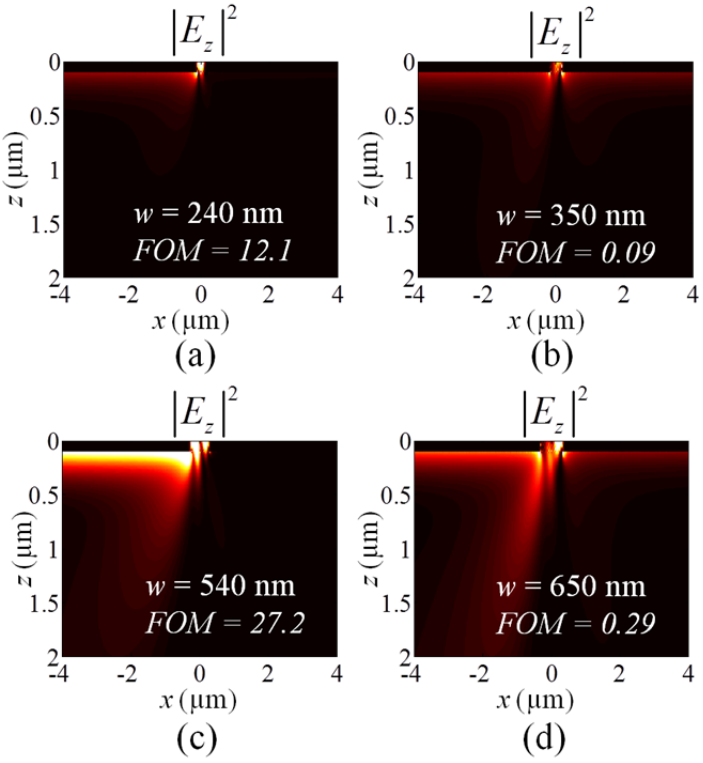

Figure 2.3.5. Intensity profiles at the transmitted side of the slit are shown for different slit width conditions at t = 300 nm : (a) w=240 nm, (a) w=350 nm, (a) w=540 nm, and (a) w=650 nm. Each figure shows the state of the highest unidirectional ratio (left-side enhanced) value during the phase modulation.

However, it is possible to obtain more information from Fig. 2.3.4(b) than Fig. 2.3.4(a). Along the conditions where the thickness of metal slit is t = 300 nm, it is shown that more than two colored points are exist in Fig. 2.3.4(a). For example, two conditions w = 250 nm and w = 540 nm

are both in the colored region of Fig. 2.3.4(a). However, it is not easy to figure out which condition is better from this figure. On the other hand, the FOM value of each condition is quite different. To figure out that, the relations between the efficiency of unidirectional ratio ($\Gamma = |E_L / E_R|^2$) and the FOM value are shown in Fig. 2.3.5 by illustrating the intensity of the transmitted SPPs for each slit condition marked in Fig. 2.3.4(b). Since the unidirectional ratio changes when the phase difference between Beam I and Beam II is varied, each of the images shows the state of the highest unidirectional ratio value during phase modulation. From Figs. 2.3.5(b) and 2.3.5(d), it is clear that unidirectional launching does not occur by phase modulation when the conditions of Eq. (2.3.3) is not satisfied. Moreover, by comparing Figs. 2.3.5(a) and 2.3.5(c), it is also found that the absolute amount of transmitted light is increased when FOM has a higher value, even though both conditions of Figs. 2.3.5(a) and 2.3.5(c) satisfy the phase difference condition. Therefore, it is clarified that condition of w = 540 nm is much better than that of w = 250 nm at t = 300 nm condition, by observing the FOM parameter.

2.3.3. Experimental demonstration for phase-modulated plasmonic switching

2.3.3.1. Experimental configuration

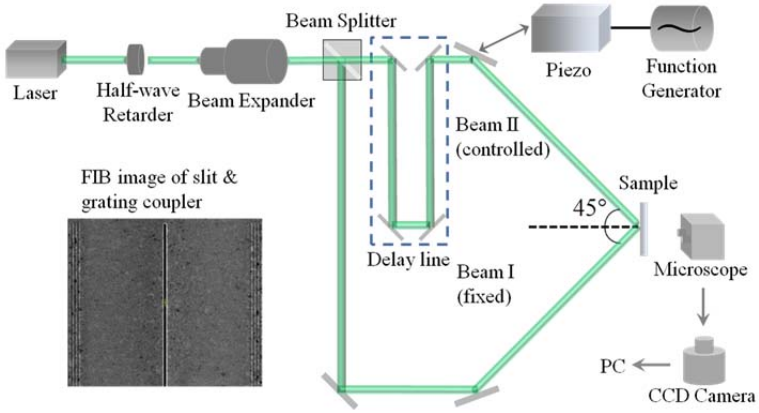

Figure 2.3.6. Experimental setup used for detecting the phase-controlled switchable unidirectional launching of SPP. Inset (left-bottom) shows the FIB image of fabricated slit and grating coupler.

In Fig. 2.3.6, experimental configuration for demonstrating the proposed SPP switching mechanism is shown. As discussed in theory part, this switching method uses two incident beams which have different phase conditions. A 532 nm green laser source passes through the beam splitter to split single source into two beams. Before it passes the beam splitter, half-wave retarder is used to set the polarization state of incident beams to TM polarization, and beam expander is also used to confirm the incident beam as a plane wave source. One of the separated beams directly illuminated to the backside of sample, which becomes a fixed-phase beam. On the other hand, the other beam is reflected by a shifting mirror which is electrically driven by a piezo-stage. Here, the *z*-stage of piezo-stage is controlled, which is a direction normal to the mirror surface. Since the optical path length of controlled beam is slightly changed by the movement of the mirror, the overall incident phase of controlled beam is changed when it reaches the nanoslit carved on the sample. In the left-side inset of Fig. 2.3.6, the shape of the carved slit is shown. As shown in the image, the center slit is carved with the thickness of w = 540 nm, which is an optimized condition for 300 nm thickness silver film. The vertical length of the slit is 25 μm, which is far longer than the width of the slit. Therefore, the side-effect caused by the finite vertical length of the slit can be suppressed. The output couplers are also carved at the left- and right-side of the center slit. The distance between the center slit and output couplers is 10 μm. The depth of the output couplers are set to 40 nm, however, this value is not so accurate due to the non-uniform milling process of FIB machine.

2.3.3.2. Calibration and experimental results

For the measurement of surface plasmons generated from the nanoslit, far field images above the slit and output couplers are captured by CCD and analyzed. Before investigating the switching performance, calibration of piezo-stage is done by applying electric voltage generated by function generator. Since it is not possible to exactly know how much the piezo-mirror is moving according to the input voltage, it is necessary to find appropriate voltage condition of 2π-change for the control beam at first. To find that condition, square pulses which have the frequency of 1 Hz is used. When the applied voltage corresponds to the phase difference change of $2n\pi$, where n is a natural number, there will be no difference in CCD image even though the applied voltage is changed.

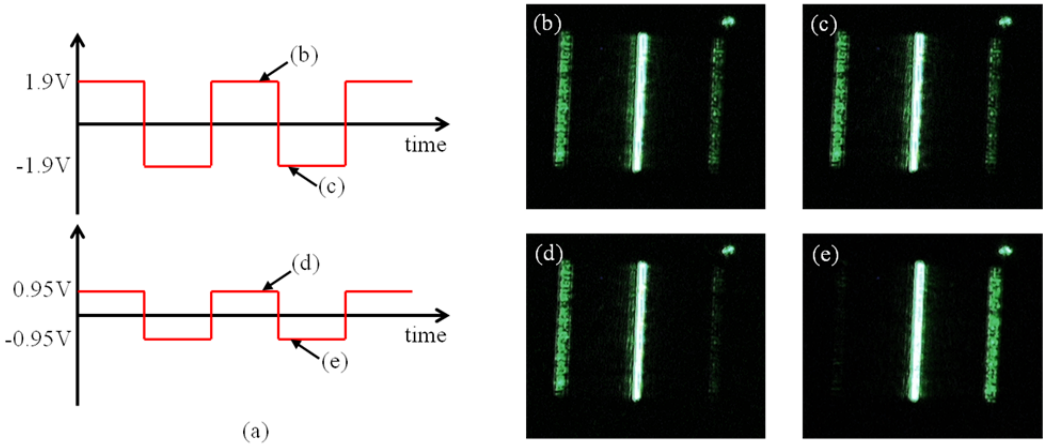

Figure 2.3.7. (a) Input square pulse signal applied to piezo-stage. CCD images when the applied voltage difference makes 2π-phase change of control beam ((b) plus and (c) minus 1.9V). CCD images when the applied voltage difference makes π-phase change of control beam ((d) plus and (e) minus 0.95V).

In Fig. 2.3.7(a), the shape of applied voltage to piezo-stage is shown, and relative CCD images are depicted from Figs. 2.3.7(b) to 2.3.7(e). When the applied voltage is a square pulses which have the amplitude of -1.9V to 1.9V, the change of field is not observed during the abrupt change of incident voltage, as shown in Figs 2.3.7(b) and 2.3.7(c). On the other hand, when the half of the voltage is applied (-0.95V to 0.95V), the direction of propagating SPP is clearly switched as shown in Figs 2.3.7(d) and 2.3.7(e). From these results, it is possible to find that the condition of applied voltage to make a $2n\pi$-change of control beam is 3.8V. However, the value of n can be any odd number.

To confirm that the voltage difference of 3.8V is exactly generating 2π-change to control beam, another shape of voltage signal is used. A linearly increasing sawtooth-shaped signal is used instead of square pulse with 0.2 Hz. By using this type of signal it is possible not only to confirm the calibration process but also to figure out the response of our switching mechanism with the linear change of incident phase by assuming that the piezo-stage is linearly operating according to the applied voltage in designed range.

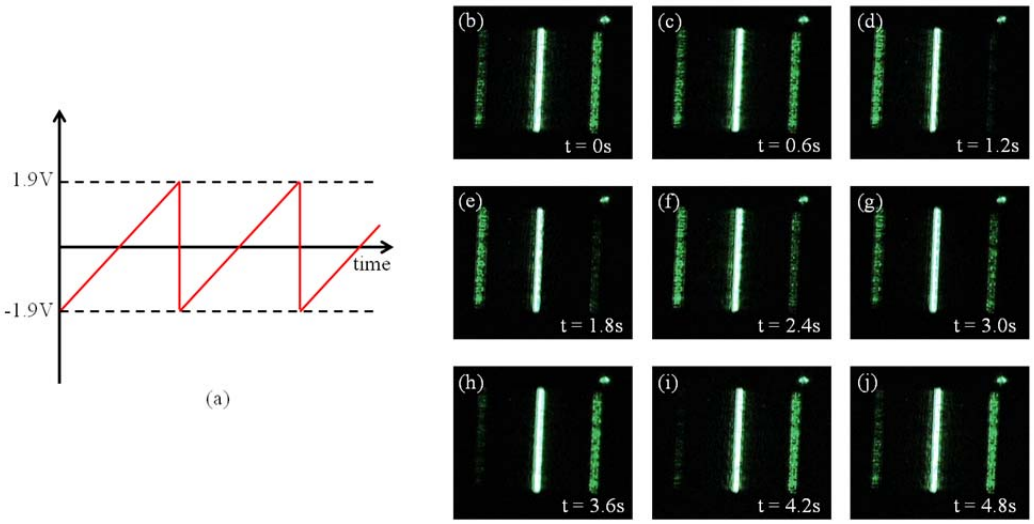

Figure 2.3.8. (a) Input sawtooth pulse signal applied to piezo-stage. Captured CCD images with time steps when the applied voltage changes from -1.9V to 1.9V with frequency of 0.2 Hz. (From (b) to (j), time is changed from 0s to 4.8s with 0.6s step.)

In Fig. 2.3.8(a), the shape of applied voltage to piezo-stage is shown for sawtooth case. Moreover, CCD images at the different conditions of input voltages are depicted in the other figures of Fig. 2.3.8. Note that the periodical change of launching direction of SPP occurs only once for one cycle of sawtooth wave. This means the amount of phase change during the 3.8V difference is exactly 2π-change. Moreover, it also means that it is possible to observe full cases of phase difference between Beam I and Beam II within the one period of this sawtooth wave. Therefore, it is possible to assume that the voltage sweep from -1.9V to 1.9V can express the cases of phase difference between two beams from 0 to 2π. Here, the unidirectional ratio is defined as,

$$\Gamma = \left| E_L / E_R \right|^2 . \tag{2.3.6}$$

For the experimental results, E_L and E_R are extracted from the integration of pixel data of CCD on the region of each output couplers. For the numerical results, E_L and E_R are defined to the z-directional electric field amplitude calculated by RCWA at 4 μm away from the center slit and 5 nm above the surface of metal layer. The experimental results are measured for several times of

periods and depicted in Fig. 2.3.9 as a shape of error bars, whereas numerical results are shown in the blue solid line.

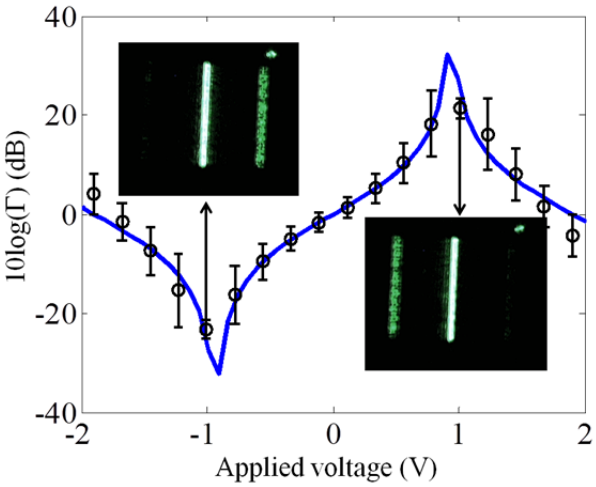

Figure 2.3.9. Comparison between experimentally measured unidirectional ratio (error bar) and numerical results (solid line) is shown. Insets show captured CCD images for the conditions of the pointing markers.

Chapter 3

Plasmonic devices by using the directional launching of SPPs

Throughout the Chapter 2, the methods for exciting SPPs unidirectionally from the end of nanoslit are discussed, which are coupled from the MIM plasmonic modes inside the nanoslit to single interface SPPs at the transmission side of the metal surface. Two different methods that based on polarization and phase modulations are introduced in each subsection, respectively.

In this Chapter, methods discussed in previous chapter are expanded to be applied in various types of plasmonic devices. In section 3.1, the principle used in Chapter 2 is used to MIM plasmonic modes in order to make a plasmonic dichroic splitter. In Section 3.2, polarization-dependent excitation of SPPs is now expanded from one-dimensional slit to two-dimensional circular-hole structure. In this case, polarization-switchable beaming is demonstrated by applying the chiral structure which is called double spiral bull's eye geometry.

3.1. Plasmonic dichroic splitting with nanoslit coupler on MIM waveguide

Over the few decades, detecting and sorting photons according to their energy level has been necessary not only for spectrum analyzing of optical antennas but also for designing optical sensors and photovoltaic devices. Demands for utilizing light as a quantized particle for understanding interaction between nano-scaled structure and photons strongly request ultra-compact photon detector that can be easily manipulated by external interactions. Particularly, optical detecting and analyzing within a sub-wavelength scale structure has been a fascinating issue.

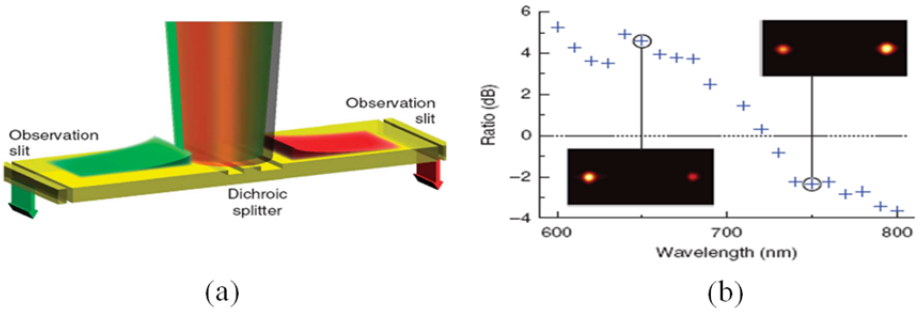

Figure 3.1.1. (a) Configuration of the previously reported plasmonic dichroic splitter and (b) its performance [56].

Recently, a sub-micron sized plasmonic dichroic splitter has been demonstrated by using the double groove structure which has an asymmetric width of the groove [56]. In Fig. 3.1.1, schematic diagram of the previously proposed plasmonic dichroic structure is shown. They achieved dichroic splitting of SPPs by using the different coupling characteristics of each groove with respect to the groove-width. Although their demonstration was quite successful, it has some limitations since the guiding directions of dichroic splitter are fixed due to asymmetry and splitting ratio was not so good. Especially, the work has been done in near infrared region, so with our best knowledge, there has been no sub-micron size plasmonic dichroic splitter operated in visible range which can switch the guiding direction according to the incident polarization state.

In this section, polarization-sensitive modulation of SPPs which is demonstrated in Section 2.2 is applied to MIM plasmonic waveguides parallel to the metal substrates. In that case, strong

lateral Fabry-Perot (FP) resonance appears between the edges of nanoslit due to the cavity formed by the entrance slit and the bottom metal substrate of MIM layer. Such lateral FP resonance can abruptly change the incident phase condition coupling to the MIM waveguide near the resonance condition, and such abrupt changes are generated at the totally different condition in TE and TM polarization cases.

As a result, by appropriately designing the geometrical parameters of the proposed structure, it is possible to split the two different incident wavelengths into opposite direction of MIM waveguide. The principle of proposed plasmonic dichroic splitter is quite simple, which is setting the FP resonance condition of the proposed structure between the designed two wavelengths.

3.1.1. Principle of dichroic splitting

3.1.1.1. Configuration of the plasmonic dichroic splitter

In Chapter 2, it is shown that the SPPs can be excited unidirectionally at specific polarization state due to the interference of anti-symmetrically and symmetrically excited SPPs. One can expect that plasmonic dichroic splitting can be achieved when such cancellation of SPPs for specific side excitation is oppositely done for different input wavelength [56]. To achieve that, strong sensitivity on the input wavelength is needed. However, it is hard to expect that such strong wavelength dependency is generated from simple single nanoslit structure.

Therefore, other types of SPP coupling structure are needed for realizing plasmonic dichroic splitter. To solve that problem, the single-layered metal film is replaced into three-layered metal-dielectric-metal structure, which is shown in Fig. 3.1.2. Here, the incident light is obliquely provided in *y*-*z* plane similar to the configuration of Chapter 2. As revealed in Chapter 2, excited SPPs from nanoslit should have anti-symmetric profile for TE polarization and symmetric profile for TM polarization incidence for given configuration due to the charge symmetry.

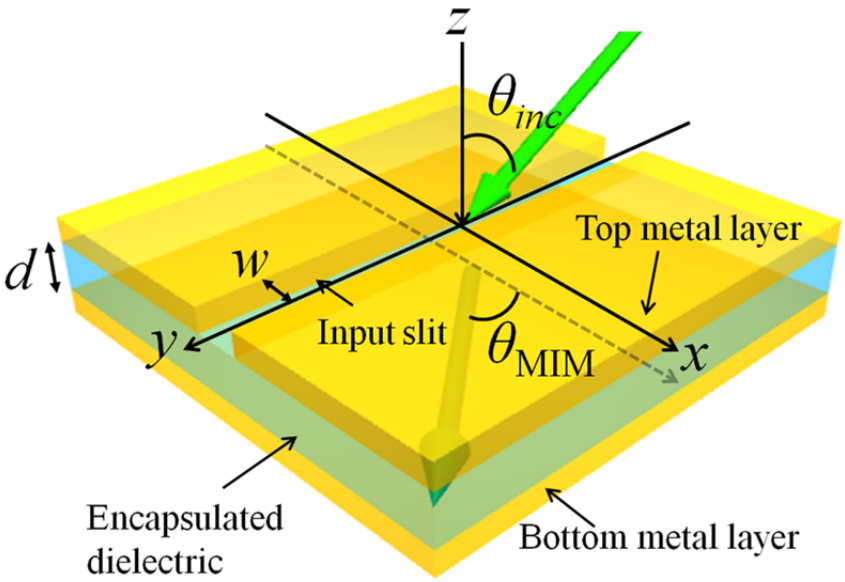

Figure 3.1.2. Configuration of the slit-coupling through the metal-dielectric-metal waveguide layer, which will be used for compact plasmonic dichroic splitter.

These characteristics are maintained even though the single-layered structure is changed to MIM layer, which is illustrated in Fig. 3.1.2. Since the infinite length of the input slit is assumed, *y*-directional momentum is conserved. Therefore, the propagating direction of MIM mode inside the encapsulated dielectric layer has the angle θ_{MIM} with respect to the *x*-axis, which can be expressed as,

$$\theta_{MIM} = \sin^{-1}\left(\frac{n_{air}}{n_{MIM}}\sin\theta_{inc}\right). \tag{3.1.1}$$

For the realization of plasmonic dichroic splitter, following conditions should be satisfied. Firstly, the amplitude of generated SPPs caused by TE polarization state, which has anti-symmetrical phase distribution (Fig. 3.1.3(a)) and that caused by TM polarization state, which has symmetrical phase distribution (Fig. 3.1.3(b)), should be in similar amplitude scale both in two designed wavelengths.

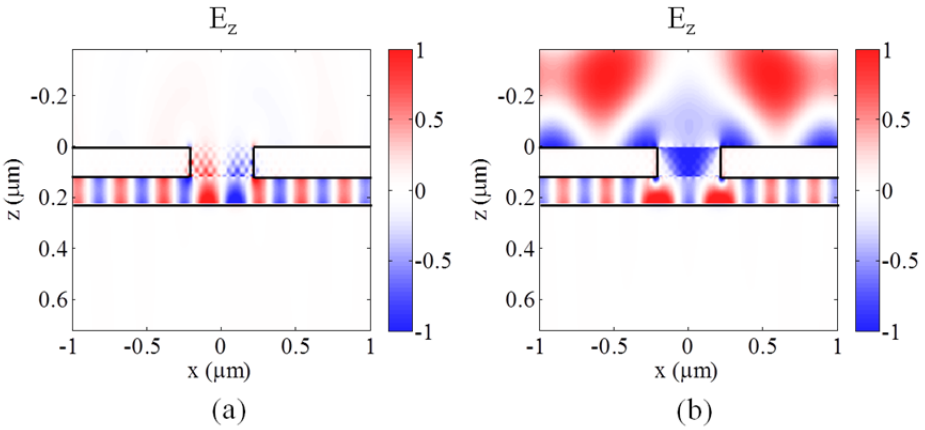

Figure 3.1.3. E_z field distribution along the *x*-z plane when the light is obliquely incident through *y*-z plane on the structure shown in Fig. 3.1.1 with (a) TE and (b) TM polarization state. The width of slit, thickness of encapsulated dielectric, and incident wavelength are set to 300 nm, 100 nm, and 532 nm, respectively.

This condition is necessary in order to make a perfect destructive interference on single side of MIM waveguide which will result in the unidirectional launching. Next, the relative phase difference between SPPs excited from TE and TM waves at one designed wavelength should have nearly π-phase difference compared to that of the other designed wavelength. This condition makes unidirectional launching of SPPs of each designed wavelength be achieved simultaneously, but with opposite directions at the same incident polarization state. Finally, one can expect the abovementioned two conditions should not be too sensitive to the geometrical parameters in order to prevent the degradation of performance caused by imperfection of fabrication process.

3.1.1.2. Fabry-Perot resonance at input coupler

As discussed in previous section, the key parameter for dichroic splitting is achieving an abrupt change of coupling phase from input plane wave source to MIM plasmonic mode between two designed wavelengths. In this section, the reason for choosing a complicate MIM waveguide geometry instead of single-layered metal film is explained. In Fig. 3.1.4, brief schematics are illustrated to show the difference of optical response between the single-layered structure used in chapter 2 and three-layered MIM structure of this chapter. When the light illuminates the nanoslit patterned on single metal film as depicted in Fig. 3.1.4(a), some portion of incident field after

passing through the nanoslit will be coupled to the SPPs mode which propagates along the transmitted side of metal surface. It is known that the amount of coupled SPPs is affected by the width of the slit. Weak periodical fluctuation of coupling efficiency was observed due to the momentum matching conditions of diffracted light [57, 58]. According to the explanation in Ref. [57], angular spectrum of diffracted wave nearly follows the Fourier transform of the geometry of the aperture. In the case of simple slit, it will follow the sinc function.

Therefore, evanescent components of diffracted light which are matched to the wavevector of SPPs are also periodically changed. However, such changes are too weak to generate an abrupt phase change since it is not based on the resonance effects.

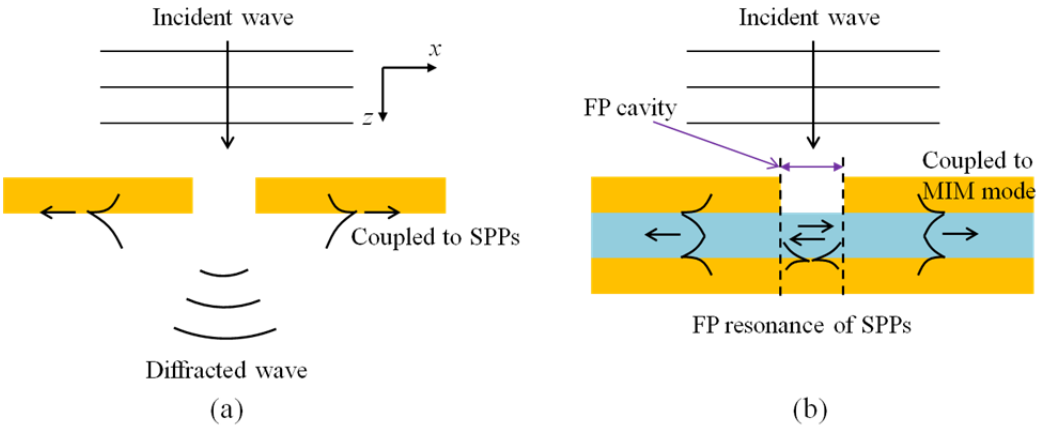

Figure 3.1.4. Schematic diagram to compare the aspect of diffracted and guided light from the nanoslit carved on (a) single metal layer and (b) metal-dielectric-metal three layers.

On the other hand, let me consider the case incidence to the three-layered MIM waveguide structure as shown in Fig. 3.1.4(b). When the depth of the encapsulated dielectric (d) is sufficiently thinner than the incident wavelength, it is quite hard to directly couple from incident plane wave to MIM plasmonic mode by simple diffraction at the edges of input slit. Otherwise, most of coupling to MIM plasmonic mode is caused by the FP resonance at the two-dimensional cavity structure formed by the input slit and bottom metal layer. Incident light firstly diffracted at the input slit, and some portion of them will couple to the metal-dielectric-air hybrid plasmonic mode which will propagate inside the cavity. Then hybrid mode is coupled to the MIM plasmonic mode. Therefore, the amount of coupled light to MIM plasmonic mode is significantly sensitive to

the width of the slit, which determines the FP resonance condition. Since the amount of coupled light is proportional to the electric field amplitude at the ends of cavity, shape of standing wave inside the cavity caused by FP resonance is the most important factor to increase the coupling efficiency. When the FP resonance condition is satisfied, the nodes of the standing wave are located at the ends of cavity. Therefore, coupling to the MIM plasmonic mode is strongly prohibited at the condition of FP resonance. Here, the FP resonance condition can be obtained as follows,

$$w/\lambda_{SPP,x} = m/2 \quad (m = 1,2,3,...) . \tag{3.1.2}$$

where w is the width of slit, m is an integer number, and $\lambda_{SPP,x}$ is an x-directional effective wavelength of hybrid SPP mode inside the cavity which is given as,

$$\lambda_{SPP,x} = \frac{\lambda_0}{\sqrt{{n_{SPP}}^2 - \sin{\theta_{inc}}^2}} \ , \tag{3.1.3}$$

where n_{SPP} is an effective refractive index of hybrid SPP mode. By substituting (3.1.3) into (3.1.2), relation between slit width and input wavelength can be obtained as,

$$w/\lambda_0 = \frac{m}{2\sqrt{{n_{SPP}}^2 - \sin{\theta_{inc}}^2}} \ , \tag{3.1.4}$$

However, since two orthogonal polarization states (TE and TM) affect the charge and SPP field symmetry, these FP resonances are also appeared differently. FP resonance with odd number of m makes a belly at the center of the cavity, so it should have symmetric field profile. Therefore, FP resonance with odd number of m is only generated by TM incidence, which is known as the case of symmetric surface charge generation. On the other hand, FP resonance with even number of m makes a node at the center of the cavity. For this case, anti-symmetric field profile is formed so that it could be only generated by TE incidence. In Fig. 3.1.5, a schematic diagram for explaining the abovementioned relation of FP resonance and incident polarization is shown for clear understanding.

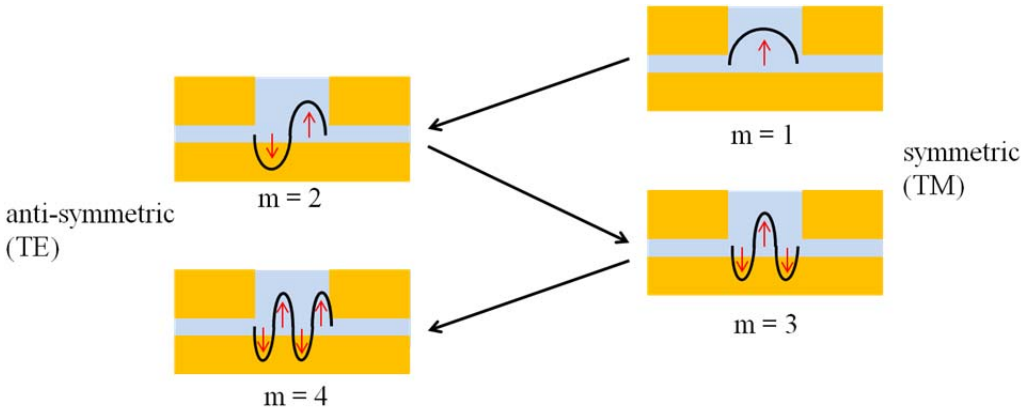

Figure 3.1.5. Schematic diagram to show the appropriate polarization state for generating FP resonance conditions inside the cavity formed by input slit and MIM layer. It shows that the FP resonances with odd number of standing wave are excited from TM incidence, whereas those with the even number are excited from TE incidence.

3.1.2. Numerical results of dichroic splitter

3.1.2.1. Coupling efficiency for TE and TM illuminations

In previous section, the main principle of dichroic splitter and the reason for choosing three-layered MIM structure instead of single-layer are explained. From now, the geometric parameters that satisfy the conditions for practical use of dichroic splitter will be found. At first, let me set the two designed wavelengths to be split are 532 nm and 660 nm, which are the green and red light in visible range. By setting the wavelengths like these, it will be quite easy to visually compare the performance of dichroic splitter. Moreover, the incident angle is fixed to $\theta_{inc} = 45°$; this value of incident angle can generate nearly the same amount of SPP mode for both TE and TM polarization states as I have shown in Chapter 2. Due to the limitation on experimental fabrication, refractive index of encapsulated dielectric is set to $n = 1.49$, which is a refractive index of polymer material that will be used in experiment part. Other parameters such as slit width (w), thickness of the top metal layer, and thickness of encapsulated dielectric are tuned to find an appropriate condition for plasmonic dichroic splitting.

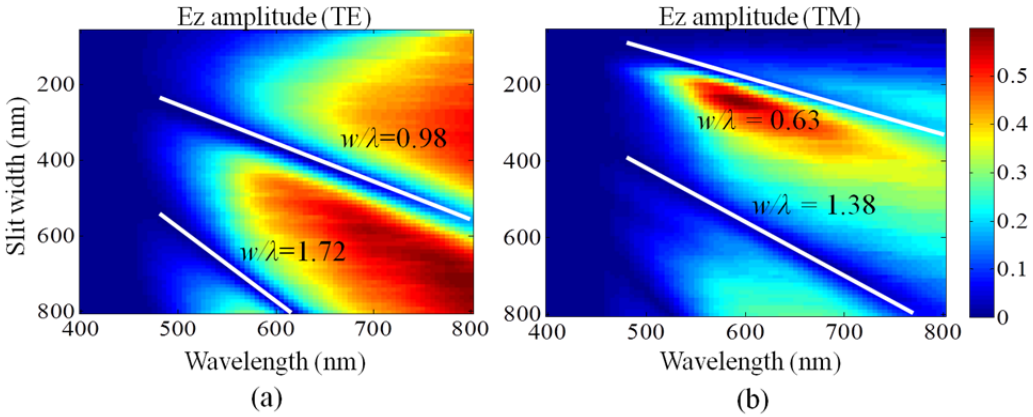

Figure 3.1.6. The parameter sweeping results of field amplitude coupled to MIM plasmonic mode for (a) TE and (b) TM illumination. White lines show the conditions for low coupling ratio caused by the FP resonance.

In Figs. 3.1.6(a) and (b), the amplitudes of coupled MIM plasmonic mode for TE and TM incidence are shown varying with the input wavelength and the width of slit, respectively. They show the *z*-directional electric field at 4 μm left-away from the center of slit at the middle point of encapsulated dielectric. Although the measurement is done for left side, fields coupled to left and right side have equal amplitude in TE or TM illumination due to the field symmetry so that the coupling to right-side MIM waveguide has the same value. As mentioned in Section 3.1.1, the blue lines, which mean the blocking of MIM mode coupling, are clearly shown in both figures. However, the locations of blue lines are quite different, and they do not cross each other.

To show these abrupt decreases of coupling efficiency originate from the FP resonance, the gradients of blue lines which are depicted in the figures are compared to that of analytic condition of FP resonance. Those values are 0.63, 0.98, 1.38, 1.72 for each blue line from upper of Fig. 3.1.6(b) to lower of Fig 3.1.6(a). Note that the location of lines reputably moves from TM to TE, which is exactly same as the schematic shown in Fig. 3.1.5. Moreover, the differences of gradient between each nearby line have almost similar values, which are 0.35, 0.4, and 0.34. This value also coincides with the calculation based on Eq. (3.1.3) by substituting $n_{SPP} = 1.6$ (average value of hybrid mode between 532 nm and 660 nm), which is obtained as $w/\lambda_0 = 0.35m$. Although there is an offset for the gradient of the first FP condition, this is natural since the phase change during the reflection at the FP cavity cannot be considered in theoretical data. Nevertheless, the

differences of gradients between nearby FP resonance conditions are significantly well-matched to the theoretical prediction.

3.1.2.2. Optimization of the condition for dichroic splitter

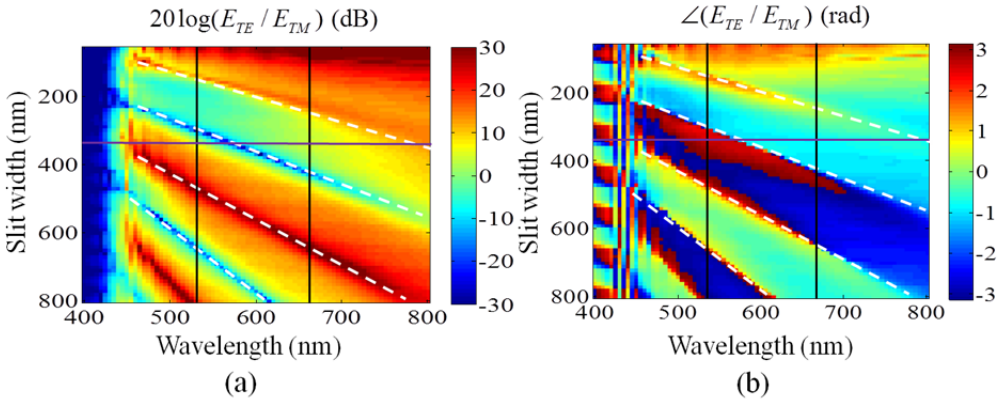

Figure 3.1.7. (a) Amplitude ratio and (b) phase difference between coupled SPPs caused by TE and TM polarization incidence are shown for various slit width and slit thickness conditions. White lines show the same FP conditions which are also shown in Fig. 3.1.6.

Until now, it is shown that the FP resonance inside the input cavity can block the coupling from incident wave to MIM plasmonic wave. For the next step, aspect of amplitude ratio and phase difference between coupled MIM plasmonic modes from TE and TM incidence are investigated in Fig. 3.1.7. The white dotted lines are FP resonance conditions which are also shown in Fig. 3.1.6, both resonances of TE and TM incidences are shown simultaneously. Since the coupled SPPs from TE or TM resonance are blocked by the FP resonance, it is natural that the amplitude ratio (E_{TE}/E_{TM}) has dips for the FP resonance condition of TE incidence, whereas it has peaks for that of TM incidence as shown in Fig. 3.1.7(a). Moreover, one of the interesting points is the abrupt phase change at the FP resonance conditions, which is shown in Fig. 3.1.7(b). The figure shows the phase difference between the excited MIM plasmonic modes caused by TE and TM incidence cases. Note that this phase difference is measured at the 4 μm left-side of the input slit; it will have π-phase difference respect to these values at the right-side of the slit due to the anti-symmetric and symmetric phase profiles of excited SPPs from TE and TM polarization incidence.

However, it does not affect the overall aspect of phase difference since it only gives constant π-phase difference. Significant phase changes at the FP resonance conditions are clearly observed, whereas it has almost flat values within the region between two FP resonance conditions. Although the important phenomena exist at the FP resonance condition, the geometrical conditions which can satisfy the proposed structure to act as a dichroic splitter are not laid on the FP resonance, but in the region between two FP resonance conditions. In these regions, amplitude ratio does not have peaks or dips so it provides almost similar coupling efficiency both from TE and TM incident waves. Moreover, phase differences have flat values near the one specific wavelength, and perhaps it can have significantly different value at the other designed wavelength if one of the FP resonance lines passes through those two wavelength conditions. The best condition for ideal dichroic splitter is the amplitude ratio of 1 (0 dB) for both 532 nm and 660 nm condition, and the difference between phase differences at the 532 nm and that of 660 nm is π (rad). Although it is not easy to find abovementioned condition simultaneously, one of the best conditions can be obtained at the slit width of 330 nm, which is marked by horizontal purple line in Fig. 3.1.7. The vertical black lines show two designed wavelengths, which are 532 nm and 660 nm, respectively. At the crossing points of those lines, the amplitude ratio is almost in 0 dB, and phase differences are in the flat regions. FP resonance line for m = 2 lies between two designed wavelengths, therefore all of the conditions for dichroic splitting are satisfied at the crossing points.

For the further optimization process, the dependency of amplitude ratio and phase difference with respect to the thickness of top metal layer is investigated. Since there are too many parameters to sweep, it will be better to observe the results only at two designed wavelength 532 nm and 660 nm from now. Hence, figures of merit (FOM) parameters for amplitude and phase difference are defined, respectively. Firstly, FOM parameter for amplitude is defined as,

$$F_A = \left\| E_{z,\lambda_1,TE} \right| - \left| E_{z,\lambda_1,TM} \right\| + \left\| E_{z,\lambda_2,TE} \right| - \left| E_{z,\lambda_2,TM} \right\|, \tag{3.1.5}$$

where λ_1 and λ_2 denote two wavelengths to be split (For this dissertation, $\lambda_1 = 532$ nm and $\lambda_2 = 660$ nm). The z-directional electric field is used for the observation of coupled SPP field since it is the strongest field component for SPP mode and the amplitude is not affected by the propagation direction inside the MIM waveguide. The meaning of parameter F_A is the difference between excited SPPs for TE and TM incident cases. Since similar coupling efficiency for TE and TM incidence is better for the unidirectional launching by interference of them, lower value of F_A

will be more appropriate to the dichoric splitter. Next, FOM parameter for phase difference is defined as,

$$F_P = \begin{cases} \Pi & \text{for } 0 < \Pi < \pi \\ 2\pi - \Pi & \text{for } \pi < \Pi < 2\pi \end{cases}, \tag{3.1.6}$$

where $\Pi = \left| \angle(E_{z,\lambda_1,TE} / E_{z,\lambda_1,TM}) - \angle(E_{z,\lambda_1,TE} / E_{z,\lambda_1,TM}) \right|$, and summation or subtraction of 2π is applied if the value of Π is out of range from $0 < \Pi < 2\pi$. This value means how much phase difference is changed for two proposed wavelengths. This value should be near π-phase to perfectly guide the two different wavelengths into opposite sides of MIM waveguide at the same polarization incidence. Since the maximum value of F_P is π, the higher value of F_P is much better condition for dichoric splitting.

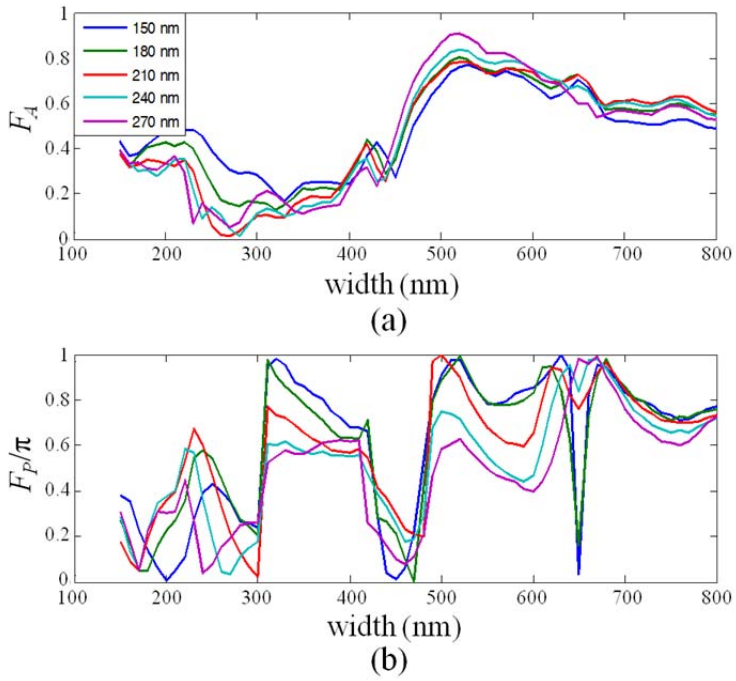

Figure 3.1.8. FOM parameters for (a) amplitude ratio and (b) phase difference which are focused on two operating wavelengths, 532 nm and 660 nm, are shown in order to find better conditions for dichroic splitting.

In Fig. 3.1.8, amplitude and phase FOM values are plotted varying with the top-metal thickness and slit width. Although amplitude FOM has lowest value at w = 270 nm and t = 210 nm, phase FOM does not satisfy the condition. It is shown that near the w = 330 nm and t = 150 nm, we have the best condition for both low F_A and high F_P values. In Fig. 3.1.9, the field distribution at the condition of w = 330 nm and t = 150 nm for (TE, 532 nm), (TM, 532 nm), (TE, 660 nm) and (TM, 660 nm) are illustrated. It can be observed that the amplitudes of coupled SPPs are almost in similar scale for each wavelength. Moreover, although there is slight mismatch, it seems SPPs coupled to right-side MIM waveguide are in-phase for 532 nm by comparing Fig. 3.1.9(a) and 3.1.9(b), whereas they are out of phase for 660 nm. On the other hand, SPPs coupled to left-side MIM waveguide has in-phase profiles as shown in Fig. 3.1.9(c) and 3.1.9(d). Therefore, it will be quite easy to suppose that constructive interference should appear in opposite directions for 532 nm and 660 nm when TE and TM incidences are superposed together.

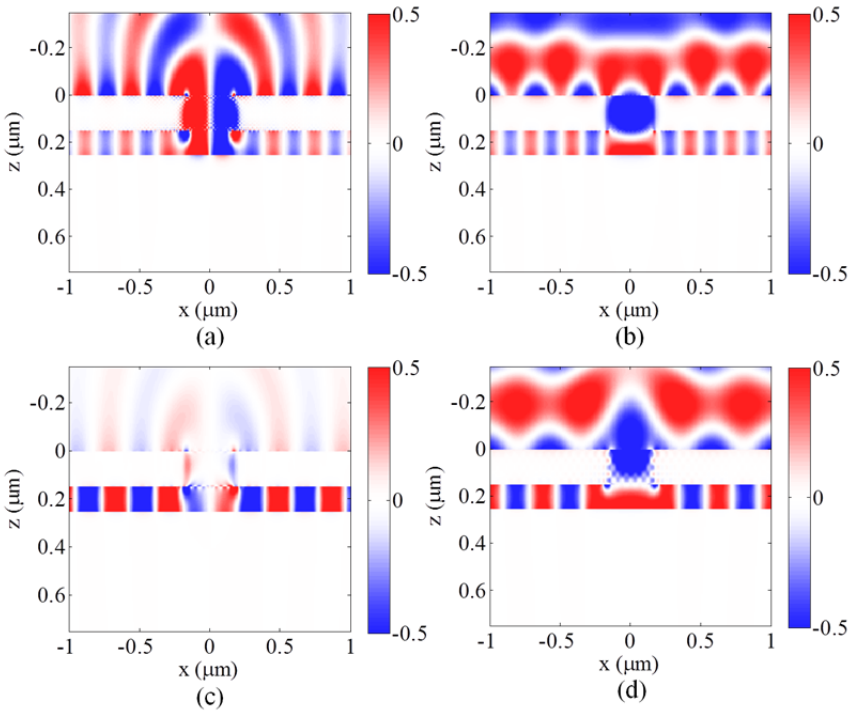

Figure 3.1.9. E_z field profile at optimized slit condition: (a) TE, 532 nm, (b) TM 532 nm, (c) TE, 660 nm, and (d) TM, 660 nm.

In Fig. 3.1.10, electric fields generated by the superposition of TE and TM incidence are shown. Similar to the study discussed on Chapter 2, appropriate amplitude ratio and phase difference between TE and TM polarization components are need to perfectly cancel the SPP excitation to the specific side of waveguide. In this case, incident field of polarization state which has the Jones vector of $(E_{TE},\ E_{TM}) = (1,\ 1.5e^{-j\pi/4})$ is used for perfect destructive interference of right-side MIM mode at 660 nm condition, which is shown in Fig. 3.1.10(b). At the exactly same polarization state, it is shown that the destructive interference appears at the left-side MIM waveguide for 532 nm condition, which means the proposed geometry is well-operated for plasmonic dichroic splitter. Moreover, since the principle of this scheme is based on the plasmonic switching operated by polarization modulation which is discussed in Chapter 2, the direction of MIM coupling can also be changed by the change of polarization state. For example, when the the Jones vector of incident light is changed to $(E_{TE},\ E_{TM}) = (1,\ -1.5e^{-j\pi/4})$, unidirectional launching occurs to left direction for 532 nm, whereas it occurs to right direction for 660 nm condition, respectively.

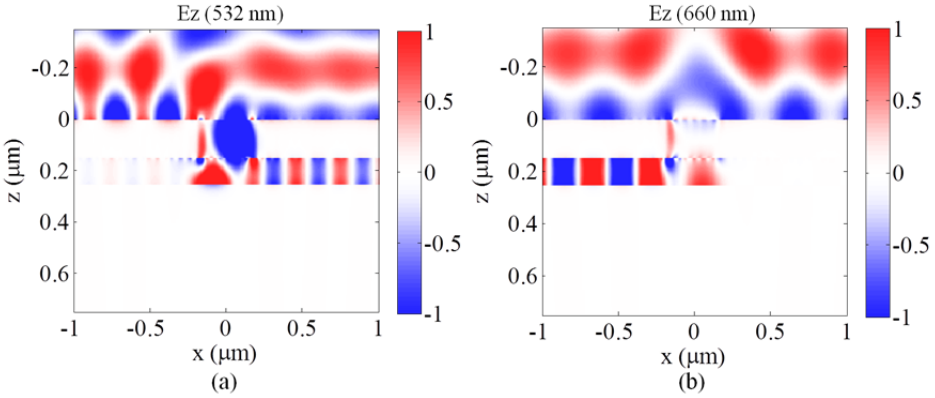

Figure 3.1.10. Field profile of (a) 532 nm and (b) 660 nm cases at the polarization state which can make plasmonic dichroic splitting. Polarization state of $(E_{TE},\ E_{TM}) = (1,\ 1.5e^{-j\pi/4})$ is used for perfect destructive interference on the left (right) side of MIM coupling at 532 (660) nm.

Until now, the detection of coupled SPPs is done by numerical electric field measurement inside the MIM waveguide 4 μm away from the center of input slit. However, such measurement is almost impossible in practical experiment since it is quite difficult to detect the electric field

inside the encapsulated dielectric which is surrounded by metal substrates which are thicker than the skin depth. Therefore, it will need output couplers which can extract the MIM plasmonic mode into the far field radiation.

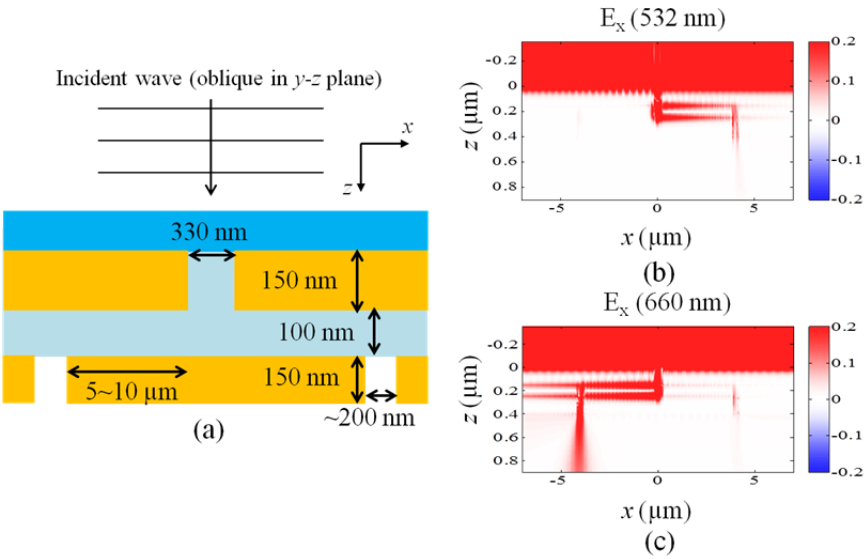

Figure 3.1.11. (a) Full structure of plasmonic dichroic splitter including the output coupler for experimental detection is shown. Numerical simulation results for full structure including output coupler at (b) 532 nm and (c) 660 nm are shown.

Hence, the overall geometry of dichoric splitter which will be demonstrated in experiment looks like the schematic shown in Fig. 3.1.11(a). In this figure, the optimized value of geometrical parameters such as slit width, thickness of each metal layers and encapsulated dielectric, and the length of MIM waveguide between input and output slits are also indicated. The length of MIM waveguide is important for practical experiment since the loss of plasmonic mode in subwavelength-scale MIM waveguide is quite significant in visible range. Therefore, it should be short enough to couple the MIM mode into far field radiation before the vanishing of SPPs by intrinsic loss, whereas it should not be too short to generate large multiple reflections between input and output slits. Considering all of these conditions, Figs. 3.1.11(b) and (c) show the numerical simulation results for plasmonic dichroic splitter. At the same polarization state of incident light, it is shown that each proposed wavelength is coupled to opposite way of plasmonic waveguide, and then out-coupled to the far field radiation below the bottom metal layer. To clearly show the out-coupled far-field radiations, *x*-directional electric field is used instead of *z*-

directional electric field, which has anti-symmetry in fundamental MIM plasmonic mode. Unfortunately, the amount of radiated field is much weaker for 532 nm compared to 660 nm. The reason for weak coupling has two reasons: one is higher loss of MIM plasmonic mode at 532 nm, and the other is weaker coupling efficiency at 532 nm than that of 660 nm, which is already shown in Fig. 3.1.9. In experiment part, handling of this problem is done by using stronger laser source for 532 nm than that of 660 nm, which will be discussed in the next section.

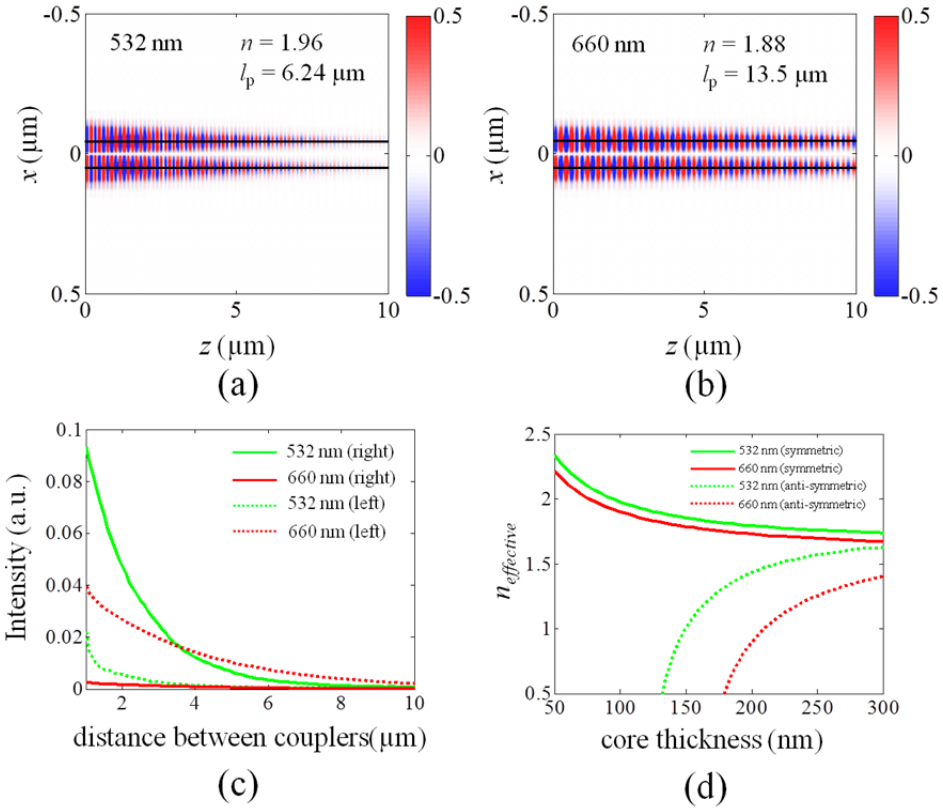

Figure 3.1.12. Propagation of MIM plasmonic mode at the designed condition for (a) 532 nm and (b) 660 nm are shown, respectively. (c) Out-coupled intensities for 532 nm and 660 nm wavelength are shown for left- and right-side output coupler according to the variation of distance between input and output couplers. (d) Mode cutoff conditions of anti-symmetric plasmonic mode are shown for 532 nm and 660 nm, respectively.

In addition, the amount of out-coupled SPPs from the output slit for various distances between input and output slit is also observed. The results are plotted in Fig. 3.1.12, and this will be helpful to design the experimental parameters. At first, the effective refractive index and propagation length of fundamental MIM plasmonic mode at 532 nm and 660 nm are found, respectively. The mode propagations at the designed frequencies are plotted in Fig. 3.1.12(a) and 3.1.12(b). As shown in the figures, the propagation length of MIM plasmonic mode at 532 nm and 660 nm are obtained as 6.24 and 13.5 μm, respectively. Therefore, the distance between input and output couplers should be in the range near these values. In Fig. 3.1.12(c), the amount of out-coupled field amplitude respect to the variation of the distance between input and output couplers is shown at the both sides of output couplers for the unidirectional condition. Here, intensity of incident field for 532 nm case is 2.5 times larger than that of 660 nm case, which is related to the input power difference between two laser sources used in experiment part. With such adjustment, it is shown that output intensities are in the same scale for both incident wavelengths when the distance between input and output couplers is near 4 μm. This value will be applied in experiment part.

In addition, in Fig. 3.1.12(d), the effective refractive index profile of fundamental (symmetric) and secondary (anti-symmetric) MIM plasmonic modes according to the thickness of MIM core region are shown for both 532 nm and 660 nm wavelengths. The cutoff condition of secondary mode for 532 nm and 660 nm lights are observed when core thickness value is 130 nm and 175 nm, respectively. As mentioned previously, designed 100 nm thickness of core can ascertain the cutoff of any higher order modes. Therefore, it is possible to only consider the interference of single mode for the unidirectional launching of SPPs in this region, which is a reason to fabricate the thickness of MIM core layer below the 100 nm.

3.1.3. Experimental demonstration of plasmonic dichroic splitter

3.1.3.1. Fabrication of the plasmonic dichroic splitter

Unlike the simple slit geometry used in Chapter 2, the structure used for plasmonic dichroic splitter is three-layered MIM multilayer structure which needs precise thickness of each layer. Therefore, fabrication methods are much complicate than the structures of previous chapters. In Fig. 3.1.13, flow of the fabrication process is illustrated.

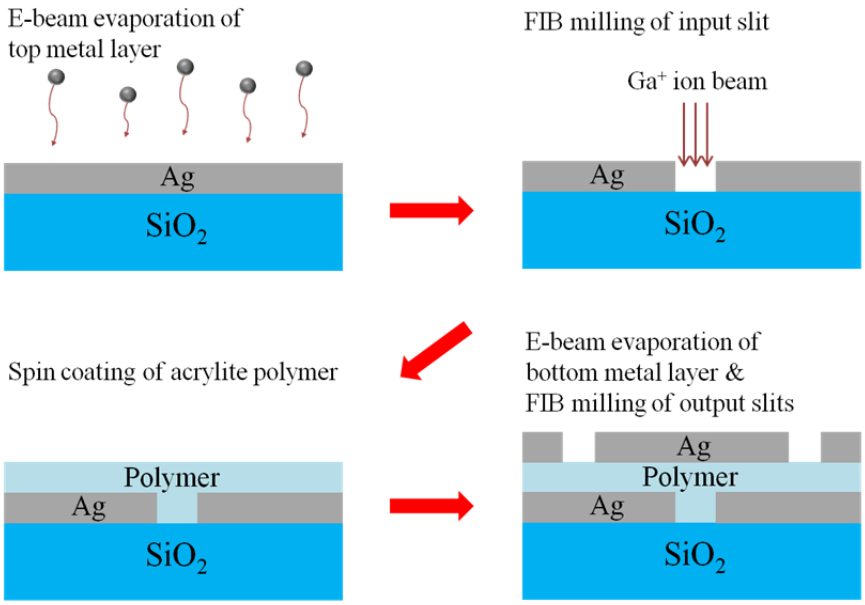

Figure 3.1.13. Schematic diagrams for explaining the flow of fabrication process of the proposed plasmonic dichroic splitter.

Firstly, 150-nm silver layer for top metal layer is evaporated by e-beam evaporator on SiO_2 substrate. The overall sample will be upside down at measurement step so the first layer becomes top metal layer. Then, the input slit is milled by FIB machine, by injecting the Ga ion source into the focused region of the slit. In general, evaporated metal layer is far easy to be milled than rigid SiO_2 substrate. Hence, it is possible to prevent the over-milling of SiO_2 substrate by controlling the milling time appropriately. For the next step, encapsulated dielectric region is deposited by using the spin coater. This step is one of the most important steps for fabrication since the thickness of encapsulated dielectric needs to be controlled to 100 nm. Therefore, the calibration processes is varying with the concentration of acrylate solution which is spin-coated. The condition for spin coating is done for 4000 rpm during 30 seconds. In Fig. 3.1.14, the relation between the concentration of acrylate solution and measured thickness of encapsulated dielectric layers is shown. As plotted in Fig. 3.1.14(a), it is possible to find a linear proportional relation between the concentration of solution and thickness of encapsulated dielectric layer. Moreover, it is also found that the proposed 100 nm thickness of encapsulated dielectric layer is obtained near the 2% of acrylate concentration. Such relations are measured by observing the cross section of MIM waveguide structure without any FIB milling process, which are shown in the Figs.

3.1.14(b), (c), (d), and (e). Therefore, the concentration of acrylate solution is set to 2% for experimental demonstrations.

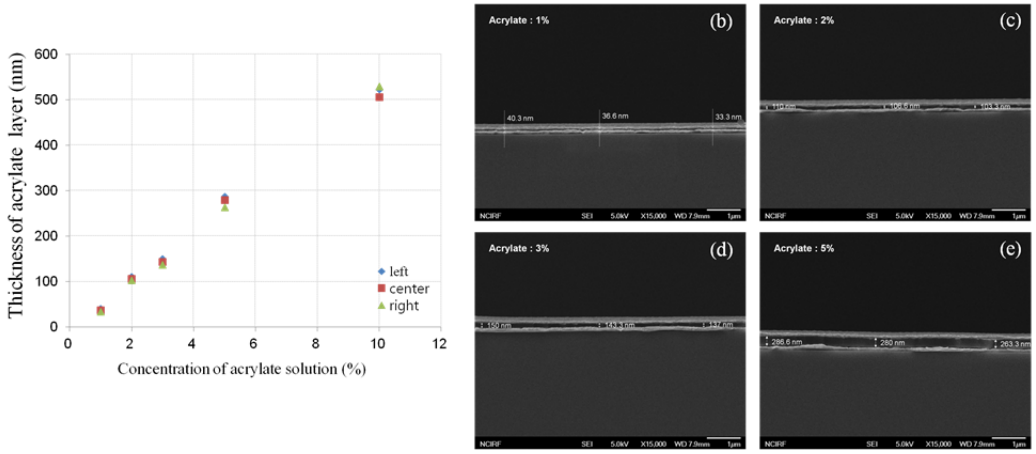

Figure 3.1.14. (a) The relation between the concentration of acrylate solution and measured thickness of encapsulated dielectric layers are shown. SEM images for various thickness of encapsulated dielectric layers: cases for (b) 1% solution, (c) 2% solution, (d) 3% solution, and (e) 5% solution are shown.

After the deposition of encapsulated dielectric, the last process of fabrication is evaporation of bottom metal layer and FIB milling of output slits. One of the problems of this step is how to find the location of input slit that was milled before the evaporation of the bottom metal layer. To solve this problem, relatively large size of markers (tens of micrometers) are also milled by FIB during the process of input slit milling, and there relative location between the markers and input slits are recorded to find the location of input slit. In Fig. 3.1.15, the SEM image of completely fabricated plasmonic dichroic structure is shown. It has been possible to find the location of input slit directly from the SEM image by observing the slightly dark region as shown in Fig. 3.1.15. To measure the aspect of MIM waveguide propagation in our geometry, distances between the input and output slits are fabricated to 4, 7, and 10 μm, respectively. Due to the fabrication limitation of FIB, the output slit is milled non-uniformly. If I tried to perfectly mill the output slit, it is over-carved both on the top and bottom layer. Therefore, output coupler is miledl very slightly on the output metal layer even though the milling process cannot perfectly remove the metal layer of focused region. In Fig. 3.1.15(c), the cross-section view of the proposed structure, which is captured by SEM, is shown to confirm that the structure is well-fabricated. It is clearly shown the

input and output couplers are carved with the proposed slit width, and encapsulated dielectric layer is also shown.

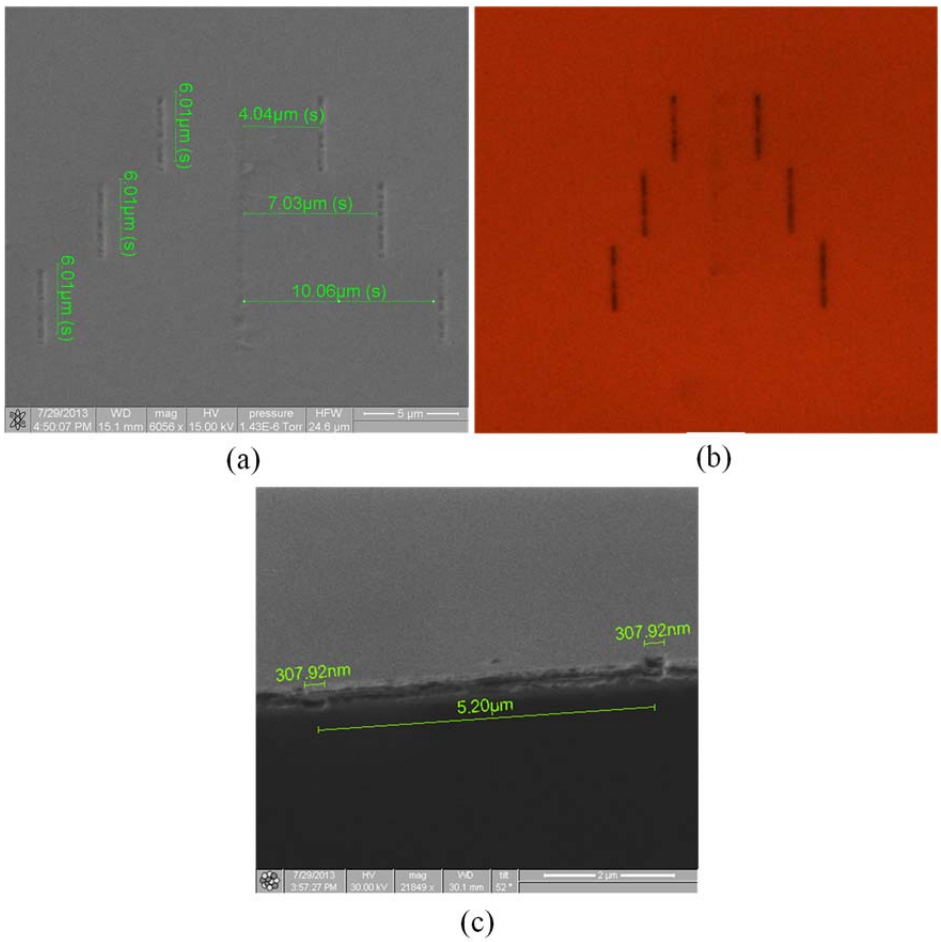

Figure 3.1.15. (a) SEM and (b) CCD image of completely fabricated plasmonic dichroic structure are shown. (c) The cross-section image captured by SEM.

3.1.3.2. Experimental setup and results

For the measurement of plasmonic dichroic splitting, two laser beam sources are simultaneously used as shown in the configuration of Fig. 3.1.16. Both laser sources pass half wave and quarter wave plates which are optimized to their wavelengths in order to control the state of incident polarization carefully. The detection of polarization state is done by the polarimeter module,

which can precisely detect the polarization state within the 0.5 degree of error on Poincaré sphere surface. Since the oblique incidence on the mirrors can change the polarization state, the measurement of polarization is done directly before the illumination on sample.

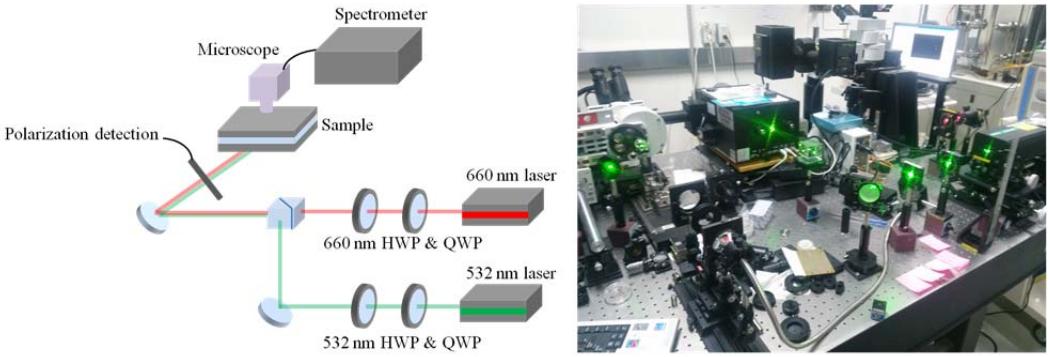

Figure 3.1.16. (a) Schematic diagram and (b) captured image of real experimental setup for the measurement of plasmonic dichroic splitting phenomenon are shown.

The power of red (660 nm) laser source is maximum 200 mW, whereas that of the green (532 nm) source is 500 mW. The difference of laser power can be compensated using the attenuators, but the power of green laser source is set to have much higher value than that of red source due to the lower coupling efficiency and higher metallic loss of MIM waveguide at 532 nm condition, as shown in the difference of brightness in Fig. 3.1.16(b). In Fig. 3.1.17, coupled lights pass that through the MIM waveguide structure are shown for red and green source respectively. From the simulation results performed in previous section, the amplitude ratio of coupled SPPs between TE and TM incidence cases is 3.6 for both wavelengths, and phase differences are -0.8 rad and 2.4 rad for 660 and 532 nm, respectively. For that case, two appropriate polarization states for 660 nm to be launched unidirectionally are obtained in Stokes parameters, $(S1,S2,S3) = (0.85, \mp 0.35, \pm 0.34)$. Since our purpose is splitting two different wavelengths at the same polarization state, these conditions of polarizations are identically applied to the 532 nm source, too. By using the polarimeter, incident polarization state is set to the abovementioned polarization state. Then, out-coupled SPP sources are captured by the CCD camera, which are shown in Fig. 3.1.17. As can be seen, directional launching of SPP source is shown at the purposed polarization state, and it is also found that such directionality is reversed for two designed wavelengths.

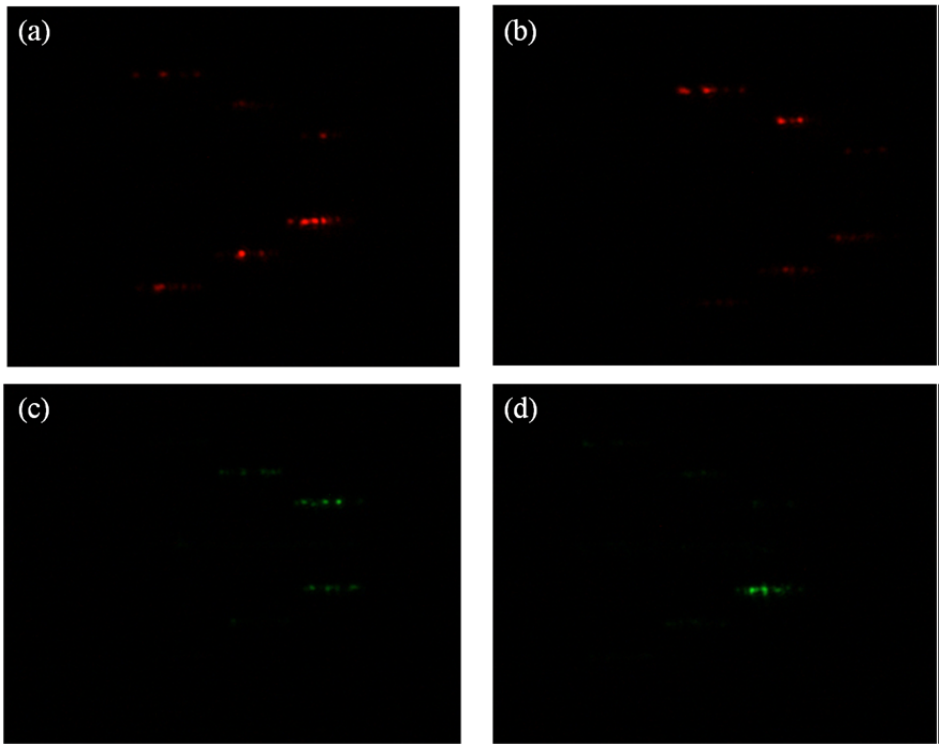

Figure 3.1.17. CCD images of out-coupled source when unidirectional launching occurs to (a) lower-side and (b) upper-side of output coupler at 660 nm. CCD images of out-coupled source when unidirectional launching occurs to (c) upper-side and (d) lower-side of output coupler at 532 nm. The input polarization states of (a) and (c) (or (b) and (d)) are aimed to be identical state.

Finally, Fig. 3.1.18 shows the case when two different wavelengths are simultaneously illuminated. This state is a superposition of Fig. 3.1.17(b) and (d), which clearly shows the demonstration of plasmonic dichroic splitting. Due to the different propagation loss in MIM waveguide, it is shown that the green signal is relatively weaker than the red signal even though the green laser source has much stronger power. Moreover, it is also shown that the green light nearly does not transmit from the farthest output coupler due to the propagation loss.

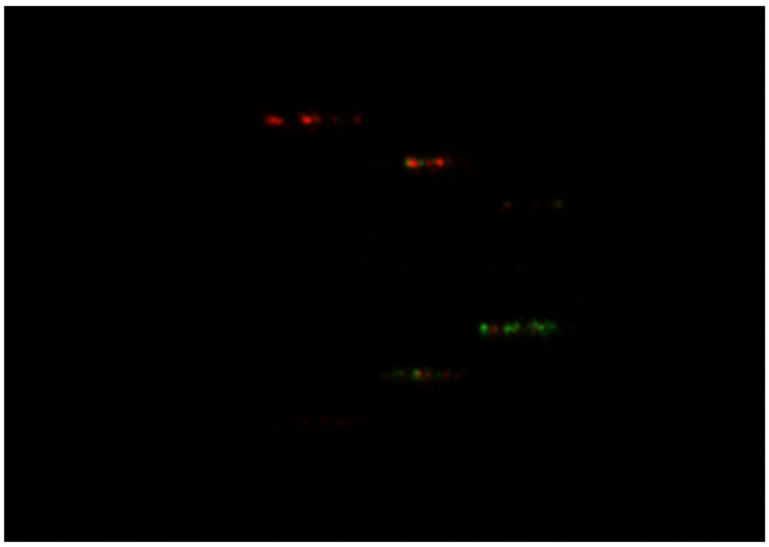

Figure 3.1.18. CCD images of out-coupled source when the input source of Figs. 3.1.16(b) and (d) are simultaneously illuminated. The dicroic splitting of plasmon sources is clearly demonstrated.

3.2. Plasmonic beam switching in double spiral bull's eye

Throughout the previous parts, switching mechanism of propagating SPP source excited from nanoslit structure was investigated. These methods are appropriate to be used for the switchable sources of integrated plasmonic system. However, for the out-coupling of SPPs and their enhancement, beaming from SPPs is also important to generate the nearly subwavelength scale of optical beam [59–61]. The plasmonic beaming, the generation of a highly directional far-field radiating beam by the non-radiating surface plasmon sources, is one of the promising issues for applying the SPPs into several applications beyond the diffraction limit. Plasmonic beaming was firstly demonstrated by using the "bull's eye" structure, which is composed of a small metallic hole surrounded by several periods of concentric annular grating corrugations. Such grating structures can efficiently convert the near-field SPP energy to the far-field radiations, since their periods are designed to compensate the momentum mismatch between the SPP mode and the radiation mode. These plasmonic bull's eye structures have been numerously reported to generate and enhance the three-dimensional optical beam from SPPs source.

In this chapter, improving the conventional plasmonic bull's eye structure to be selectively operated according to incident polarization states is performed. The principle of switchable plasmonic beaming was obtained by applying the double spiral bull's eye geometry instead of concentric one. The chiral geometry of spiral grating structure can change the angular momentum of generated beam during the diffraction at gratings. On- and off-state of the proposed structure are determined by the condition of optical chirality of incident beam. By applying the notation of topological charge number in plasmonic beaming, the aspect of chiral beam generated from the double spiral bull's eye geometry is clearly explained with full numerical electromagnetic simulations.

3.2.1. Principle of beaming from spiral bull's eye structure

3.2.1.1. Spin-orbital interaction in nanohole and plasmonic lens

Before explaining about the bull's eye geometry, the spin-orbital interaction of SPPs from nanohole structure will be briefly explained. The spin-orbital interaction, which is referred in the Ref. [62], means the interaction between the optical chirality of incident light and the orbital angular momentum of transmitted or guided light. Although such phenomenon was firstly reported in transparent bulky material which has both anisotropic and inhomogeneous characteristics [63], it has been intensively researched in plasmonic structure such as nanohole and circularly patterned nanoslit, which is often called plasmonic lens [64]. The reason for such intensive interests of spin-orbital interactions in plasmonic area is that the metallic structure can easily generate such interaction within very short optical path.

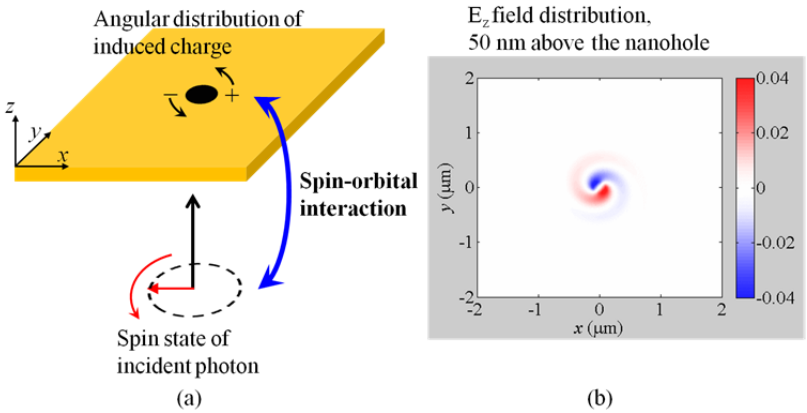

Figure 3.2.1. (a) Schematic diagram for explaining the spin-orbital interaction phenomenon in nanohole geometry. (b) E_z field distribution 50 nm above the nanohole geometry. The radius of nanohole is 50 nm, and incident wavelength of 532 nm is used.

For example, one of the simplest cases of the spin-orbital interaction is shown in Fig. 3.2.1, which is a circular nanohole structure illuminated by circularly polarized light. The rotation of electric field vector makes surface charge near the nanohole rotate; therefore generated SPPs from the nanoslit can have the angular orbital momentum with the same direction of optical polarization as shown in the field distribution of Fig. 3.2.1(b). Moreover, another case of spin-orbital interaction in plasmonic vortex lens is shown in Fig. 3.2.2, can be seen in ref. [28]. In this case, excited SPPs from circularly patterned slits are focused to the center of the structure and generate the plasmonic vortex.

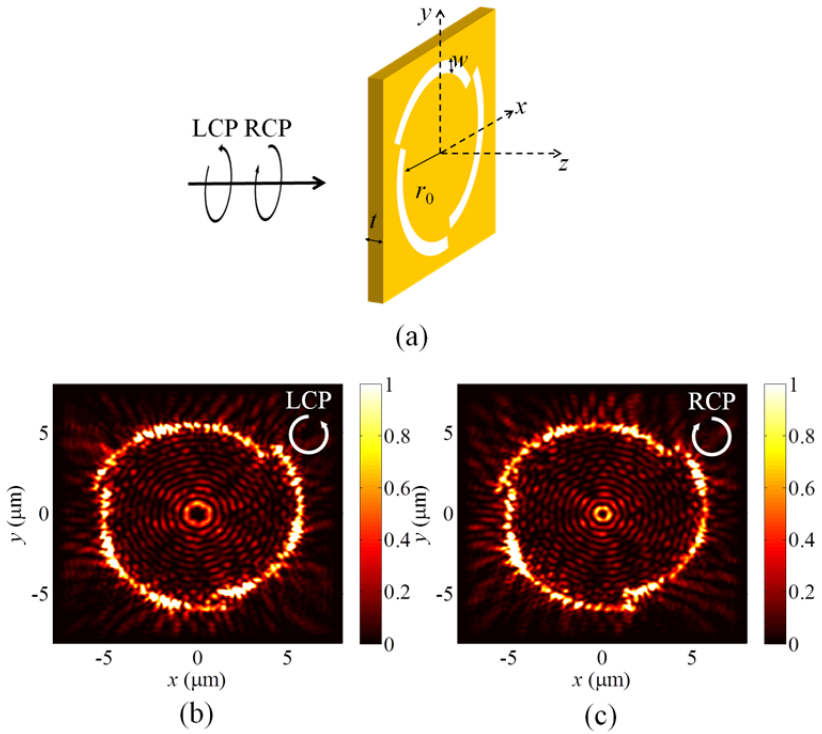

Figure 3.2.2. (a) Schematic diagram of three-fold plasmonic vortex lens structure. Field intensity distributions of plasmonic vortex generated from three-fold plasmonic vortex lens are shown for (b) LCP and (c) RCP incidence.

One of differences between the case shown in Figs. 3.2.1 and 3.2.2 is that the structure of Fig. 3.2.2 contains its own chiral geometry, which is a three-folded whirlpool-shape slit pattern. Such chirality of geometry can give a totally different response with respect to the incident polarization. In this case, it has been proved that an addition or subtraction of topological charge number of plasmonic vortex can be achieved. For the clear understanding, the definition of topological charge number will be explained. Let me consider a far-field optical beam or near-field SPP spot with a phase singularity at a certain point. Although the phase cannot be defined at the singular point, the phase profile along the circular path near the singular point should have a mathematical form of $\exp(jn\phi)$ [65]. Here, ϕ and n denote the azimuthal angle and the topological charge number of that singular point, respectively. The radius of plasmonic vortex lens linearly increases the amount of effective wavelength of the SPP mode (λ_{SPP}) at each segment of slit, therefore it

makes overall phase delay of 3 λ_{SPP} . Hence, plasmonic vortex will have topological charge of 3, when the spin-orbital interaction phenomenon is ignored. However, due to the spin-orbital interaction, the topological charge number of plasmonic vortex is added or subtracted by one according to the direction of optical polarization. Then, the size of plasmonic vortex can be expanded or squeezed, as shown in Figs. 3.2.2(b) and (c).

The key principle of the proposed structure in this chapter is applying the concept of addition or subtraction of topological charge number caused by spin-orbital interaction into the plasmonic bull's eye structure. The key concept is quite simple, but there are some differences between plasmonic lens and bull's eye geometry since the former case focuses the SPP itself into center point but latter is a beaming based on the diffracted light from surrounding gratings. In the next section, the geometry of proposed structure is shown, and then the difference of mechanism between the case of plasmonic lens and the proposed spiral bull's eye structure is compared based on the concept of spin-orbital interaction and topological charge numbers.

3.2.1.2. Principle of chiral beam generation

In Fig. 3.2.3, schematic diagrams for explaining the difference between abovementioned two cases, hot spot or vortex generation from plasmonic lens and beam generation from bull's eye geometry, are compared. For convenience, those two cases are simplified into two-dimensional structure in this figure. One can think these diagrams mean the cross section along the diameter of plasmonic lens and bull's eye structure, respectively. Firstly, Fig. 3.2.3(a) shows the case of plasmonic lens. Here, the backside-illuminated plane wave is coupled to the MIM mode inside the narrow metal slit patterned on the substrate. Throughout this chapter, it is assumed that the slit width is in subwavelength scale below the cutoff condition of anti-symmetric plasmonic mode. Therefore, only symmetric MIM plasmonic mode is coupled, which has symmetric E_x field component.

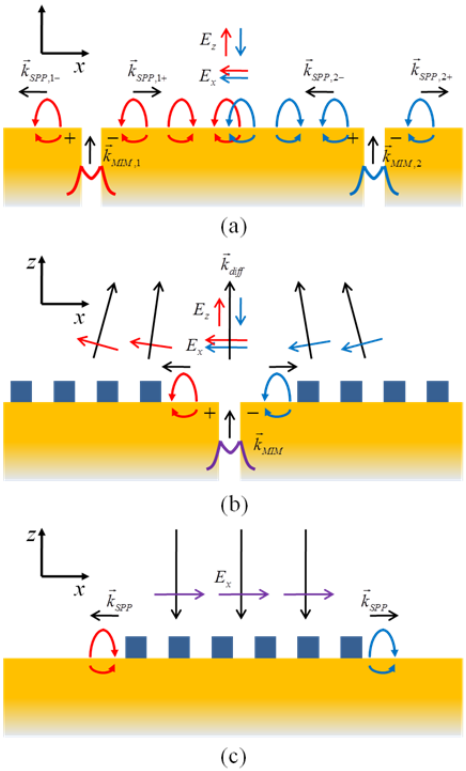

Figure 3.2.3. Schematic diagrams for explaining (a) the interference of two SPP modes generated from two slits, which is used for generating near field surface plasmon hot spot, and (b) the plasmonic beam generation by using the dielectric grating. Black solid arrows denote the wavevector of SPPs whereas red and blue arrows denote the directions of electric fields. (c) Schematic for the coupling from plane wave to SPP mode by the dielectric grating is shown in order to explain the phase shift compensation by the reciprocity of grating structure.

As mentioned in previous chapters, the exit-side of the metal slit can be regarded as a local capacitor and it accumulates the surface electron of the upper side of metal substrate. Due to the anti-symmetric E_z profile, it destructively interferes at the middle point of two metal slits when two SPPs generated from different slits are interfering each other as shown in Fig. 3.2.3(a). Although the electric field parallel to metal surface (E_x) constructively interferes at the center of slit, it is natural to consider that plasmonic dark spot is generated in this case since the E_z is much

stronger than E_x for SPPs mode. Therefore, to make the constructive interference of E_z, the π-phase shift between two opposite directional SPPs should be considered.

However, if the focus of interest is related to the far-field beaming via the radiative coupling of SPPs by gratings, the efficient beaming condition is quite different from the previous case and it follows the mechanism shown in Fig. 3.2.3(b). The surface plasmon generated from single slit or hole is similar to the case of Fig. 3.2.3(a), which means that the π-phase shift between left and right side of excited SPPs still remains. However, during the diffraction at the grating, this π-phase shift is compensated. The reason for such compensation is that another π-phase shift occurs when the SPPs are coupled to the diffracted field by the gratings. Such phenomenon can be simply explained by the reciprocal characteristic of the diffraction at the gratings. As depicted in Fig. 3.2.3(c), when normally incident plane wave illuminates the grating structure as used in Fig. 3.2.3(b), SPPs are generated on both sides of the grating ends. At the same phase, it is easy to suppose that the electric field parallel to metal surface should be in the same direction for the both sides of excited SPPs. Therefore, the SPPs generated at the right and the left ends of the structure have the same direction of the E_x field. At the same time, they have the same directions of electric fields (E_x), but the opposite directions of propagation. This means that π-phase shift is generated between both SPPs at the right and the left ends of the structure as shown in Fig. 3.2.3(c). Then, due to the reciprocity, it is possible to know that this π-phase shift also occurs when SPPs with opposite propagations encounter the surface grating, as shown in Fig. 3.2.3(b).

Therefore, unlike the case of plasmonic lens, geometrically generated π-phase shift is not needed for beaming from bull's eye structure. Moreover, the dominant field components for the plasmonic beaming are the two tangential field components (E_x, E_y), whereas that for the generation of SPP hot spots or vortex is one vertical field component (E_z). Therefore, it is not possible to consider the aspect of beaming from bull's eye structure with superposition of single scalar value as treated in the case of plasmonic lens.

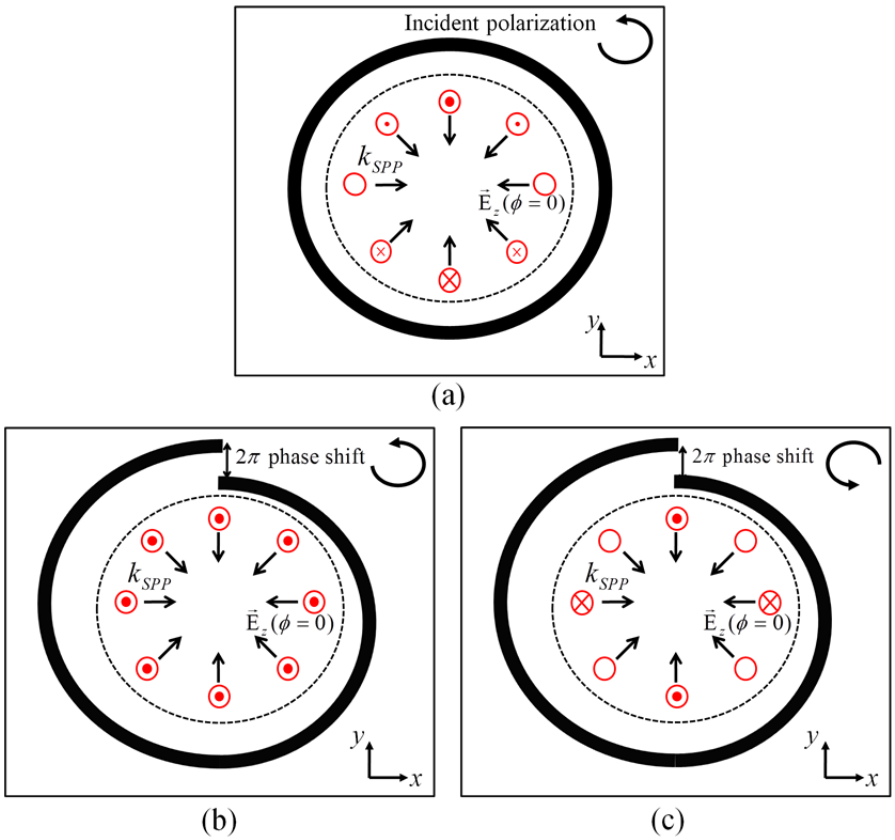

Figure 3.2.4. Schematic diagrams which show the wavevector and vertical electric field profile of the SPPs that are generated from (a) the circular slit structure with LCP light incidence, and those on the spiral slit structure (b) with LCP and (c) RCP light incidence.

From now, let me examine in detail the reason of these differences. Figure 3.2.4 shows the circular and spiral slit patterns used for the generation of switchable near field plasmonic hot spot and dark spot [28]. The black arrows denote the propagating directions of SPPs and red spots show the z-directional electric field at a fixed time. When the circularly polarized light is passing through the subwavelength slit, the phase delay caused by the evolution of the polarization state will modulate the phase of the excited SPPs by spin-orbital interaction. Therefore, when the circularity polarized light illuminates the simple circular slit pattern as in Fig. 3.2.4(a), the excited SPP has phase delay of 2π along the virtual contour inside the slit which is denoted with dashed

black line. This spin-assisted topological charge number is defined as l_{spin}. Since the E_z field directly follows the phase condition, the plasmonic vortex represented by the first order Bessel function of the first kind is generated rather than a hot spot [28]. To compensate these circular phase shift, geometrical modification as shown in Fig. 2(b) can be used. It shows that the phase delay generated by circularly polarized light can be compensated by introducing additional propagation delay of SPP mode when the radius of spiral slit is increasing in the direction opposite to polarization rotating direction to make an increment of λ_{SPP} for one cycle. In this case, all the SPPs have the same phase when they reach the center point so the plasmonic hot spot is generated. On the other hand, if the direction of rotation of polarization is the same as the increasing direction of spiral slit as in Fig. 3.2.4(c), the propagation delay gives additional phase delay to the initial phase delay so the angular momentum of plasmonic vortex can be increased. these angular momentum number compensated by the geometrical structure is defined as a geometrical topological charge number $l_{geometry}$. The E_z field distribution under this type of plasmonic lens structure can be given as [22],

$$E_z(r,\phi,z) \propto E_0 \exp(jk_z z)\exp(j(l_{spin}+l_{geometry})\phi)J_{(l_{spin}+l_{geometry})}(k_\rho r), \quad (3.2.1)$$

where k_z and k_ρ denote the wavenumber perpendicular to the metal plate and radial to the center axis, respectively. Here, we define the clockwise direction as a plus sign of topological charge so that the spin-assisted angular momentum l_{spin} is defined as $l_{spin} = +1$ for the right-handed circularly polarized (RCP) and $l_{spin} = -1$ for the left-handed circularly polarized (LCP) light incidence [28]. In the same convention, $l_{geometry}$ is -1 for the structure shown in Figs. 2(b) and (c). By Eq. (3.2.1) and structures shown in Fig. 2, the plasmonic vortex field generated by patterned slit can be simply switched by changing the incident polarization direction. It has been shown that the state $l_{spin} + l_{geometry} = n$ follows the vortex pattern of the n^{th} order Bessel function [28].

However, due to the differences in phase compensation mechanism and dominant field component as examined in Fig. 3.2.3, different explanation is needed for plasmonic beaming structure. In Fig. 3.2.5(a), the schematic diagram of bull's eye beaming structure is shown. The central metallic hole is surrounded by circular concentric gratings. Consider the case of the LCP light incidence. Similar to those in Fig. 3.2.4, black solid arrows denote the propagating wavevector. However, since the dominant field components are tangential fields, the colored

arrows denote the directions of tangential electric field components. The red arrows with dotted line near the gratings are the tangential electric field at specific time, and blue arrows with dashed line indicate those field components after π/2 phase has passed from the time of red arrows with dotted line.

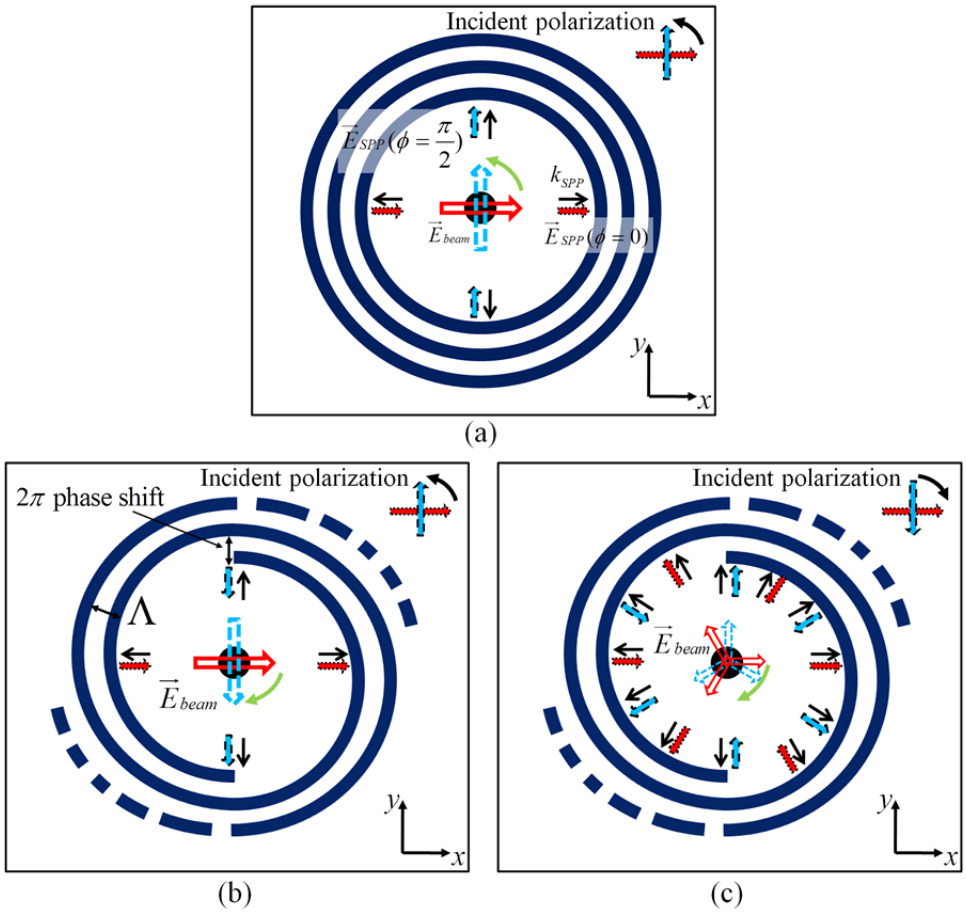

Figure 3.2.5. Schematic diagrams which show the wavevector and tangential electric field profile on (a) the bull's eye beaming structure with LCP light incidence, and on the clockwise rotating double spiral bull's eye structure (b) with LCP and (c) RCP light incidence.

The large arrows shown at the center are the directions of the tangential electric field of generated plasmonic beam measured above the metal surface. It should be pointed out that the phase of the tangential electric field component comprising the plasmonic beam is dependent on

the *z*-coordinate. Here, for the sake of convenience, these phases are set the same as that of the near-field electric component on the metal surface. Unlike the cases of Fig. 3.2.4, the fields generated from the left and right sides of the gratings do not make interference with those from the up and down sides of the gratings since they have vector components orthogonal to each other. Therefore, the polarization state at the center of beam is circular, the same direction as the incident plane wave.

Similar geometrical modification for the gratings can also be applied to that for the slits as shown in Figs. 3.2.5(b) and 3.2.5(c): the spiral grating structure. In these cases, the additional phase delay is generated along the radial increase of propagation length from the center hole to the starting position of grating. The field generated from the left and right sides are delayed by the phase of π due to the geometry but they are already $\pi/2$ phase faster than the fields generated from up and down sides due to the incident polarization. As a result, the incident LCP light is converted to the RCP light at the center of plasmon beam.

On the other hand, quite different results are obtained when the incident polarization has the same rotating directions with the spiral geometry as shown in Fig. 3.2.5(c). In this case the phase delays generated by polarization state and geometry are added to each other, so that the fields generated from the left and right sides have $3\pi/2$ phase slower than fields generated from up and down side gratings, which can be drawn like small colored arrows in Fig. 3.2.5(c). If the amplitude of diffracted light are assumed to be identical along all of the radial direction, all of the small arrows are equally contributed to the field generated at the central axis of plasmonic beam. Then, the vector sum of these field components is completely cancelled to each other at the center axis regardless of its phase state, which prohibits the beaming along the *z*-direction.

There is a difference of plasmonic hot spot generations and plasmonic beaming conditions. In the first case, the condition of $l_{total} = 0$ makes all the SPPs have the same phase, resulting in the plasmonic hot spot. However, the plasmonic beaming is generated when the vector sum of the tangential components is constructively interfered. This condition is only satisfied when the topological charge of E_z field satisfies $l_{total} = \pm 1$ along the z-axis. For the case of simple bull's eye structure, the condition of $l_{total} = \pm 1$ is satisfied by both circular polarizations so that the linear polarization can also generate beam. However, this does not violate the beaming condition since the π phase shift still remains along the line perpendicular to the incident linear polarization direction. In the next section, full-3D numerical results for the proposed double spiral Bull's eye

geometry are discussed. In addition to them, numerical calculations on the polarization-dependent light collection by using the inverted spiral bull's eye geometry will be also introduced.

3.2.2. Numerical results of chiral bull's eye geometry

3.2.2.1. Switchable beam generation from double spiral bull's eye

In this section, at first, the field profile generated from the conventional bull's eye geometry is reproduced for the reference.

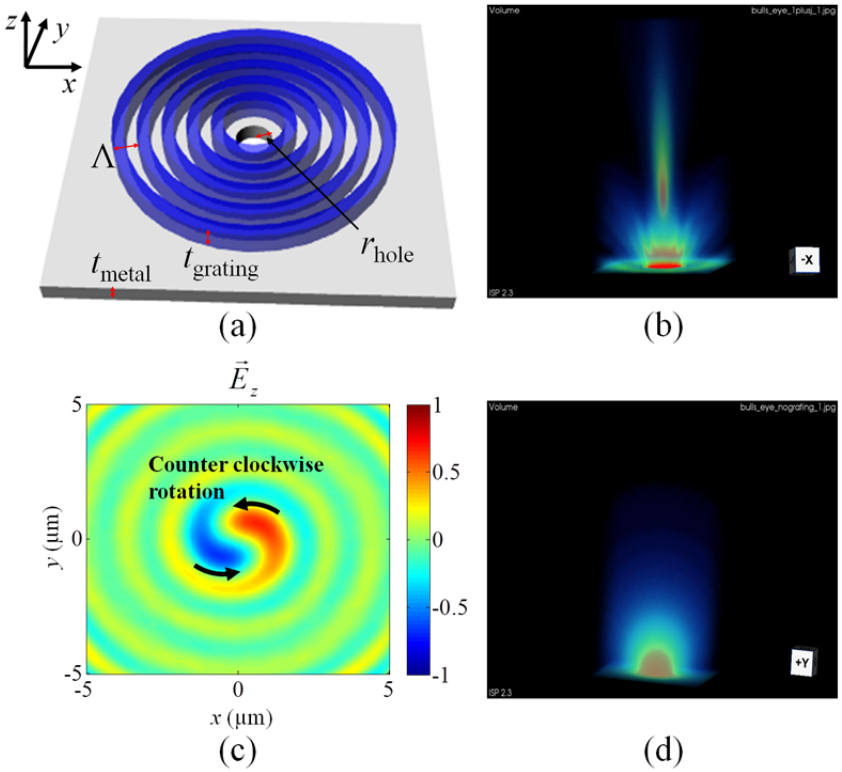

Figure 3.2.6. (a) Schematic diagram of the bull's eye configuration used for numerical calculation. (b) Three-dimensional view of the electric field intensity distribution of bull's eye structure with LCP light incidence, ranged from 0 μm to 20 μm above the dielectric grating layer and (c) vertical electric field (E_z) distribution on the z = 10 μm plane. (d) Three-dimensional view of the electric field intensity distribution of single hole without the gratings

In Fig. 3.2.6(a), the schematic of bull's eye structure used in numerical simulation is shown. The free space wavelength λ, radius of hole r_{hole}, period of grating Λ, thickness of metal layer t_{metal}, thickness of dielectric grating layer $t_{grating}$, are set to λ = 650 nm, r_{hole} = 100 nm, Λ = 450 nm, t_{metal} = 250 nm, and $t_{grating}$ = 400 nm, respectively. These parameters are based on the values which are optimized to the efficient generation of plasmonic beaming [66].

Figure 3.2.6(b) shows three-dimensional electric field intensity distribution of plasmonic beam generated by bull's eye structure when the incident plane wave is LCP. The full-width at half-maximum (FWHM) of the plasmonic beam, which is measured (in simulation) 6.5 μm above the grating, is obtained as 976 nm. It is clearly shown that, along the *z*-axis, the plasmonic beam is strongly formed, since this condition is related to the case of Fig. 3.2.5(a). Although the dominant field components for plasmonic beaming are the tangential components, the vectorial nature of these field components makes it difficult to illustrate the phase rotating characteristics. However, the vertical field component is scalar component and directly related to the phase characteristic. Consequently, it is possible to determine the topological charge number of plasmonic beam from E_z field. Figure 3.2.6(c) shows the distribution of E_z field on the 10 μm above the grating.

It is clearly shown that the field is rotating counter-clockwise with one phase cycle, which proves that the beam has a topological charge number of $l_{total} = +1$, as expected in Fig. 3.2.5(a). Note that the *x*-polarized light makes *x*-polarized beaming and *y*-polarized light makes *y*-polarized beaming along the *z*-axis for bull's eye structure. Since there are no artificial phase delay formed by the geometry, incident polarization is not changed by any polarization state of incident field. This means that bull's eye structure has polarization-independent beaming characteristics so it cannot be use for a polarization-dependent switching device. In Fig. 3.2.6(d), electric field intensity distribution is shown when the LCP light illuminates the metallic hole without the grating pattern. It is shown that the electric field transmitted from the hole without grating is exponentially decayed since the hole size is a subwavelength scale.

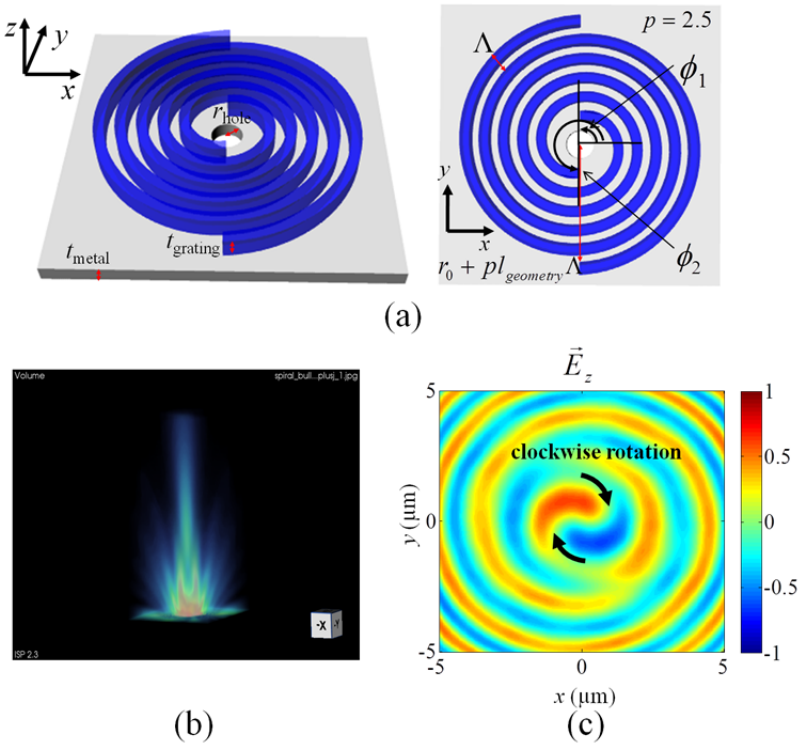

Figure 3.2.7. (a) Schematic diagram of the proposed double spiral bull's eye configuration used for numerical calculation. (b) Three-dimensional view of the electric field intensity distribution of double spiral bull's eye structure with LCP light incidence ranged from 0 μm to 20 μm above the dielectric grating layer and (c) vertical electric field (E_z) distribution on the z = 10 μm plane.

As mentioned earlier in previous section, the polarization-dependent switchable beaming could be demonstrated by using the double spiral bull's eye structure. Figure 3.2.7(a) illustrates the proposed double spiral bull's eye structure composed of metallic hole and surrounding spiral-shaped dielectric gratings. The parameters already defined in conventional bull's eye structure such as r_{hole}, Λ, t_{metal}, and $t_{grating}$ are set to be the same value as used in Fig. 3.2.6. Unlike the folded plasmonic vortex lens slit for the generation of near field plasmonic vortex, the double spiral bull's eye structure requires continuously coiled structure. This is because the periodic grating profile is needed for the diffraction to the specific angle that can generate a plasmonic beam [60]. The radius of single spiral grating continuously increases along the azimuthal angle, so that the radius of spiral grating will be provided as a function of azimuthal angle,

$$r_{spiral,i}(\phi) = r_0 + \frac{l_{geometry}\Lambda}{2\pi}(2\pi p + \phi_i - \phi) \quad (\text{i} = 1, 2, \ldots \text{n}, \ \phi_i \le \phi \le \phi_i + 2\pi p), \tag{3.2.2}$$

where n, p, $l_{geometry}$, r_0, and ϕ_i denote the total number of spiral dielectric grating, the winding number of each spiral grating, the geometrical angular momentum of overall grating structure, the initial radius of spiral grating, and the initial offset of the azimuthal angle of each spiral grating, respectively. The minus sign used in the azimuthal angle term is due to the clockwise direction of spiral grating. In the simulations shown in Figs. 3.2.7 and 3.2.8, the parameter of $n = 2$ (double spiral structure), $p = 2.5$, $l_{geometry} = +2$ (clockwise), $r_0 = \frac{\Lambda}{2} + r_{hole}$, $\phi_1 = \frac{\pi}{2}$, and $\phi_2 = \frac{3\pi}{2}$ are used. Although the number of spiral gratings is not directly related to the geometrical angular momentum, the symmetry of structure is broken if only the single spiral structure is used. This makes symmetry breaking of the coupling intensity along the circulation, which produces unwanted distortion to overall beaming characteristics. Therefore symmetric double spiral structure is preferred rather than single spiral to preserve the on-axis beaming.

Figure 3.2.7(b) shows the 3D electric field intensity distribution above the grating when the LCP (counter-clockwise) light is illuminated from the backside. Note that the strong beam is generated along the *z*-axis similar to the case of bull's eye structure. This can be explained by simple summation of angular momentum as explained in Eq. (3.2.1). In this case the topological charge of $l_{total} = +1$ is obtained since the value of l_{spin} is –1. The topological charge of +1 can be obviously shown in Fig. 3.2.7(c), which illustrates the E_z field on the z = 10 μm plane. It is noteworthy that only one cycle of phase modulation is detected near the *z*-axis and it circulates along the *clockwise* direction, even though the incident polarization has *counter-clockwise* rotation direction. This means the double spiral grating structure successfully changes the angular momentum of the generated beam and finally changes the polarization state. In fact, efficient on-axis beaming with circular polarization can be generated when the topological charge is +1 or –1, by using the bull's eye structure. It can be assumed that the bull's eye structure is a grating structure which has a geometrical angular momentum of zero, which makes absolutely the same intensity pattern regardless of rotation direction of polarization. Therefore, when the LCP light illuminates the proposed double spiral bull's eye structure, it can efficiently generate plasmonic beam as if the RCP light illuminated the conventional bull's eye structure since they have exactly the same topological charge number.

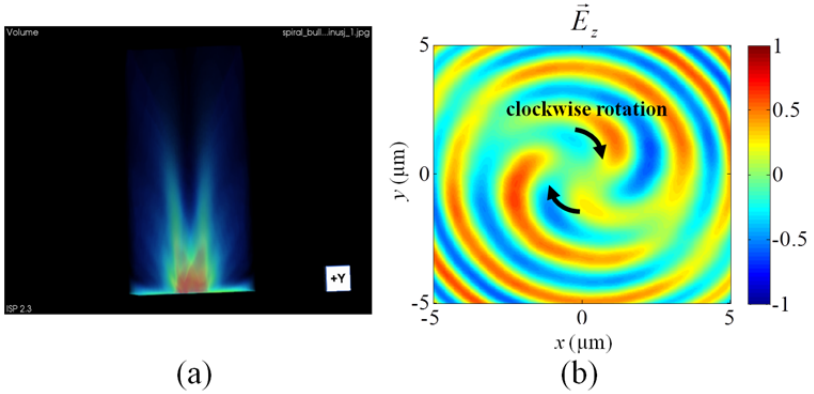

Figure 3.2.8. (a) Three-dimensional view of the electric field intensity distribution of double spiral bull's eye structure with RCP light incidence, ranged from 0 μm to 20 μm above the dielectric grating layer and (b) vertical electric field (E_z) distribution on the z = 10 μm plane.

However, when the polarization state of incident beam is RCP (clockwise), the topological charge number will be $l_{total} = +3$. The overall beam shape for this case is illustrated in Fig. 3.2.8(a). It shows quite different beam pattern from that shown in Fig. 3.2.7(b). Although the beams are generated above the double spiral grating structure, these beams are split into two main lobes and helically diverging along the propagation direction rather than merging along the *z*-axis. According to the explanation in previous section, let me assume that the spiral geometry only affects the phase delay mechanism, so that the field intensity pattern should have circular symmetric profile. However, there are side effects of spiral geometry such as phase discontinuity at the starting point of the spiral grating, diffracted light generation position mismatch due to the geometry, and coupling intensity mismatch due to the metallic loss difference. As a result, the circular symmetry of field intensity cannot be maintained. Nevertheless the angular momentum conservation is well-matched and it can be viewed by the same manner used in Fig. 3.2.7(c). The E_z field on the z = 10 μm plane for the case RCP light illumination is shown in Fig. 3.2.8(b). It shows that the field amplitude of the center point is relatively weak, and the field distribution near the center point has about three cycles of phase modulation and it also circulates along the clockwise direction. This means the topological charge of this beam is +3, as expected in Fig. 3.2.5(c).

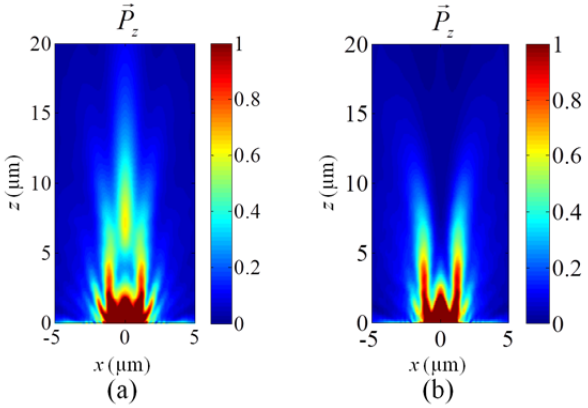

Figure 3.2.9. Distributions of z-directional power flow of the proposed double spiral bull's eye structure on the y = 0 plane with the (a) LCP and (b) RCP light incidence. The color scales are in the same scale of normalized power both in (a) and (b).

By using the polarization dependent beam characteristics of the proposed double spiral grating structure, the plasmonic beaming can be switched by changing the polarization states. To provide a clear view for the switching characteristic of the proposed structure, the *z*-directional power flow distributions on the $y = 0$ plane for the cases of LCP and RCP light illumination are compared in Figs. 3.2.9(a) and 3.2.9(b). It is clearly formed that bright spot along the *z*-axis is formed for LCP light incidence but is not shown in RCP light incidence. The on-off ratio of the proposed switchable beaming structure is obtained as 23.3 dB, which is defined as the ratio of *z*-directional time averaged power flow passing through a circular area of diameter of 976 nm located on $z = 8.5$ μm plane of the LCP incidence case divided by the RCP light incident case.

3.2.2.2. Polarization-dependent light collection from inverted spiral bull's eye

Although the main issue of this chapter is finished in section 3.2.2.1, an alternative approach of the proposed spiral bull's eye geometry is briefly discussed in order to demonstrate a polarization sensitive light collection.

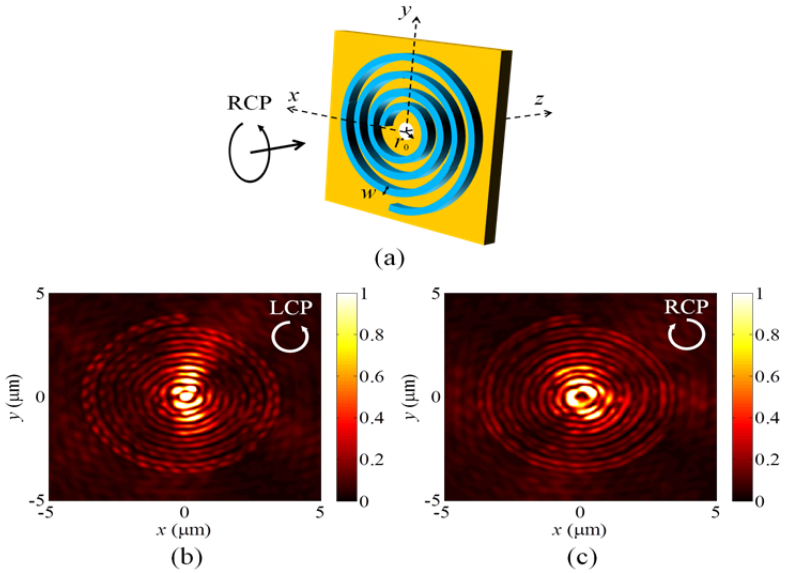

Figure 3.2.10. (a) Schematic diagram of spiral bull's eye structure for the polarization-dependent enhancement of nanohole transmission. Electric field intensity distributions of 10 nm backside of the metal substrate with the (b) LCP and (c) RCP incident waves are shown respectively for comparison of the field intensity at the center point.

As discussed previously, the spiral bull's eye geometry can radiate the SPPs into far-field beam. Then it is possible to suppose that it should react polarization-sensitively for collection of far-field incident light into SPP source due to the reciprocity.

Consider the case of the spiral bull's eye structure when it is located at the backside of the metal substrate as shown in Fig. 3.2.10(a). In this case, specific symmetry is not needed unlike the case of previous section. Therefore, optimized structure is formed as a single spiral structure, the continuous increase of the radius finally provides an Archimedean spiral grating structure. The radius of the grating can be expressed by the simple relation $r(\phi) = r_1 + \Lambda\phi/2\pi$, where the parameters λ_0, r_0, r_1, and w are set to λ_0 = 800 nm, r_0 = 50 nm, r_1 = 100 nm, and w = Λ/2, respectively. When the spiral bull's eye is used, transmission efficiency enhancement is highly sensitive to the incident polarization state due to the chiral geometry [67]. The role of gratings is to couple the incident wave into the SPPs and merging them to the nanohole by their circular-shaped geometry. However, due to the phase delay caused by the spiral geometry, merged SPPs

interfere differently at the center point varying with the incident polarization state. Figures 3.2.10(b) and 3.2.10(c) depict the electric field intensity distribution with RCP and LCP light incidence on the plane 10 nm backside from the metal substrate, respectively. The field intensity at the center point is dramatically changed by the direction of the optical handedness. As a result, modulation of the field intensity at the center point finally affects the transmission efficiency.

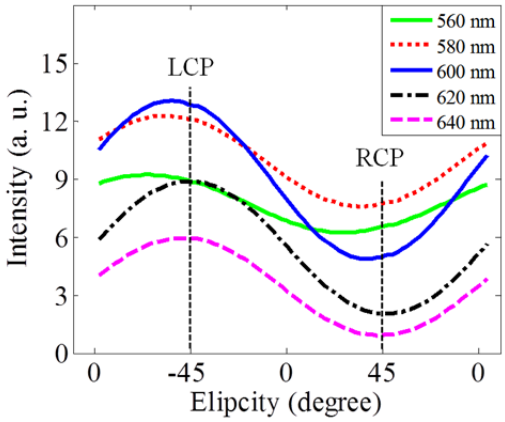

Figure 3.2.11. Transmission efficiencies varying with the optical polarization are shown with several grating periods. The results are normalized to the value of transmission without the spiral gratings.

This aspect is clearly shown in Fig. 3.2.11. Transmission efficiency through the nanohole is strongly dependent on the polarization ellipticity, which has the highest value near an ellipticity of -45°, and is related to the LCP state shown in Fig. 3.2.10(b). In addition, the results also show that the effect of the grating period is quite important in terms of enhancing efficiency. Both the polarization sensitivity and overall transmission efficiency could be maximized near the condition of $\Lambda = 600$ nm. This condition is well-matched to the highest SPP excitation condition in conventional bull's eye geometry, which is numerically calculated by RCWA simulation [66].

Chapter 4

Conclusion

Throughout this dissertation, revealing and demonstrating the methods to modulate the direction of surface plasmon excitation from nanoslit or beaming from nanohole structure is the main focus. These switchable schemes of SPP launching are demonstrated by various types of control factor, such as polarization state and relative phase differences. Especially in Chapter 2, these two types of SPP switching mechanism is well-established with appropriate physical insights and they are also demonstrated in experiments.

In the first part of Chapter 2, basic principles of SPPs and propagating SPP waveguide mode characteristics in single interface and MIM waveguide structure are introduced. Throughout this dissertation, most of the physical phenomenon is based on the SPP mode coupling which can be explained by induced charge characteristics near the nanoslit and nanohole structure. Therefore the contents included in the first part of Chapter 2 can be the background knowledge to understand this dissertation. Then, in the second part of Chapter 2, a method for unidirectional launching from nanoslit which can be switched by incident polarization is discussed. The physical origin of this switchable scheme is based on the interference of anti-symmetric SPP excitation from TE incidence and symmetric SPP excitation from TM incidence. Among them, the origin of the latter excitation method was firstly explained by using the magnetic induction current near the nanoslit. Appropriate combinations of two types of polarization give a unidirectional launching, and it is predicted that unidirectional launching condition appears near the circular polarization

state by analyzing the charge accumulation model. Then, the experimental demonstration of polarization dependent SPP directional switching is followed and verifies the analytic model discussed in this part. It is expected that this method can be commonly applied to plasmonic switching device in integrated plasmonic circuit since the change of polarization state is one of the most frequently used methods even for on/off switching in conventional optical devices such as liquid crystal display. However, the limitation of the method explained in the second part of Chapter 2 is an oblique propagation of SPPs from the nanoslit. Moreover, it is well-known that the switching speed of the incident polarization state is quite slow in reality. In last part of Chapter 2, such problems are solved by demonstrating a novel switching mechanism which is done by the phase-modulation of incident beam. In this configuration, two beams which have the same incident wavelength simultaneously illuminate nanoslit with opposite incident angles hence the interference pattern is generated above the metal substrate. It is revealed that the excited SPPs from nanoslit can have either anti-symmetric or symmetric profile according to the relative position of nodal lines of interference pattern and the position of nanoslit. By interfering those two types of excitations, a unidirectional launching of SPPs controlled by phase difference between two incident beams is demonstrated. Experimental demonstrations of proposed switchable launching scheme is done by using the electro-motively driven peizostage, which slightly moves the optical path of controlled beam by applied electric voltage. The method discussed in this chapter can also be applied to plasmonic switch, which needs much faster operating speed than polarization-based modulations.

By using the modulation mechanisms of SPPs which are explained in Chapter 2, compact switchable plasmonic device applications are proposed in Chapter 3. The scheme of switchable SPPs launching from nanoslit discussed in the first part of Chapter 3 is a plasmonic dichroic splitting, which means a switching of launching direction according to its optical wavelength. To demonstrate it, a basic concept of polarization dependent switchable SPP launching explained in Chapter 2 is applied to a MIM waveguide structure. Unlike the single metallic layer considered in Chapters 2, input region formed by input slit and MIM waveguide form strong optical cavity structure of SPP mode. Therefore, strong FP resonances are generated at the input region. These FP modes appear in totally different conditions according to incident polarization state due to the symmetry of excited SPPs as discussed in Chapter 2. In a certain geometry conditions, it is possible to make two proposed laser beams in different wavelengths propagate into the opposite directions of MIM waveguide, by locating the FP resonance condition between two proposed wavelengths. Experimental demonstrations verify the numerical analysis. Sorting the photons

according to their optical wavelength has been considered as an important issue in optical spectrum analysis. Therefore, it is anticipated that this scheme can be applied to ultra-small plasmonic spectrum analyzer which can be operated in chip-scale.

In addition, in the second part of Chapter 3, device for switchable beaming of SPPs is considered for the out-coupling of SPPs and their modulation, By applying the chiral geometry into the plasmonic bull's eye structure, which is a subwavelength aperture surrounded by dielectric gratings, polarization-dependent switchable beaming has been achieved. The chiral geometry of spiral grating structure can change the angular momentum of generated beam during the diffraction at gratings. On- and off-state of the proposed structure are determined by the condition of optical chirality of incident beam.

As discussed in the introduction part of this dissertation, plasmonics is one of the most fascinating fields in nano-photonics due to numerous benefits which can be applicable to subwavelength imaging, integrated optics and sensing of nano-size materials. Especially, plasmonic switching device is quite important for realizing integrated plasmonic system. It is anticipated that the various switching methods discussed in this dissertation can provide a route for utilizing a practical active plasmonic system, and even can be applied to the realization of all-optical computing which can be operated in micro-scale chips.

Bibliography

1. H. Raether, *Surface Plasmons on Smooth and Rough Surfaces and on Gratings* (Springer-Verlag, 1988).

2. A. Liebsch, *Electronic Excitations at Metal Surfaces* (Springer-Verlag, 1997).

3. W. L. Barnes, A. Dereux, and T. W. Ebbesen, "Surface plasmon subwavelength optics," Nature **424**, 824–830 (2003).

4. B. Lee, I.-M. Lee, S. Kim, D.-H. Oh, and L. Hesselink, "Review on subwavelength confinement of light with plasmonics," J. Mod. Opt. **57**, 1479–1497 (2010).

5. T. W. Ebbesen, H. J. Lezec, H. F. Ghaemi, T. Thio, and P. A. Wol, "Extraordinary optical transmission through sub-wavelength hole arrays," Nature **391**, 667–669 (1998).

6. E. Ozbay, "Plasmonics: merging photonics and electronics at nanoscale dimensions," Science **311**, 189–193 (2006).

7. T. Ergin, N. Stenger, P. Brenner, J. B. Pendry, and M. Wegener, "Three-dimensional invisibility cloak at optical wavelengths," Science **328**, 337–339 (2010).

8. D. OConnor, M. McCurry, B. Lafferty, and A. V. Zayats, "Plasmonic waveguide as an efficient transducer for high-density data storage," Appl. Phys. Lett. **95**, 171112 (2009).

9. K. Nakayama, K.Tanabe, and H. A.Atwater, "Plasmonic nanoparticle enhanced light absorption in GaAs solar cells," Appl. Phys. Lett. **93**, 121904 (2008).

10. A. F. Koenderink, "Plasmon nanoparticle array waveguides for single photon and single plasmon sources," Nano Lett. **9**, 4228–4233 (2009).

11. K. T. V. Grattan and B. T. Meggitt, *Optical Fiber Sensor Technology* (Chapman & Hall 1998).

12. J. a Schuller, E. S. Barnard, W. Cai, Y. C. Jun, J. S. White, and M. L. Brongersma, "Plasmonics for extreme light concentration and manipulation," Nature Materials **9**, 193–204 (2010).

13. H. J. Lezec, J. A. Dionne, and H. A. Atwater, "Negative refraction at visible frequencies," Science **316**, 430–432 (2007).

14. M. Kuwata-Gonokami, N. Saito, Y. Ino, M. Kauranen, K. Jefimovs, T. Vallius, J. Turunen, and Y. Svirko, "Giant optical activity in quasi-two-dimensional planar nanostructures," Phys. Rev. Lett. **95**, 227401 (2005).

15. M. A. Seo, H. R. Park, S. M. Koo, D. J. Park, J. H. Kang, O. K. Suwal, S. S. Choi, P. C. M. Planken, G. S. Park, N. K. Park, Q. H. Park and D. S. Kim, "Terahertz field enhancement by a metallic nano slit operating beyond the skin-depth limit," Nature Photonics **3**, 152–156 (2009).

16. S. Kawata, Y. Inouye, and P. Verma, "Plasmonics for near-field nano-imaging and superlensing," Nature Photonics **3**, 388–394 (2009).

17. A. V. Kabashin, P. Evans, S. Pastkovsky, W. Hendren, G. A. Wurtz, R. Atkinson, R. Pollard, V. A. Podolskiy and A. V. Zayats, "Plasmonic nanorod metamaterials for biosensing," Nature Materials **8**, 867–871 (2009).

18. B. Luk'yanchuk, N. I. Zheludev, S. A. Maier, N. J. Halas, P. Nordlander, H. Giessen, and C. T. Chong, "The Fano resonance in plasmonic nanostructures and metamaterials," Nature Materials **9**, 707–715 (2010).

19. Y. Avitzour, Y. A. Urzhumov, and G. Shvets, "Wide-angle infrared absorber based on a negative-index plasmonic metamaterial," Phys. Rev. B **79**, 045131 (2009).

20. H. A. Atwater and A. Polman "Plasmonics for improved photovoltaic devices," Nature Materials **9**, 205–213 (2010).

21. A. Boltasseva and H. A. Atwater, "Low-loss plasmonic metamaterials," Science **331**, 290–291 (2011).

22. F. H. L. Koppens, D. E. Chang, and F. J. García de Abajo, "Graphene plasmonics: a platform for strong light–matter interactions," Nano Lett. **11**, 3370–3377 (2011).

23. M. I. Stockman, "Nanofocusing of optical energy in tapered plasmonic waveguides," Phys. Rev. Lett. **93**, 137404 (2004).

24. S.-Y. Lee, J. Park, I. Woo, N. Park, and B. Lee, "Surface plasmon beam splitting by the photon tunneling through the plasmonic nanogap," Appl. Phys. Lett. **97**, 133113 (2010).

25. Z. Liu , J. M. Steele , W. Srituravanich , Y. Pikus , C. Sun , and X. Zhang , "Focusing surface plasmons with a plasmonic lens," Nano Lett. **5**, 1726–1729 (2005).

26. S. I. Bozhevolnyi1 V. S. Volkov, E. Devaux, J.-Y. Laluet and T. W. Ebbesen, "Channel plasmon subwavelength waveguide components including interferometers and ring resonators," Nature **440**, 508–511 (2006).

27. S.-Y. Lee, J. Park, M. Kang, and B. Lee, "Highly efficient plasmonic interconnector based on the asymmetric junction between metal-dielectric-metal and dielectric slab waveguides," Opt. Express, **19**, 9562-9574 (2011).

28. H. Kim, J. Park, S.-W. Cho, S.-Y. Lee, M. Kang, and B. Lee, "Synthesis and dynamic switching of surface plasmon vortices with plasmonic vortex lens," Nano Lett. **10**, 529–536 (2010).

29. A. V. Krasavin, A. V. Zayats, and N. I. Zheludev, "Active control of surface plasmon–polariton waves," J. Opt. A **7**, S85–S89 (2005).

30. R. Charbonneau, N. Lahoud, G. Mattiussi, and P. Berini, "Demonstration of integrated optics elements based on long-ranging surface plasmon polaritons," Opt. Express **13**, 977–984 (2005).

31. R. Charbonneau, C. Scales, I. Breukelaar, S. Fafard, N. Lahoud, G. Mattiussi, and P. Berini," Passive integrated optics elements based on long-range surface plasmon polaritons," J. Light Technol. **24**, 477–494 (2006).

32. D. Pacifici, H. J. Lezec, and H. A. Atwater, "All-optical modulation by plasmonic excitation of CdSe quantum dots," Nature Photonics **1**, 402–406 (2007).

33. H. Wei, Z. Li, X. Tian, Z. Wang, F. Cong, N. Liu, S. Zhang, P. Nordlander, N. J. Halas, and H. Xu,"Quantum dot-based local field imaging reveals plasmon-based interferometric logic in silver nanowire networks," Nano Lett. **11**, 471–475 (2011).

34. J. A. Dionne, K. Diest, L. A. Sweatlock, and H. A. Atwater "PlasMOStor: a metal− oxide− Si field effect plasmonic modulator," Nano Lett. **9** 897–902 (2009).

35. P. Lalanne, J. P. Hugonin, and J. C. Rodier, "Theory of surface plasmon generation at nanoslit apertures," Phys. Rev. Lett. **95**, 263902 (2005).

36. J. A. Dionne, L. A. Sweatlock, H. A. Atwater, and A. Polman, "Planar metal plasmon waveguides: frequency-dependent dispersion, propagation, localization, and loss beyond the free electron model," Phys. Rev. B **72**, 075405 (2005).

37. J. Chen, Z. Li, M. Lei, S. Yue, J. Xiao, and Q. Gong, "Broadband unidirectional generation of surface plasmon polaritons with dielectric–film–coated asymmetric single–slit," Opt. Express **19**, 26463–26469 (2011).

38. T. Xu, Y. Zhao, D. Gan, C. Wang, C. Du, and X. Luo, " Directional excitation of surface plasmons with subwavelength slits," Appl. Phys. Lett. **92**, 101501 (2008).

39. F. López-Tejeira, S. G. Rodrigo, L. Martín-Moreno, F. J. García-Vidal, E. Devaux, T. W. Ebbesen, J. R. Krenn, I. P. Radko, S. I. Bozhevolnyi, M. U. González, J. C. Weeber, and

A. Dereux, " Efficient unidirectional nanoslit couplers for surface plasmons," Nature Phys. **3**, 324–328 (2007).

40. J. Homola, S. S. Yeea, and G. Gauglitzb, "Surface plasmon resonance sensors: review," Sensors and Actuators B **54**, 3–15 (1999).

41. B. Lee, S. Roh, and J. Park, "Current status of micro- and nano-structured optical fiber sensors," Opt. Fiber Technol., **15**, 209–221 (2009).

42. H. Shin and S. Fan, "All-angle negative refraction for surface plasmon waves using a metal-dielectric-metal structure, " Phys. Rev. Lett. **96**, 073907 (2006).

43. Y. Lim, S.-Y. Lee, K.-Y. Kim, J. Park, and B. Lee, "Negative refraction of Airy plasmons in a metal-insulator-metal waveguide," IEEE Photon. Tech. Lett., **23**, 1258–1260 (2011).

44. K. L. Tsakmakidis, A. D. Boardman, and O. Hess, "Trapped rainbow storage of light in metamaterials, " Nature **450**, 397–401 (2007).

45. J. Park, K.-Y. Kim, I.-M. Lee, H. Na, S.-Y. Lee, and B. Lee, "Trapping light in plasmonic waveguides, " Opt. Express **18**, 598–623 (2010).

46. Z. Han, L. Liu, and E. Forsberg, "Ultra-compact directional couplers and Mach–Zehnder interferometers employing surface plasmon polaritons," Opt. Comm., **259**, 690–695 (2006).

47. G. Lvque and O. J. F. Martin, "Transient behavior of surface plasmon polaritons scattered at a subwavelength groove," Phys. Rev. B **76**, 155418 (2007).

48. A. Yu. Nikitin, F. J. Garca-Vidal, and L. Martn-Moreno, "Oblique launching of optical surface waves by a subwavelength slit," Phys. Rev. B **83**, 155448 (2011).

49. S.-Y. Lee, I.-M. Lee, J. Park, S. Oh, W. Lee, K.-Y. Kim, and B. Lee, "Role of magnetic induction currents in nanoslit excitation of surface plasmon polaritons," Phys. Rev. Lett. **108**, 213907, (2012).

50. E. D. Palik, *Handbook of Optical Constants of Solids 2nd ed.* (Academic Press, San Diego, 1998).

51. J. H. Kang, D. S. Kim, and Q. H. Park, "Local capacitor model for plasmonic electric field enhancement," Phys. Rev. Lett. **102**, 093906 (2009).

52. J. D. Jackson, *Classical Electrodynamics*, 3rd ed. (Wiley, 1998).

53. H. Kim, J. Park, and B. Lee, *Fourier Modal Method and Its Applications in Computational Nanophotonics* (CRC Press, Boca Raton, FL, 2012).

54. G. Lerosey, D. F. P. Pile, P. Matheu, G. Bartal and X. Zhang, "Controlling the phase and amplitude of plasmon sources at a subwavelength scale," Nano Lett. **9**, 327–331 (2009).

55. J. Park, H. Kim, I.-M. Lee, S. Kim, J. Jung, and B. Lee, "Resonant tunneling of surface plasmon polariton in the plasmonic nano-cavity," Opt. Express, **16**, 16903–16915, (2008).

56. J. S. Q. Liu and R.A. Pala, F. Afshinmanesh, W. Cai, and M.L. Brongersma, "A submicron plasmonic dichroic splitter," Nat. Commun. **2**, 525 (2011).

57. H.W. Kihm, K.G. Lee, D.S. Kim, J.H. Kang, and Q.-H. Park, "Control of surface plasmon generation efficiency by slit-width tuning," Appl. Phys. Lett. **92**, 051115 (2008).

58. H. Kim and B. Lee, "Unidirectional surface plasmon polariton excitation on single slit with oblique backside illumination," Plasmonics, **4**, 153-159, (2009).

59. H. J. Lezec, A. Degiron, E. Davaux, R. A. Linke, L. Martin-Moreno, F. J. Garcia-Vidal, and T. W. Ebbesen, "Beaming light from a subwavelength aperture," Science **297**, 820–822 (2002).

60. S. Kim, H. Kim, Y. Lim, and B. Lee, "Off-axis directional beaming of optical field diffracted by a single subwavelength metal slit with asymmetric dielectric surface gratings," Appl. Phys. Lett. **90**, 051113 (2007).

61. S. Kim, Y. Lim, H. Kim, J. Park, and B. Lee, "Optical beam focusing by a single subwavelength metal slit surrounded by chirped dielectric surface gratings," Appl. Phys. Lett. **92**, 013103 (2008).

62. Y. Gorodetski, A. Niv, V. Kleiner, and E. Hasman, "Observation of the spin-based plasmonic effect in nanoscale structures," Phys. Rev. Lett. **101**, 043903 (2008).

63. L. Marrucci, C. Manzo, and D. Paparo, "Optical spin-to-orbital angular momentum conversion in inhomogeneous anisotropic media," Phys. Rev. Lett. **96**, 163905 (2006)

64. G. M. Lerman, A. Yanai, and U. Levy, "Demonstration of nanofocusing by the use of plasmonic lens illuminated with radially polarized light," Nano Lett. **9**, 2139–2143 (2009).

65. A. T. O'Neil, I. MacVicar, L. Allen, and M. J. Padgett, "Intrinsic and extrinsic nature of the orbital angular momentum of a light beam," Phys. Rev. Lett. **88**, 053601 (2002).

66. H. Kim, J. Park, and B. Lee, "Finite-size nondiffracting beam from a subwavelength metallic hole with concentric dielectric gratings," Appl. Optics, **48**, G68–G72 (2009).

67. A. Drezet, C. Genet, J.-Y. Laluet and T. W. Ebbesen, "Optical chirality without optical activity: How surface plasmons give a twist to light," Opt. Express **16**, 12559–12570 (2008).

한글 초록

표면 플라즈몬은 금속 표면의 자유 전자와 광자간의 공진에 의한 현상으로, 파장 이하 크기로의 집속이 가능하고 금속 표면에서의 강한 전자기장 증폭을 야기할 수 있어, 활발한 연구가 이루어지고 있다. 특히 표면 플라즈몬을 이용한 광학 소자는 높은 광 집속도와 빠른 정보처리 효과를 동시에 가지는, 집적 광 회로의 구현과 초고밀도 광 저장 장치의 개발에 있어 요구되며, 이러한 광학 소자를 흔히 플라즈모닉 소자라고 칭한다. 플라즈모닉 소자를 이용한 집적 시스템은 기존의 전자회로의 한계를 극복하고, 광 컴퓨팅 또는 양자 컴퓨팅의 구현에 있어서도 큰 기여를 할 것으로 기대되고 있다.

플라즈모닉 소자 기반 연산에 있어 중요한 부분 중 하나는 표면 플라즈몬의 스위칭이라 할 수 있다. 본 논문에서 다루고자 하는 핵심 내용은 금속 슬릿이나 금속 개구 구조를 기반으로 하는 플라즈모닉 소자에서 표면 플라즈몬의 여기를 변조하는 방법들에 대한 물리적 고찰과 구조의 설계 및 구현이다. 특히 2 장에서는 표면 플라즈몬을 변조할 수 있는 여러 가지 기법들에 대해 설명하고 있는데, 2 장 2 절에서는 금속 슬릿으로부터 여기되는 표면 플라즈몬의 방향을 입사 빛의 편광 상태의 변조를 통해 조절하는 내용에 대해 다루고 있다. 소자 구조와 입사 빛의 비대칭성 없이도 편광 상태의 조절을 통해서 표면 플라즈몬이 단방향으로만 여기될 수 있는 방법에 대해 기술하였으며, 그 원리를 설명하기 위해 입사 빛이 금속 슬릿 주변에서 만드는 유도 전류와 그로 인한 자기 모멘트의 모델링을 수행하였고, 이를 실험적으로 구현하였다.

3 절에서는 마찬가지로 금속 슬릿 주변에서 표면 플라즈몬의 방향 변조 현상에 대해 서술하였는데, 2 절에서와는 다르게, 두 개의 입사 빛의 위상 차이에 의한 표면 플라즈몬의 방향 변조 방법을 기술하였다. 이 방법은 두 평면파가 금속 표면에 입사되었을 때 생기는 간섭 무늬와 슬릿 간의

상대적인 위치에 따라서, 슬릿 내부에서 여기되는 표면 플라즈몬 모드가 변화하고, 그로 인해 투과면에서 여기되는 표면 플라즈몬의 대칭성이 변화하게 되는 원리를 이용한다. 이 방법의 실험적 구현을 위해서, 간섭계를 구성하여 두 개의 입사 빔 중 하나는 위상을 고정하고, 다른 하나는 전기적 신호로 미세하게 광 경로를 변조할 수 있도록 piezostage 가 이용되었다.

집적 광 회로 내에서 빛의 스펙트럼 분석 및 신호의 멀티플렉싱을 위해서는, 빛의 파장에 따라서 신호를 분리할 수 있는 플라즈모닉 소자가 필요하다. 3 장의 1 절에서는 2 장에서 다루었던 방법을 금속-유전체-금속 도파로층에 응용하여, 빛의 편광 상태와 파장 두 가지의 조건에 따라서 변조될 수 있는 플라즈모닉 색조 분리 방법에 대해서 기술하였다. 단층 금속층이 금속-유전체-금속 도파로 층으로 변경될 경우, 투과단이 금속층에 의해 차단되고, 이로 인해 입사 슬릿단에서 Fabri-Perot 공진 현상이 일어나게 되는 것을 이용하였다. 공진 조건에 따라서, 희망하는 두 개의 파장 대역은 서로 다른 플라즈몬 여기 위상을 가지게 되어, 파장에 따라 도파로로 여기되는 방향을 변화하는 것이 가능해지게 된다.

또한 3 장 2 절에서는 금속 슬릿이 아닌 금속 개구로부터 형성되는 표면 플라즈몬이 주변의 격자 구조에 따라서 회절 될 때 만들어지는 빔을 입사 편광에 따라서 조절할 수 있는 방법에 대해 기술하였다. 이 때 원형 금속 개구 주변의 격자 구조를 기존의 동심원형에서, 이중 나선형 구조로 변화시켜 편광 의존성을 증가시킴과 동시에 대칭성이 깨지지 않도록 하였으며, 나선 격자 구조의 회전 방향과 입사 편광 방향의 관계에 따라 빔의 각운동량이 변화하게 되고, 따라서 회절된 빔이 중심축 방향으로 뻗어 나가는 on 상태와, 중심축 기준으로 이중 나선형으로 분리되어 나가는 off 상태로 변화할 수 있음을 전산 모사를 통해 구현하였다.

감사의 글

학부를 마치고 대학원 신입생 세미나 준비를 하던 때가 엊그제 같은데, 어느덧 5년이라는 시간이 흐르고 박사 학위를 받게 되었습니다. 너무나도 부족한 것이 많은 제가 이렇게 무사히 학위를 마치고 졸업을 할 수 있게 된 데에, 도움을 주신 수 많은 분들에게 짧게나마 이 글로 감사의 마음을 전합니다.

먼저 저의 지도교수님이신 이병호 교수님께 감사 드립니다. 제가 학위기간 동안 조금이나마 연구자로써 성숙할 수 있었던 이유는 전부 교수님의 지도가 있었기 때문이라고 생각합니다. 항상 누구보다도 부지런하시고, 연구에 대한 열정을 가지고 지도해 주셨던 교수님이 계셨기에, 학위 과정 동안 있었던 여러 흔들림과 역경을 딛고 일어날 수 있었다고 생각합니다. 앞으로도 교수님의 기대에 부합할 수 있는 훌륭한 사람이 되겠다고 다시 한번 다짐하고, 앞으로 나아가겠습니다.

저의 부족한 학위 논문을 여러 모로 지도해주신, 심사 위원 분들께도 감사 드립니다. 제가 학부 때부터 여러 수업을 듣고 많은 것들을 느끼게 해 주신 이신두 교수님, 날카로운 지적으로 제 논문의 부족한 부분을 많이 채워주신 정윤찬 교수님, 제 학위 논문의 가장 세세한 부분까지 지적해 주시고 특히 저를 대신해서 사이언스지에 코멘트까지 남겨 주신 김경염 교수님, 제 보잘 것 없는 논문에 좋은 평가를 해 주시고 많은 개선점들을 말씀해주신 유경식 교수님, 네 분 모두 다시 한번 감사드립니다.

연구실 선배님이시자, 존경하는 교수님들로써 도움을 많이 받았던 분들께도 감사의 말씀 전해 드립니다. 먼저 짧은 시간이었지만 솔라셀과 관련된 연구를 하면서 좋은 말씀 많이 해 주신 김성철 교수님께 감사의 말씀 전합니다. 함께 오스트리아 학회에도 다녀왔고, 최근에도 저를 생각해 주시고 세미나에 넣어주신 정재훈 교수님께도 감사 드립니다. 많은 것들을 배울 수 있는 기회라고 생각하고 열심히 하겠습니다. 항상 너무나도 바쁘시지만 저를 비롯한 후배들을 챙기는 것을 잊지 않으시는 김휘 교수님, 존경스럽고 또 감사합니다. 김성철 교수님과 함께 연구할 때에도 계셨고, 이번 정재훈 교수님과 함께 하는 세미나에도 함께 계신 김정호 교수님, 항상

눈에 뜨이지 않는 곳에서 저를 비롯한 후배들에게 많은 도움을 주셔서 감사합니다.

제가 연구실 생활을 하면서 함께 했던 플라즈모닉스 팀 선배분들께도 감사 드립니다. 제가 연구실에 들어올 때부터, 학위를 받기 직전까지 인성적인 면에서나 연구에 있어서나 너무나도 큰 도움을 주신 일민이형, 사실 형이 계시지 않았다면 제가 했던 많은 일들이 빛을 발하지 못했을 것이라고 생각합니다. 같이 밤늦게까지 연구했던 많은 날들도 잊지 않고 간직하겠습니다. 비록 한달 여의 짧은 기간 밖에 연구실에서 뵙지는 못했지만, 복잡한 실험기구로 제가 신입생일 때 넘사벽의 면모를 보여주신 한준구 교수님, 제게 많은 관심을 가져주시고 광학 실험에 대해서 많은 것들을 가르쳐주신 용준이형께도 감사 드립니다. 제가 학부 졸업프로젝트 시절 때부터 제게 가장 가까운 선배셨고, 또 가까운 롤 모델이셨던 정현이형, 제 대학원 생활의 시작부터 끝까지 논문 작성법이며, 연구하는 방법이며 너무나도 많은 도움을 받았습니다. 매번 후배들에게도 정현이형 같은 좋은 선배가 되고자 노력하지만 쉽지 않은 것 같습니다. 포스트 닥으로 미국에 계시면서도 틈틈히 한국에 오셔서 도움 주시는 것들, 너무나도 감사합니다. 항상 맛있는 것들을 잔뜩 사주시던, FIB 공정과 ppt 그림그리기의 달인 숙영누나, 강한 멘탈과 쿨함의 상징이자 특히 방장으로 계실 때 온갖 굳은 일들 하셨던 모습이 인상 깊은 성우형, 피자를 접어서 드시던, 다행히 제가 강원도 출신이라 친절하게 대해주신 세윤이형, 연구실에서 항상 모범적인 모습만 보여주시고, 홀로 어려운 화학 공정 하시느라 고생이 많으신 한식이형, 실험을 하실 때 특히 쿨해지신다는, 제 개인적인 기준으로 저희 연구실에서 가장 잘생기신 준범이형, 앞으로 범죄 저지르면 상담하러 가야 할 R반의 에이스 민수형, 모두 감사드립니다.

또 이번에 저와 함께 졸업하시게 된, 제 여자친구 만들어 주시겠다고 다방면으로 고생해주신 태린 누나, 최근 강력한 후배들의 등장으로 일대일에서 고군분투 하시는 다운이형, 두 분 모두 고생하셨고 감사드립니다.

나와 초등학교, 고등학교, 대학교, 그리고 비슷한 시기에 연구실에 들어왔지만, 지금은 다른 길을 걷고 있는 민균, 사실 내가 여기까지 올 수 있었던 건 네가 있었기 때문이지 않았을까 하는 생각이 든다. 앞으로도 자주 볼 기회가 있었으면 좋겠다. 또 나와 동기로 연구실에 들어왔던 동호형과

인덕이, 함께 있었으면 여러 모로 더 즐거웠을 것 같다. 특히 인덕이는 박사 턱 때 내 술을 나눠 마셔줘야 하지 않을까나? 세 명 모두 동기로써 정말 고마웠다. 내 일년 후배이자, 올해부터 무거운 방장의 짐을 지게 된 OEQELAB의 간지남이자 캐쥬얼 플라즈모닉스의 창시자 의영이, 나와 모바일 세계를 함께했고, 올해부터 본격적으로 말년병장 자리에 앉게 된 지배자 규호, 숨겨진 재벌 2세이자 우유부단함의 상징 우영이형, 에어리 빔의 대가 치영이, 우리 팀의 미래를 짊어진 삼인방: 내 졸업프로젝트 후배였지만 여러 모로 도움이 많이 못 되어줘서 미안한 규근이, 2년 연속 신입생 세미나에서 진가를 발휘하고 있다는 현수, 하늘을 나는 우리 팀의 유망주 준수, 그 동안 너무 너희 셋을 신경 쓰지 못했던 것 같아 미안하다. 앞으로 연구실에 남아 있는 동안이라도 도움을 줄 수 있었으면 좋겠다. 김휘 교수님의 수제자이자, 미적 감각이 좋으신 재범이형, 자칭 얼룩말을 주장하지만 일대일 최강자이자 자가용 한대를 어깨에 메고 다닌다는 우영이형의 후계자 요한이, 지배자도 무서워한다는 벌키 선제, 모두 고맙고 앞으로도 뭐든 잘 하리라고 믿는다.

301동에 떨어져 있지만, 동고동락을 함께하는 3D 팀 분들에게도 감사의 말씀 전합니다. 먼저 3D 팀을 이끌어 주시는 민성욱 교수님, 나긋나긋한 목소리의 박재형 교수님, 예전 신입생 세미나에 참석하셔서 포스를 보여주셨던 최희진 교수님, 술을 좋아하신다던 주환이형, 3D 팀 여학우 에이스셨던 윤희 누나, 3D 팀 술 문화를 캐리하신 지수형, 제게 금장을 부탁하셨던 영민이형(죄송해요 저도 실력이 안되서요), 에너자이저 길배형, 훈남 재현이형, 이제는 3D팀 가장이시고 항상 고생이 많으신 기훈이형, 얘기는 많이 못해봤지만 3D팀에서 가장 일찍부터 일한다는 Chen Ni누나, 나와 훈련소 동기이자, 나대신 힘든 방장일 도맡아서 해 준 착한 순기, 이번에 성공적으로 부방장에 취임한 똑똑하고 센스좋은 지운이, 못난 날 데리고 금장을 달아주겟다 했던 에이스 창건이, 한국말을 정말 유창하게 하는 Li Gang, 3D 팀의 유망주이자 서울과고라 고생 많이 했던 종현이, 나랑 같이 놀 때만 트롤링한다는 종영이, 현수에게 고통받은 창원이, 인맥계의 최강자라는 영모, 우리 연구실 첫 서양계(?) 글로벌한 Matheus Miranda, 파릇파릇 신입생 진수, 모두에게 감사 드립니다.

어쩌다 보니 우리 연구실 분들 못지 않게 친해진 정윤찬 교수님 연구실 친구들에게도 감사의 말을 전합니다. 먼저 학부 때부터 R반의 큰삼촌으로 불리우던 현태, 내가 징징대던 것들 다 잘 들어줘서 고맙다. 결혼 다시 한번

축하하고, 앞으로도 자주 보고 잘 지냈으면 좋겠다. 연구실 초창기 때 우리 랩에 자주 놀러오던 승종이, 제가 광전자 공학 조교할 때 무슨 책 공부하면 좋냐고 물어보셨던 문파의 최강자 영철이형, 알고보니 부학생회장 친절한 진섭씨, LEAL롤팀 최강전력 병선이, 국대 나서스(?) 승수씨, 그 외에도 다른 연구실 분들, 제가 불쑥불쑥 찾아가는데도 항상 반겨 주셔서 감사합니다.

같은 건물 같은 방 쓰던 이름만 들으면 엄청 예쁠 것 같은 지윤이, 항상 심심하다고 먼저 연락하고 말 걸면 대답 안하는 쿨가이 최근재, 몇 안 남은 중학교 동창 중에서 가장 먼저 내게 연락해 주는 승주, 집에 내려갔을 때 부르면 항상 튀어나와주는 범기 다들 고맙습니다.

마지막으로 저의 사랑하는 가족에게도 고맙다는 말을 전하고 싶습니다. 매번 일 때문에 바쁘다는 핑계만 대고 집에도 자주 내려가지 않던 작은 아들 때문에 걱정 많이 하시는 부모님, 이 자리를 빌어 죄송하다는 말씀 드리고 싶고, 여기까지 계속 뒷바라지 해 주셔서 너무나도 감사합니다. 그리고 항상 귀차니즘에 빠져 사는 동생 챙겨 주느라 고생 많은 우리 형, 대놓고 말하기 그래서 그렇지 항상 고맙게 생각하고 있다우. 올해부터 혹시 같이 살게 되면 즐겁게 지내 봅시다. 그리고 가까운 곳에 계시면서 특히 학부 때 신세 많이 졌던 작은고모와 고모부께도 감사의 말씀 드립니다. 이제 용환이 전역하고 은호도 대학 들어가면 집안이 더욱 화기애애 해지겠네요.

언급 드리진 못했지만 함께했던 다른 분들께도 감사 드립니다.

2014년 2월 이승열 올림.